Dissertation
submitted to the
Combined Faculty of Mathematics, Engineering and Natural Sciences
of Heidelberg University, Germany
for the degree of
Doctor of Natural Science

Put forward by:

Paulina Maria Wysmolek

Born in:

Czestochowa

Date of oral examination:

19^{th} of July 2022

Light-sheet microscopy of 3D activity in neural organoids

Referees:
Prof. Dr. rer. nat. Joachim P. Spatz
Prof. Dr. rer. nat. Ulrich Schwarz

Zusammenfasung

Der Traum von der Schaffung eines zugänglichen neuronalen Netzwerks in einer Plastikschale ist mit der Entwicklung von aus Stammzellen gewonnenen Hirnorganoiden der Verwirklichung näher gerückt. Trotz dieses Erfolges fehlen einfache Technologien für die Netzwerkcharakterisierung in 3D, so dass wenig darüber bekannt ist, ob funktionelle Netzwerke gebildet werden können. In dieser Arbeit wurde eine Plattform zur Quantifizierung der elektrischen Aktivität in neuronalen 3D-Organoiden fertiggestellt und getestet. Der Aufbau umfasst ein einfaches, selbstgebautes Lichtscheiben-mikroskop, das eine räumliche Auflösung von einzelnen Neuronen (<2 μm) bei einer 3D-Aufnahmegeschwindigkeit (5 Hz) ermöglicht, die mit weit verbreiteten fluoreszierenden Ca^{2+}-Sensoren kompatibel ist. Zur Validierung des Systems wurden neurale Organoide aus embryonalen Stammzellen der Maus gezüchtet, die endogen einen Ca^{2+}-Sensor (RGECO1) exprimieren. Die spontane Netzwerkaktivität wurde innerhalb eines Sichtfeldes von 665 x 665 x 60 μm^3 aufgezeichnet. Zur Extraktion der Kalziumspuren einzelner Neuronen wurde ein Softwarepaket (CaImAn) verwendet. Die räumlichen und zeitlichen Komponenten wurden durch eine eingeschränkte nicht-negative Matrixfaktorisierung der 4D-Daten entkoppelt. Die Korrelationsanalyse der neuronalen Spuren identifizierte Cluster mit stark gekoppelten Neuronen (Spearman's Korrelationskoeffizient > 0.8). Der Aufbau ermöglicht Untersuchungen darüber, wie funktionelle neuronale Schaltkreise durch Selbstorganisationsprinzipien des multizellulären Systems geformt werden.

Summary

The dream of creating an accessible neuronal network in a plastic dish has moved closer to realization with the development of stem cell derived brain organoids. In spite of this success, simple technologies for the network characterization in 3D are lacking and thus little is known whether functional networks can be formed. In this thesis, a platform for quantifying electrical activity in 3D neural organoids has been finalized and tested. The setup includes a low-complexity home-built light-sheet microscope that grants single-neuron spatial resolution (<2 μm) at a 3D acquisition speed (5 Hz) compatible with widely used fluorescent Ca^{2+}-sensors. To validate the setup, neural organoids were grown from mouse embryonic stem cells which endogenously express a Ca^{2+}-sensor (RGECO1). The spontaneous network activity was recorded within a field of view of 665 x 665 x 60 μm^3. To extract calcium traces of individual neurons, a software package (CaImAn) was used. Spatial and temporal components were decouple using a constrained non-negativematrix factorization of the 4D data. Correlation analysis of the neuronal traces identified clusters with strongly coupled neurons (Spearman's correlation coefficient > 0.8). The setup will allow studies of how functional neuronal circuits are shaped via self-organization principles of the multicellular system.

Dedication

"You would not have called to me unless I had been calling to you," said the Lion.

— C.S. Lewis, *The Silver Chair*

"It's a dangerous business, Frodo, going out your door. You step onto the road, and if you don't keep your feet, there's no knowing where you might be swept off to"

— J.R.R. Tolkien, The Lord of the Rings

To my Parents, Sisters and furry brothers.

Moim Rodzicom, Siostrom i kudlatym braciom.

Acknowlegdments

"Talking nonsense is the sole privilege mankind possesses over the other organisms. It's by talking nonsense that one gets to the truth! I talk nonsense, therefore I'm human"

— Fyodor Dostoevsky

I would like to thank my Family. *My Parents, Sisters, Grandma, Cousins, Aunts and Uncles. Without their love and constant support I wouldn't have written this thesis. They believed in me when I was far from believing in myself.*

My friends *especially Alejandra Ross Beraldi, Jincy Joy, Max Terban, Jacqueline De Lora, Silvia Antona, Saliha Erici and Jenny Diemer for always having my back - even at 2 am in the lab (it's akshay true).*

My friends and proof-readers *Jacqueline De Lora, Philipp Fleig, Katja Salbaum, Filippo Kiessler, Achim Brinkop, Elijah Shelton, Yannik Dreher. They went through the draft of this thesis to help me get it into the right shape.*

My supervisors *Friedhelm Serwane and Joachim Spatz for giving me the opportunity to work on this exciting project. They supported and encouraged me, spent their time and resources which I am very grateful for.*

Finally, thank you God. *For all of the above-mentioned and not-mentioned blessings.*

Contents

Chapter 1

General Introduction

"Begin at the beginning" the King said gravely, "and go on till you come to the end: then stop."

— Lewis Carroll,
Alice in Wonderland

Neurons are electrically excitable cells with multiple inputs (dendrites) and a single output (axon). They build fascinating, intricate structures: neuronal networks. A single neuron integrates the electrical signals it receives from its neighbours and then fires when a threshold is reached, passing the electrical signal to other neurons. Prominent examples of organized neuronal networks are the brain and the retina. They both are part of the central nervous system. As an indicator of their complexity, the number of neurons (computational units) they contain can be considered. And so, the brain is estimated to contain around 86 billions of neurons [1]. This is of the same order of magnitude as the number of stars in the Milky Way[1]. As for the retina, it contains around 100 millions of light-sensitive neurons (4.6 million cones and 92 million rods) [2]. Meanwhile, a modern processor includes as many as 59.4 billions of transistors[2] - building blocks of a computer circuitry. Biological neural networks have the important property that the connections between neurons are adaptive and can change over time. This is not the case for digital logic implemented in a computer chip architecture.

Image encoding by the retina and cognition in the brain are produced through complex neuronal firing patterns. However, many aspected of these patterns are still poorly understood. For this reason, electrophysiological readout of biological network activity at a single neuron resolution in physiological conditions is needed. Yet, the experimental access for recording technologies to be applied to human brain or retinal tissue is limited.

In the past years, important advances in the field of neuroscience could be made with the introduction of cerebral and retinal organoids - multicellular three-dimensional systems derived from embryonic stem cells and induced pluripotent stem cells [3, 4, 5, 6]. These artificially generated structures mimic key aspects of neuronal be-

[1] NASA
[2] Mk2 intelligence processing unit

haviour and tissue architecture of organs. Nevertheless, it is still an open question to evaluate the extent to which they replicate network function as seen *in vivo* [4, 7].

> In this thesis I describe my work to build a platform to study the spontaneous behaviour of a 3D neuronal network in a neural organoid generated for that purpose. To achieve this task, the following experimental challenges have to be overcome. Neurons communicate with their neighbours at a milliseconds timescale via electrical signals, i.e. spikes or action potentials. Thus, the functionality of a neuronal tissue needs to be assessed at this timescale in 3D by studying its electrical activity at a single neuron resolution.

In the past, electrophysiological signals of single neurons within neurospheres [8, 9] cerebral organoids [10, 11, 12] and retinal organoids [13, 14, 15] have been recorded using patch clamp electrophysiology. The high temporal (sub-millisecond) resolution of this technique enables sampling of individual action potentials and thus the determination of inhibitory and excitatory neuronal response upon external stimulation. However, only few individual neurons can be inspected at once which prevents the mapping of network connectivity. Advances in Complementary Metal-Oxide-Semiconductor (CMOS)-based multielectrode array technology (MEA) have allowed to capture extracellular potentials created by sliced neuronal populations to analyse 2D connectivity and neural circuits in neurospheres [16], cortical cultures [17, 18] and organoids [19], brain [6, 7, 20, 21] and retinal organoids [22].

Recently, 3D characterization of network behaviour in brain organoids was performed by combining MEA with CMOS based shank probes [7]. While electrode approaches offer unprecedented time resolution, their spatial resolution in 3D is mainly limited by the ability to place electrodes at different tissue depths. As a result, single cell resolution in the third dimension (z) is difficult to obtain. In addition, identification of neuron types comprising the network and as such the assessment of tissue morphology is challenging due to limited optical access to the sample. This is a particular drawback for characterizing organoids consisting of different neuron types, for example cerebral and retina organoids [4, 23, 24].

Monitoring 3D network activity with simultaneous access to cell morphology is possible via microscopy using fluorescence based electrical readout, for example via Calcium imaging [25]. The functionality of both cerebral and retinal organoids has been characterized with confocal one- and two-photon microscopy [3, 26, 27, 28]. However, limited scanning speed of the confocal microscope experiments were restricted to 2D. To overcome this challenge, custom microscopes have been developed, including light-sheet and light-field microscopes (Table 2.2).

Using sophisticated custom-built optical setups, functional 4D (three space and one time direction) activity mapping in *Caenorhabditis elegans*, zebrafish, and primary neuron cultures have been performed at scanning rates between 0.8 to 50 Hz [29, 30, 31, 32, 33, 34, 35, 36]. Moreover, artificial intelligence–enhanced microscopy has improved the performance of a light-field microscope in functional imaging of neuronal activity of the zebrafish brain [37].

While these setups are in principle suited to perform volumetric imaging of neuronal networks, they require advanced optical expertise in their assembly and alignment [37, 38, 39, 40, 41, 42, 43, 44, 45, 46, 47].

In this thesis, a platform for 3D mapping of neuronal activity at single neuron level is developed. It is a custom-built light-sheet microscope tailored to state-of-the-art computational neuroscience tools [48].

The setup allows for calcium imaging of a broad range of samples in physiological conditions with subcellular resolution at 5 Hz, which is the same temporal regime as other custom-built microscopes. It is tailored to widely used Ca^{2+}-imaging sensors, but displays orders of magnitude lower complexity and costs compared to previous implementations.

This thesis is organized as follows: Chapter 2 presents main concepts from neurobiology, biophysics, optics and image analysis which are necessary to paint the problem landscape of studying neuronal systems. Chapter 3 discusses in steps the approach implemented to achieve that goal. First, the setup's design and characterization in terms of spatio-temporal resolution is considered. Next, the generation of a sample needed to validate the setup is presented. Further, an analysis pipeline employed for information extraction is shown and used to inspect the behaviour of a representative sample. Chapter 4 represents a summary of the key accomplishments achieved in this work. Finally, Chapter 5 focuses on the outook and future prospects such as a possible bridge between the experimental results obtained in the frame of this thesis and a theoretical model (a Hopfield network).

Chapter 2

Background

A world of dew,
And within every dewdrop
A world of struggle.

— Kobayashi Issa, *A World of Dew*

This chapter introduces concepts from biology, biophysics, optics and image analysis that set this thesis in a proper context. First, the architecture and basic functioning a neuronal cell will be discussed. Next, *in vitro* models used to study neuronal systems will be presented along with methods used to characterize their structure and function. In particular, light-sheet microscopy and calcium imaging will be described. Finally, state-of-the-art algorithm for calcium imaging data, CaImAn [48] will be considered along with simple filters for image processing. The work in this thesis, which is to establish a low-complexity experimental method for characterising 3D neuronal systems, builds upon the concepts presented in this chapter.

2.1 Neuron: unit of the nervous system

The term "neuron" was coined by Heinrich Wilhelm Gottfried von Waldeyer-Hartz, German anatomist in his lectures to describe the nerve cell as the basic and discrete structural unit of the nervous system [49].

2.1.1 Neuron anatomy

Neurons are electrically excitable eukaryotic cells in which the nucleus is contained in a specialized compartment. The majority of neurons develop two types of unidirectional projections from their cell body:
• numerous, thin dendrites - allowing the cell to connect to its environment and to receive signals from its neighbours
• a single long thick extension - axon- which the cell uses to broadcast singles to its environment (Figure 2.1 A.)
The inside and outside of the neuron is separated by a cell membrane - a thin (5 - 10 nm [54]) phospholipid bilayer. An electrochemical gradient is actively maintained across the membrane which converts it into a fascinating capacitor (Figure 2.1 B.).

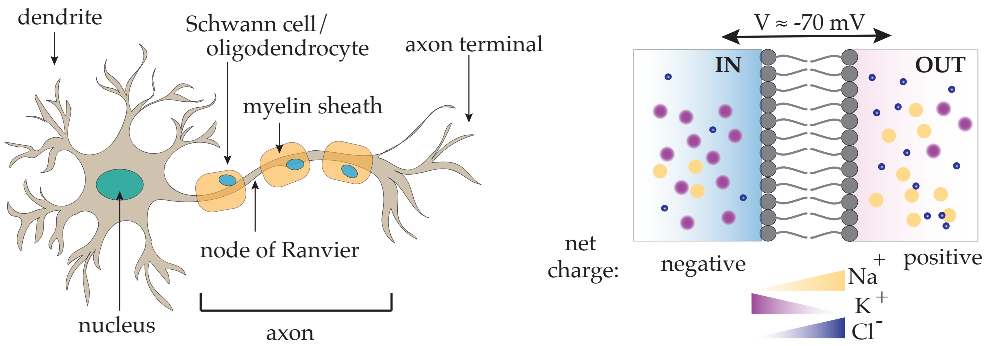

Figure 2.1: **Neuron anatomy A.** Components of a neuron cell. B. Electrochemical gradient maintained across a semi-permeable cell membrane in a resting state. Concentration of Na^+ and Cl^- ions are higher inside the cell (IN) and lower outside (OUT). The opposite is true for K^+ ions. For each ion species, the knowledge of its charge and concentration gradient across the membrane allows to calculate a so called reverse potential, for which there is no net flux of this ion species across the membrane. This can be done using the Nernst equation [50]. The reverse potential of the membrane that takes into account all ions that can permeate the membrane can be calculated using the Goldman–Hodgkin–Katz voltage equation [51, 52] Redesigned from [53].

Approximate ionic concentrations in the extra- and intracellular fluids are presented in Tab 2.1.

Table 2.1: **Extra- and intracellular ion contractions** at resting state [25, 55]

Ion	$C_{extracellular}$ $[mM]$	$C_{intracellular}$ $[mM]$
Na^+	140	12
K^+	4	135
Cl^-	116	4
Ca^{2+}	1	$\approx 7x10^{-4}$

Axons are enwrapped in periodically distributed segments of a fatty, insulating substance - myelin - which is produced mainly by:

- Schwann cells (in peripheral nervous system, PNS)
- Oligodendorcytes (in central nervous system, CNS).

Myelin acts as a electrical insulator and allows for fast signal conduction along myelinated neurons. Conduction velocities for myelinated axons scale with $\propto \ a$ where a is the radius and for unmeylinated axons $\propto \sqrt{a}$[56].

Regions non-covered by myelin ($1 - 2\mu m$ long), are called Ranvier nodes. They are densely packed with voltage-gated ion channels embedded in the cell membrane.

2.1.1.1 Voltage gated ion channels

Voltage-gated ion channels are transmembrane proteins that are selectively permeable to a particular type of ions and allow for their movement across the cellular membrane (Figure 2.2).

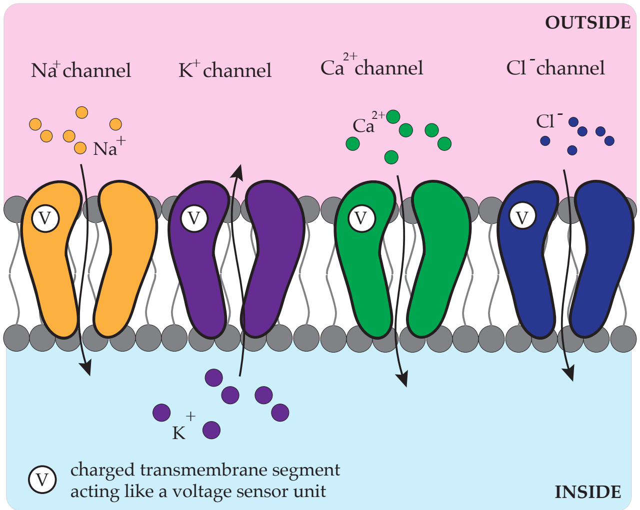

Figure 2.2: **Voltage-gated ion channels** are selectively permeable to sodium, potassium, calcium or chloride ions. Their state, open/close, is controlled by the membrane potential. Channel properties such as ion selectivity and conductance are dictated by the amino-acid sequence and as a result structure of the pore.

Their structural conformation and thus ion conductance is modulated by the membrane potential value. For that purpose, channels are equipped with voltage-sensing domains (Figure 2.2).

2.2 Neuronal signals

Synaptic communication between neurons occurs by means of action potentials (AP) - transient changes of the polarization state of the cell membrane. They are primarily generated by changes in membrane permeability to Na^+ and K^+ ions [57].The propagation of these signals varies depending on whether the neuron axon is covered in myelin - or not.

2.2.1 Unmyelinated neurons

The CNS is mainly made out of myelinated nerve fibres. However, PNS contains many unmyelinated fibres. It turns out they retain a degree of plasticity and ability to sprout collaterally which allows them to respond first to injury or disease in their neighborhoods [58].

2.2.2 Hodgin and Huxley and the cell membrane

A quantitative description of the electro-chemical behaviour of the cell membrane was put forward by A.Huxley and A.Hodgkin in 1952 (H&H) [59] based on their voltage clamp experiments performed on a squid giant axon.

2.2.2.1 Squid giant axon

The anatomy of the squid giant axon was studied and described in 1909 by Leonard Worcester Williams (L W Williams). One of the most remarkable features of these animals were their very large (up to $\approx$ 1.5 mm in diamter) axons which partially control the jet propulsion system that the squid employs to perform fast movements throught the water. John Zachary Young demonstrated the function of the giant axon in the laboratory which turned out to be pivotal for experimental electrophysiology [60]. Indeed, the surface of squid giant axon was large enough to allow for the insertion of an electrode of $\approx$ 500 μm in diameter and let Huxley and Hodgkin conduct their current flow measurements.

2.2.2.2 Hodgin and Huxley's experimental setup

To characterize electrophysiological properties of the cell membrane and its ionic permeability, Hodgin and Huxley employed voltage clamp method, first proposed by George Marmont in 1949 [61](Figure B.) In their set up, two electrodes are introduced into squid giant axon in a feedback circuit. Electrode 1 records voltage across the membrane and compares it with the voltage set by the experimenter. If the two voltages differ electrode 2 is used to inject current into the axon to compensate for the difference and "freeze" the membrane at a desired voltage with the help of a high-frequency amplifier. This injected current is necessarily equal to current flowing through the ionic channels of the membrane. This granted H&H the ability to directly record contributions to the ionic currents across the membrane in a step-wise manner while minimizing the capacitive currents. In addition, the approach allowed the ionic currents to be separated.

2.2.2.3 Hodgin and Huxley's equation

In the H&H model, current flow across the membrane can be described in terms of ions flowing via sodium and potassium voltage-gated ion channels as well as other channels not modeled expilicitly. These are represented by leakage channels (for example Cl^-). The equivalent circuit representing the system is depicted on Figure 2.3.

• equivalent circuit

Each type of channel is represented by a resistor: for sodium R_{Na}, potassium R_K and other channels R_l (Figure A.). Arrows on the resistors indicates that the resistances are adjustable and depend on the state of the channel (open/closed). The ion concentration differences across the membrane give rise to Nernst potential, which can be calculated for particular ions and are represented in the circuit by three batteries: E_{Na}, E_K, E_l. Their orientation reflects the overall concentration on the inside and outside of the membrane of the particular type of ion ans as a consequence, the direction of the ion flow upon channel opening (convention: inward current positive). In practice, it is convenient to express specific potentials E_{Na}, E_K, E_l as displacements from the resting potential E_r:

$$V_{Na} = E_{Na} - E_r \tag{2.1}$$

$$V_K = E_K - E_r \tag{2.2}$$

$$V_l = E_l - E_r \tag{2.3}$$

The total membrane current is decomposed into capacitive and ionic terms:

$$I = C_M \frac{dV}{dt} + I_i \tag{2.4}$$

where I is the total membrane current density, C_M is the membrane's capacity per unit area (assumed to be a constant), V is the displacement of the membrane potential from it's resting value, t is time and I_i is the ionic current density.

• ionic contributions to observed current
Ionic current can be expressed in terms of the sodium, potassium and leakage conductances and three time- and voltage-dependent variables n,m and h

$$I = C_M \frac{dV}{dt} + \bar{g}_K n^4 (V - V_K) + \bar{g}_{Na} m^3 h (V - V_{Na} + \bar{g}_l (V - Vl) \tag{2.5}$$

where $\bar{g}_{Na}$, $\bar{g}_K$ and $\bar{g}_K$ are constants with the dimensions of conductance ($mmho/cm^2$ equivalent to mS/cm^2). As for the gating variables n, m, h they are unit-less, can adopt values between 0-1 (Figure 2.3) and are expressed in terms of voltage dependent rates α and β

$$\frac{dn}{dt} = \alpha_n (1 - n) - \beta_n n \tag{2.6}$$

$$\frac{dm}{dt} = \alpha_m (1 - m) - \beta_m m \tag{2.7}$$

$$\frac{dh}{dt} = \alpha_h (1 - h) - \beta_h h \tag{2.8}$$

Gating variables are meant to represent the portion of channel-activating or -inactivating molecules on the inside (n, m, h) or outside ($1 - n$, $1 - m$, $1 - h$) of the membrane. Rates at which these molecules are transferred across the membrane are dictated by α and β. n, m describe the activation of the potassium and sodium channel respectively and h the blocking of sodium channel.

2.2.2.4 Action potential in terms of HH model

The elegant model proposed by H&H allowed them to describe a propagating action potential in terms of dynamic changes in Na^+ and K^+ conductances and the gating variable (Figure 2.4).
Once the membrane potential reaches the threshold value of about $-$ 55mV, membrane permeability to Na^+ ions increases (gating variable m increases) which further reinforces depolarization.
Depolarization causes a slower rise increase of potassium conductance (gating variable n increases), which results in efflux of K^+ ions.
In a next step, Na^+ voltage gated channels are inactivated (increase in h gating variable) and further efflux of K^+ ions re-polarizes and hyperpolarizes the membrane. Action potential can not travel back because K^+ channels remain activative while Na^+ channels are inactivated (refractory period). It takes several miliseconds for the channels to de-inactivate and close when the membrane's voltage reaches back the resting state (Figure 2.4 D.).

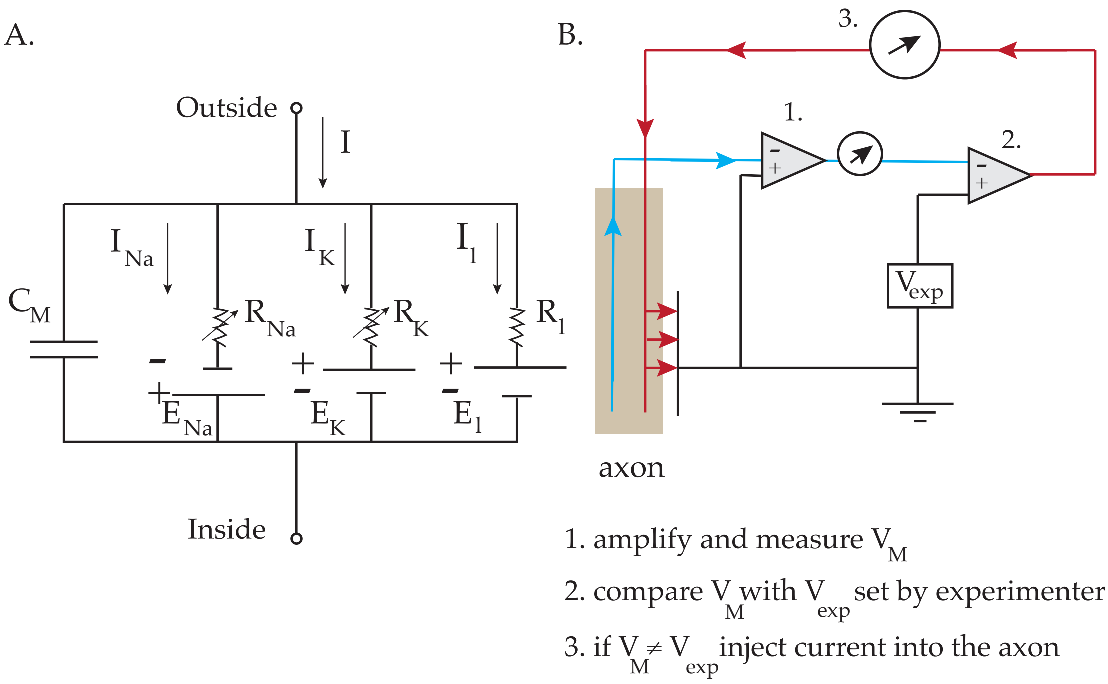

Figure 2.3: **H&H expriment and findings A.** Equivalent circuit for the membrane. Each type of channels is represented by a resistor: R_{Na} (sodium), R_K (potassium) and R_l (other channels), I is the total membrane current density which is decomposed into individual ionic currents (sodium I_{Na}, potassium I_K, "leakage current' I_l), C_M is the membrane's capacity per unit area, E_{Na} and E_K are the equilibrium potentials for the sodium and potassium ions and E_l is the potential at which the "leakage current' is zero. B. experimental setup used by H&H to study squid giant axon in laboratory. Voltage across the membrane is measured, amplified (1.) and compared it with the voltage set by the experimenter (2.). If the two voltages differ current is injected into the axon (3.) to compensate for the difference and "freeze" the membrane at a desired voltage. Adapted from [59] [62]

2.2.3 Signal propagation in myelinated neurons

High action potential velocities developed in myelinated axons cannot be described in terms of the cable theory of ion diffusion. This realisation pushed theoreticians to link the phenomenon to another physical mechanism. It will be briefly touched upon in the next section.

2.2.3.1 Wave-type saltatory conduction

Very recently, a new conduction model emerged which constitutes an ion analogue to electron plasmon-polaritons in metallic linear periodic system [63]. Conduction is here described as a collective, synchronized ion oscillation in periodically organized myelinated segments that propagate as a wave along the axon.
• Frequency of the plasmon-polariton must be tuned to the dynamics of opening of Na^+ channels and the μs time of gate triggering. It is the H&H cycle that dictates the subset of wave frequencies (given by a subset of k wave vectors) that can be maintained along the axon. Because of the geometry of the myelinated segments, it is the longitudinal modes of plasmon-polariton wave that can synchronise with H&H. That way, they are supplemented in energy and can polarize/depolarize consecutive nodes of Ranvier.

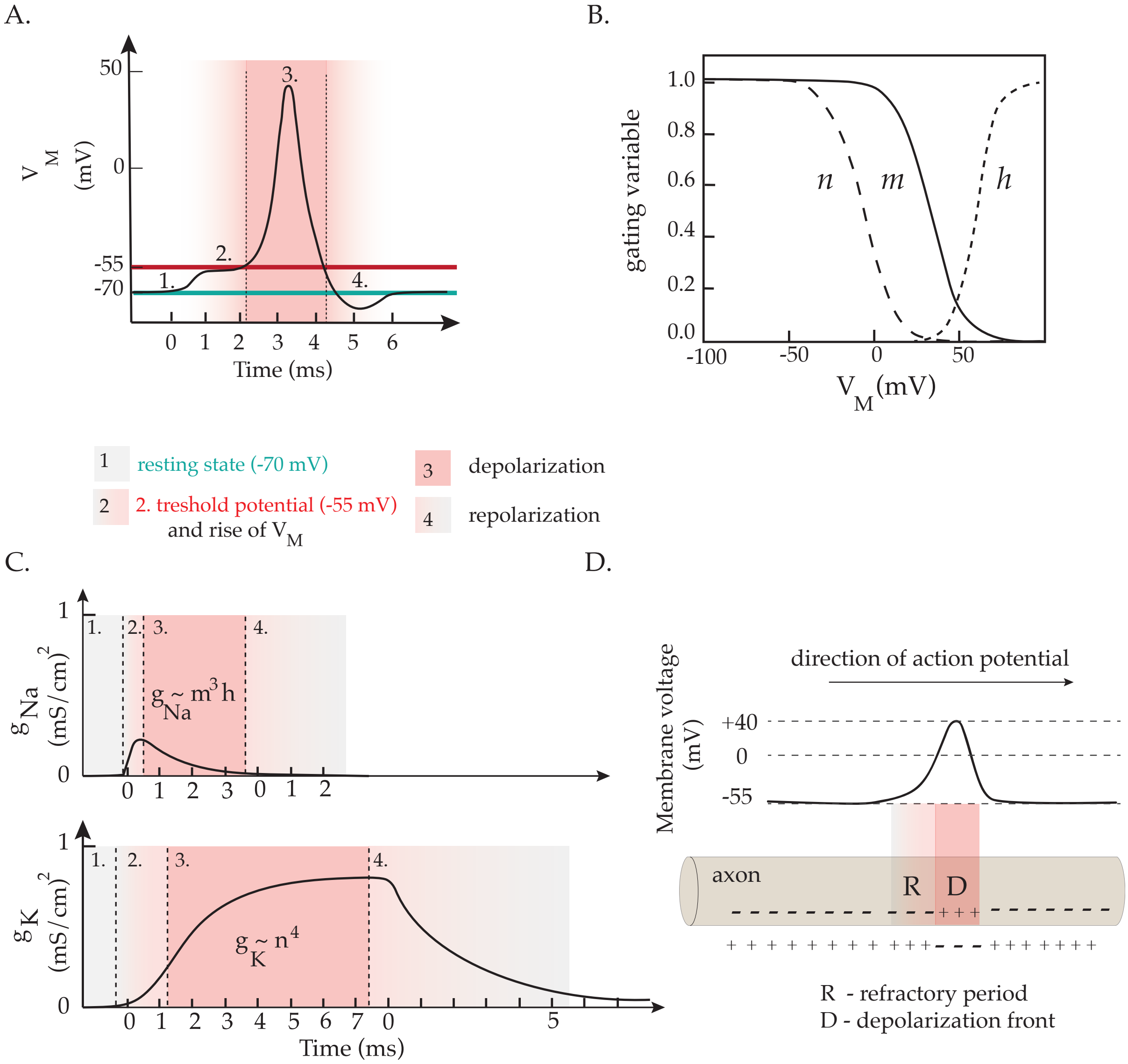

Figure 2.4: **Action potential in terms of gating variables A.** Action potential graph describes propagating changes of membrane potential (V_M) values at as a function of time. B. n, m, h gating variables are membrane potential depended and their behaviour accounts for the C. changes in sodium and potassium conductances during an action potential - m and h for sodium and n for potassium. Noticeably, sodium conductance rises faster compared to the potassium. D. Two regions within the axon can be distinguished during an action potential propagation - the part at which the front of the depolarization wave (action potential) is currently present (D) and the part where the front just past (R). Adapted from [59], [62].

• Another key factor for maintaining the dipole oscillations is the adjustment of myelin thickness ζ layer across which a pair of coupled oscillators is created (Figure 2.5). A mode with a beating frequency which matches gating-time of Na^+ channels allows for synchronisation with the H&H. Other modes, out of synchronization and thus not continuously supplemented in energy from action potentials are damped. For more details the reader is encouraged to consult chapter 12 of the book "Quantum Nano-Plasmonics" [64].

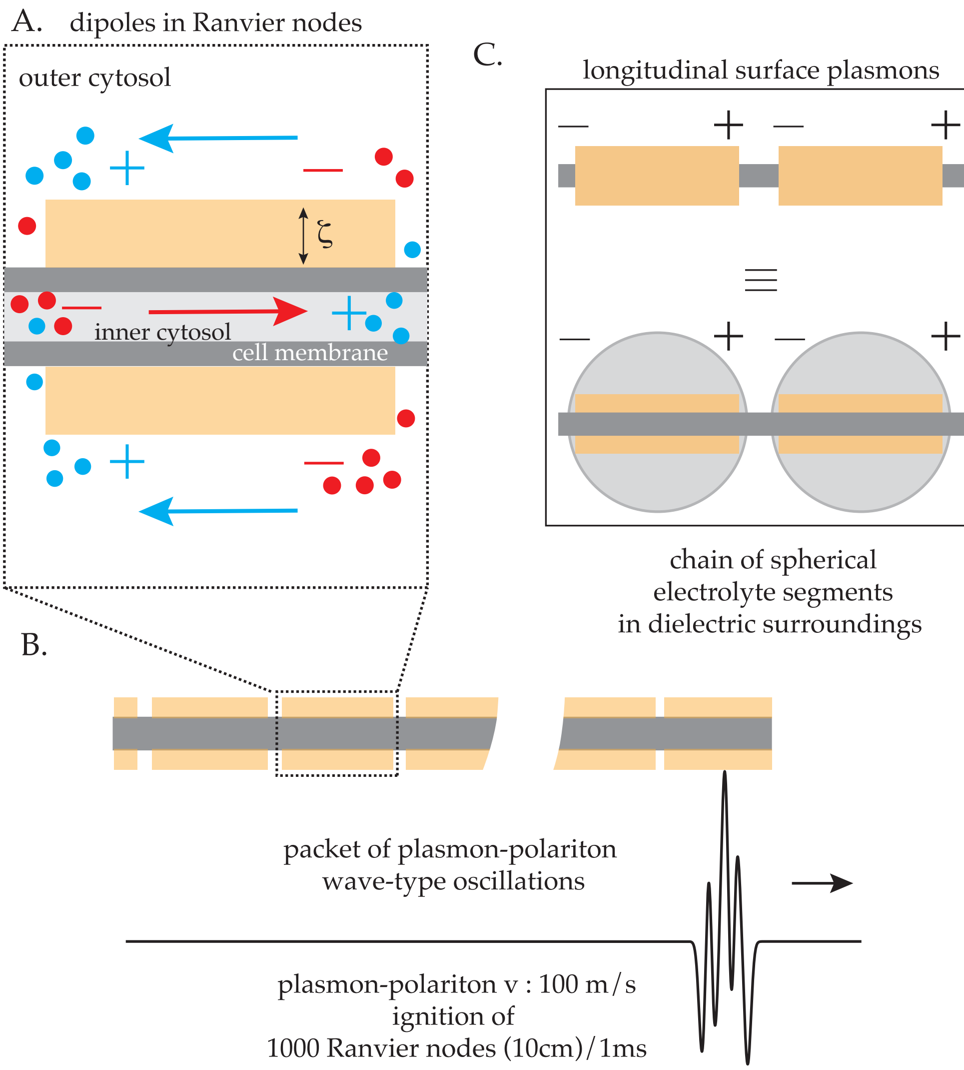

Figure 2.5: **Saltatory conduction** Collective fluctuations of charge distribution are called plasmons. A. Action potentials are synchronized oscillations of local ion density that take the form of a plasmon-polariton wave and propagate along the periodically myelinated axon B. Group velocities of the plasmon-polariton modes are of the order of 100 m/s C. The myelinated axon can be treated as 1D chain of electrolyte spheres between which dipole-type coupling of the dipole plasmon-polariton nature can occur. Adapted from [63]

2.2.3.2 Representation of a neuronal network - summary

To set up the stage for further discussion, a cartoon representation of a neuronal system and the properties of its building block - the neuron- are depicted on Figure 2.6. Electrically excitable networks of mammalian neurons as found in the CNS, are densely packed, light scattering and optically opaque. Within the neuron, signals travel from dendrites (IN), through the cell body, to the axon (OUT) at speeds that depend on the type of neurons (myelinated or non-myelinated).

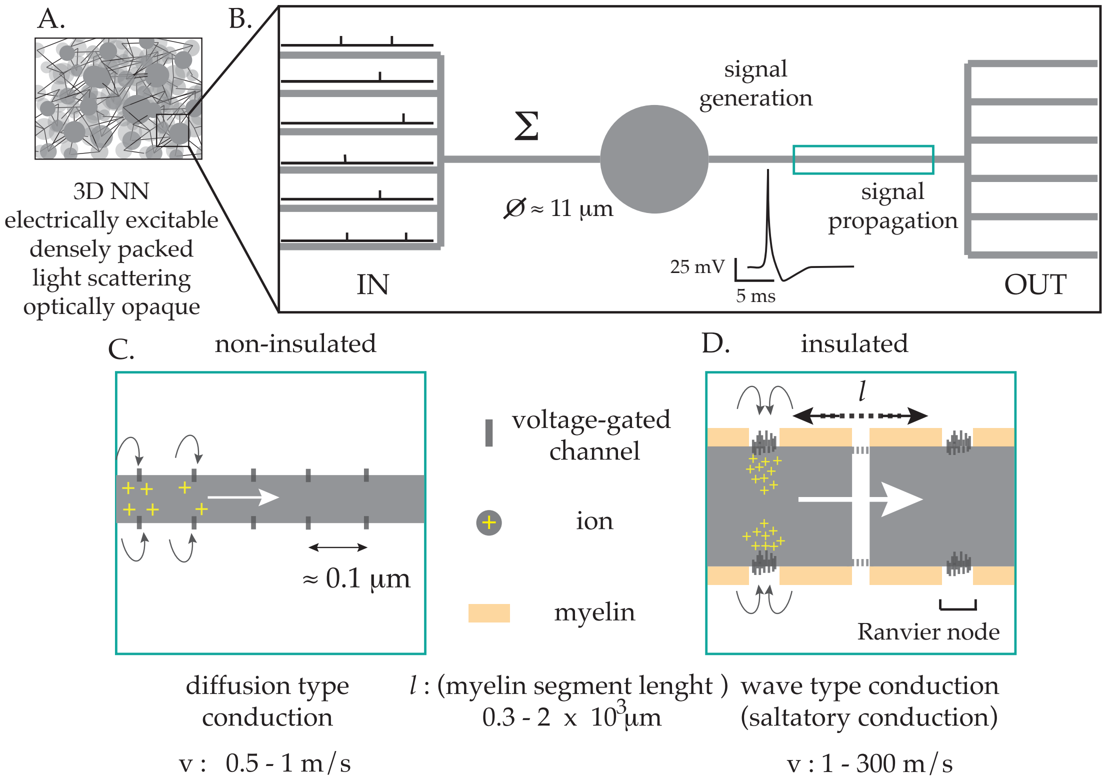

Figure 2.6: **Simplified look at a neuron system A.** 3D neuronal network (3DNN) can be seen as an electrically excitable, densely packed, light scattering and optically opaque material continuously dissipating energy (it is alive!). B. The building block of the network is a neuron with inputs (dendrites), a computational unit (cell body) that integrates incoming signals and an output (axon) which transmits response signals (action potentials) to other fellow neurons. C. Depending on the type of neuron, conduction can be slow, diffusion driven in non-myelinated (non-insulated) axons and D. fast, wave-like in myelinated (insulated) ones. Inspired by [65]

2.3 What do we need to study neuronal systems?

The minimal kit to study neuronal systems has to include a study material as well as experimental and computational tools to inspect it:

- Sample: Easily accessible neuronal sample
- Readout: 3D activity signal readout
- Resolution: Cellular[a] Spatial and Millisecond Temporal Resolution
- Analysis: Pipeline to extract information from a densely packed system[b]

[a]By cellular resolution around 5 μm is assumed (considering the soma of an averaged neuron is about 11 μm [66]).

[b]densely packed tissue can be understood as 'crowded". That means for instance that if the tissue was to be imaged, strong overlap between distinct cells that should be treated separately could occur.

In the next sections, each point will be addressed.

2.4 Sample: neural organoids

One factor limiting neuroscience research is difficult access to intact living brain tissue. Excitingly, this issue has partially been solved with the advent of organoids, 3D organ-like structures. These artificial models recapitulate some aspects of the functionality and tissue architecture of their natural counterparts. They have first been generated using embryonic stem (ES) cells [1] and later induced pluripotent stem cell (iPS) [2].

So far, organoids resembling specific brain regions have been generated and employed inter alia for studying neuro- and pathology development, for instance to model complex neurodegenerative diseases like Alzheimer's disease (AD) [70, 71].

In 2011 Eiraku et al. showed a 3D optic cup formation from pluripotent stem cells [72]. This opened the doors to the development of new retinal models for studying retinagenesis and pathologies. This is how, in 2020 Cowan et al. reported the generation of multilayered human retinal organoids which had light-sensitive cells with functional synapses [26].

In this thesis, a protocol for creation of retinal organoids from mouse embryonic stem cells was followed [73] to obtain an order 3D neuronal network (Figure 2.7).

[1]ES have the ability to self-renew and to differentiate to all of the cell types in the body. They are obtained from the cells of the inner cell mass of preimplantation embryos[67, 68]

[2]iPS are generated from differentiated cells in the process of cell reprogramming [69]

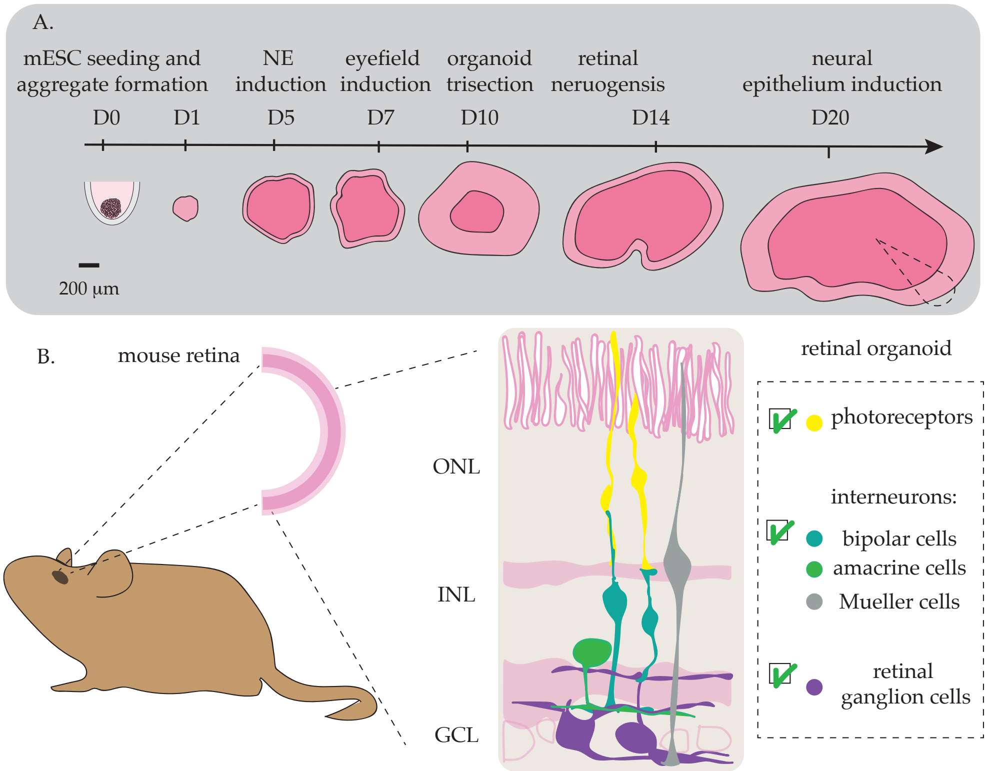

Figure 2.7: **Mouse retinal organoids as model systems A.** Schematic overview and timeline of the culture protocol that includes seeding of a set initial number of mESC in U-bottom well dish to allow for their aggregation and embryoid body formation. Within the first 7 days, neural epithelium (NE) forms after what the induction of eyefield starts. At D10, organoids are trisectioned (cut into 3 parts) and retinal neurogensis proceeds further. B. Cellular composition of mouse retina has been compared to a D20 mouse retinal organoid. The organoid created a layered structured within which the presence multiple of retina-specific cells has been confirmed: photoreceptors within the outer nuclear layer (ONL), bipolar cells, amacrine cells and Mueller cells within inner nuclear layer (INL) and the retinal ganglion cells in ganglion cell layer (GCL). Iinspired by [73] and vision-research. To create the figure data from [73, 74] were used.

2.4.1 Characterization of 3D samples

One of the ways to characterise the cellular architecture of naturally and/or artificially obtained biological samples is to employ the knowledge of molecular markers which uniquely identify a cell.

2.4.1.1 Immunohistochemistry and cryosectioning

Detection of molecules of interest in tissue samples can be done using immnocytochemistry (IF), which exploits selective antigen-antibody (AG-AB) binding. AG-AB bonds belong to the category of weak physical bonds mainly involving: (I) hydrogen bonds (II) Coulombic bonds (III) hydrophobic (IV) Lifshitz–van der Waals bonds [75] One strategy used in IF is the indirect labelling (Figure 2.8) that includes two steps:

1) primary AB binds to the component of interest (antigen)
2) secondary AB binds to the primary AB and since it is conjugated with a fluorophore, it provides a signal that can be detected for example in a fluorescent microscopy setup.

In addition, as multiple II AB molecules can bind to a single I AB, a signal amplification occurs.
The labelling mechanism relies on slow diffusive transport of antibodies (in this case both I AB and II AB). As a result, the penetration depth of AB into the 3D tissues is limited and the achievement of homogenous labelling is challenging. Strategies are being developed to expedite antibody transport with the use of external forces such as an electric field [76].

The problem can however be mitigated by simply slicing the sample into sections which grants access to layers located deep in the tissue. This can be done using cryosection procedure that involves rapid freezing (-50°) and thin cutting of the sample. The machine allowing to perform such procedure is called a cryostat. It is equipped with a sharp blade and a precise stage that allows for sample manipulation at low temperatures (-10 to -20°). Thin sections of the sample that can then be transfer on to glass slides and labelled.

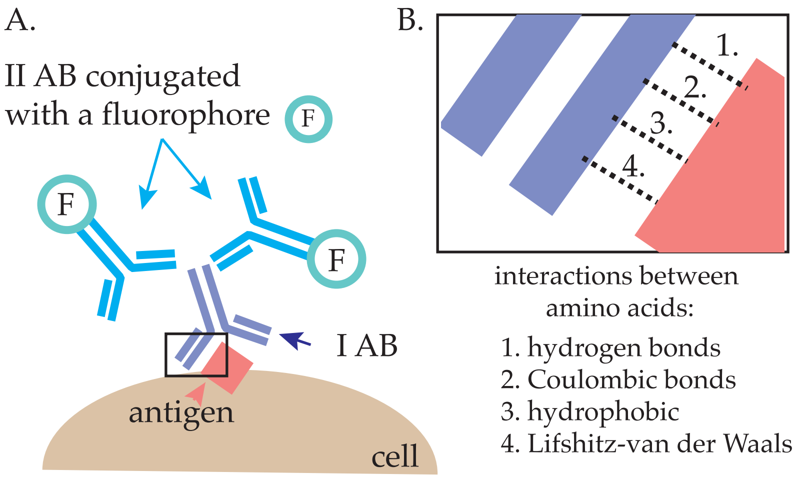

Figure 2.8: **Principle behind immunofluorescence staining A.** Primary antibody (I AB) binds specifically (though not covalently) to an antigen molecule present on the cell surface. Next, a secondary antibody (II AB) conjugated with a fluorophore binds to the primary antibody and provides a readout signal. It is possible to permeate the cell membrane and detect antigens present inside the cell. B. The nature of the interactions between aminoacids forming both the antigen and the antibody are non-covalent (thus reversible) and can be: hydrogen bonds (operative at very short distances ($1.5 - 5\,\AA$), Coulombic bonds (distances of the order of $100\,\AA$)), hydrophobic, Lifshitz van der Waals.

2.5 Readout: functional characterization of neuronal systems

Functional characterization of *in vitro* generated neuronal systems such as neural organoids is necessary for these systems to be used as model systems or test beds for drug development. In this section, methods used for electrophysiological analysis will be presented, ranging from current recording of a single ion-channel (patch clamp) and activity dynamics of cell populations (2D and 3D MEA, soft mesh electronics calcium imaging).

2.5.1 Patch Clamp

The behaviour of individual ion channels of interest can be investigated with the use of a fine-tipped glass micropipette that when carefully position around cell membrane can tightly seal it with a resistance of >1 $G\Omega$ (Figure 2.10 A.). The trapped channel can be exposed to various stimuli from within the pipette [83]. This configuration is called cell-attached and is the most 'physiological' as it leaves the cell intact. Other patch clamp recording methods exist such as:
• whole-cell: the pipette gains access to the cytoplasm by rupturing the cell membrane
• inside-out cytosolic surface of the membrane is exposed to air
• outside-out: the cytosolic side of the membrane faces the pipette solution

Whole-cell patch clamp has been used to characterized neuronal activity of 27 neurons in human cortical spheroids [84]. However, whole-organoid network dynamics can not be investigated with the excellent temporal resolution that the technique offers.

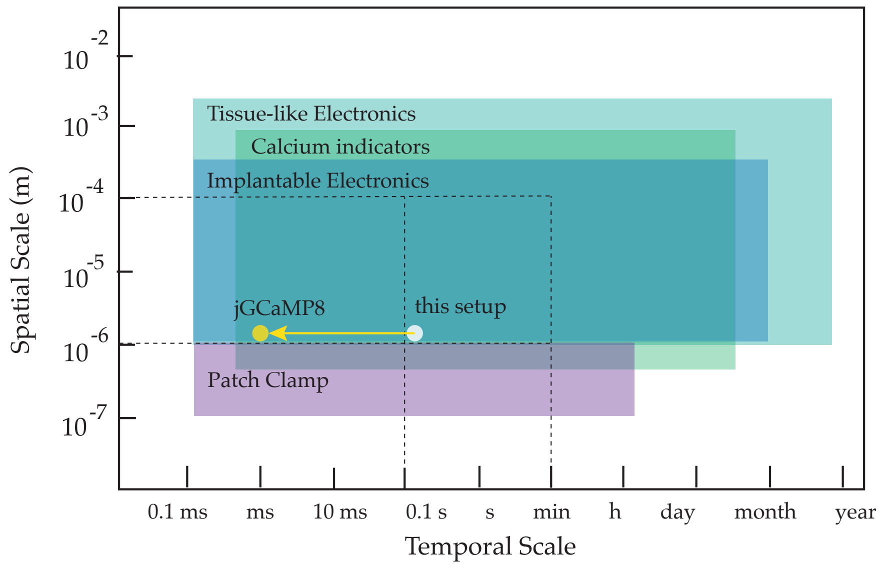

Figure 2.9: **Methods for studying electrophysiology of neuronal systems** offer various spatial and temporal resolutions. Tissue-like and implantable electronics along with microscopy techniques using calcium indicators allow to look at neuronal network in 3D at a single cell resolution. The advantage of microscopy is that activity and morphology of the tissue can be inspected simultaneously. That opens doors for the establishment of a structure-function connection which occurs in many biological systems. Capabilities of the setup presented in this thesis are represented by a grey dot. The temporal resolution of the setup was limited by the used calcium indicator. It could be improved if a faster indicator was used: jGCaMP8 [77](see 5.2.1). Adapted from [78], [79]

2.5.2 Multi Electrode Array (MEA)

Neuronal electrical activity causes transient imbalances in ion in the intra- and extracellular space. Locally, a charge separation takes place which gives rise to a local electric field that can be detected with the use of an electrode or an entire grid of electrodes: multi electrode array.
In general two types of signals can be recorded :
• network oscillations of small neuronal populations: superposition of action potentials and synaptic potentials resulting in waves (duration: >10 ms, amplitude: from hundreds of μV to 1-2 mV, bandwidth: 1-300 Hz)
• fast current fluctuations due to spiking activity of individual neurons (duration: 0.5-2 ms, amplitude: hundreds of μV, bandwidth: 300-3000 Hz) [85].
Even though activity recordings obtained with this technique display a high spatio-temporal resolution, they are limited to 2D.

2.5.2.1 3D MEA

CMOS-based MEA in conjunction with Neuropixels CMOS shank probes [86] have been used to 3D characterize networks in human brain orgaonids [7]. Neuropixels probes can be inserted into the active tissue to record extracellular action potentials from individual neurons with a sub-millisecond temporal resolution.

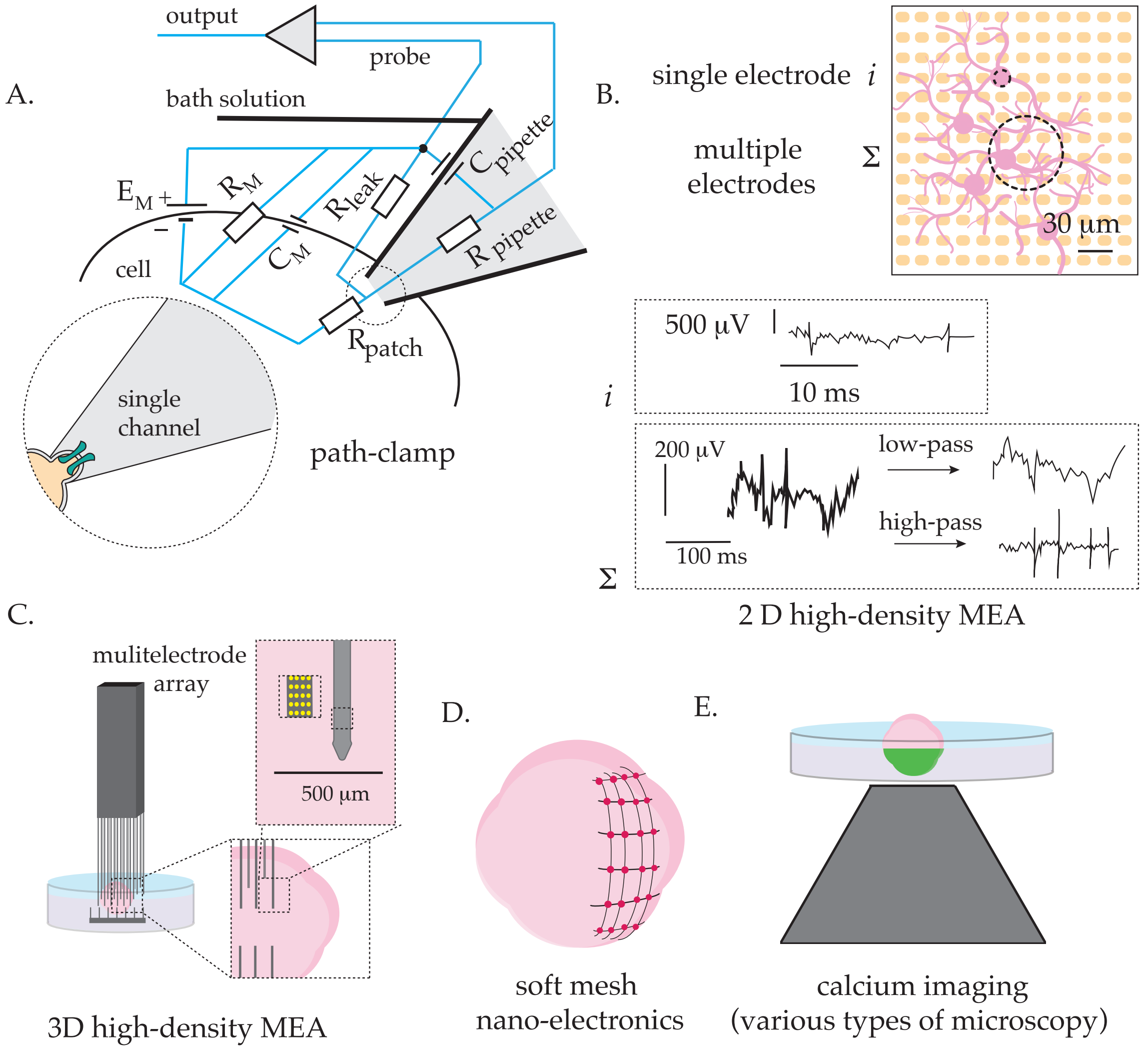

Figure 2.10: **Methods for electrophysiological recording A.** In the cell-attached path configuration, the potential difference between the pipette electrode and the bath electrode is measured via a voltage clamp circuitry. In case R_{Patch} >> resistance of the cell (R_M) and also R_{Patch} >> pipette ($R_{pipette}$) current flows through the patch and the trapped ion channel (zoom) can be monitored. The quality of the seal between the pipette and the patch is given by the leak resistance (R_{leak}) and is in practice of the order of 10 GΩ. C_M and $C_{pipette}$ represent the membrane and pipette capacitances which are both small. B. Grid of multi-electrode results in a chip on which 2D cell culture can be maintained. Each electrode can be address separately (i) to extract fast current fluctuations due to spiking activity of individual neurons. In addition, local field potentials resulting from superposition of action potentials and synaptic potentials (>10 ms duration, hundreds of μV in amplitude) extending over an area covered by multiple electrodes can be obtained (Σ) and the raw signal can be further filtered and decomposed into different contributions. C. CMOS-based 2D MEA in conjugation with CMOS shank probes with electrode pitch of about 20 μm allow for high spatio-temporal mapping of activity in 3D D. Integration of mesh stretchable nano-electronics into an organoid allows for a three-dimensional readout of its surface electrical activity throughout development. D. Variety of fluorescence microscopy techniques have been proposed to record neuronal activity reported by a wide range of calcium sensors. They offer the unique advantage of simultaneously recording network activity and its morphology in 3D in a non-invasive way. Inspired by [80, 7, 81, 82, 83]

2.5.2.2 Soft nano-electronics

Li et. al reported in 2019 the generation of *cyborg* human cardiac organoids with a mesh-like nano electronics sensor/stimulator integrated into their structure during organogenesis [81]. Authors argue that incorporated nano-electronics did not affect the 3D differentiation of iPSC-derived cardiac organoids and allowed to monitor the evolution, propagation and synchronization of the bursting dynamics throughout developmental stages of the tissue. The approach offers high spatio-temporal readout of activity in 3D, it seems for now it is limited to the outer surface of the structure. Similar work has been done by [87] where early-stage brain organoid development has been looked at. Further investigation of the influence the integration of the nano-electronics has on tissue growth should be conducted separately for each type of sample.

2.5.3 Readout : Interlude

Introduction of the role of calcium ions and ways to study their role in neuronal cells sets the stage to understanding the last set of techniques that will be mentioned in this thesis and that are used for electrophysiological recordings.

2.5.3.1 Ca^{2+} as a mediator of neuronal interactions

Calcium is involved in the regulation of a plethora of cellular processes and vital aspects of the cell cycle starting from cell proliferation and ending at cell death [88, 89]. It plays a key role in the transmission of neuronal signals and shaping synaptic plasticity [90].

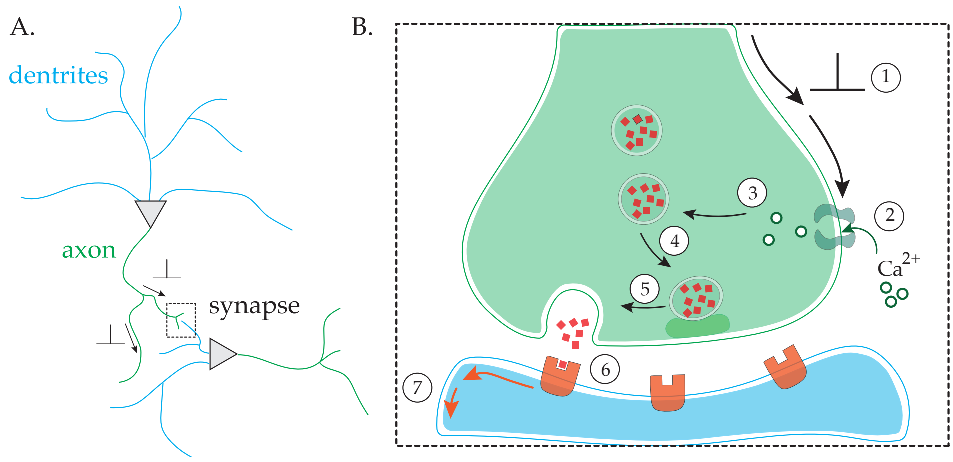

Figure 2.11: **Synaptic transmission in a chemical synapse A.** An action potential (symbolized by ⊥) travels down the axon of the pre-synaptic neuron to the dendrites of the post-synaptic neuron B. Neurotransmission process, zoom in to A: 1. The action potential reaches the axon's terminal which causes a local change in membrane potential. That results in a conformational change of voltage-gated Ca^{2+} channels 2. Ca^{2+} ions enter the presynaptic neuron through the open voltage-gated Ca^{2+} channels via Brownian flow 3. Ca^{2+} ions signal a vesicle storing neurotransmitter molecules 4. As a result, the vesicle binds to the docking protein 5. Neurotransmitter molecules are released from the synaptic vesicle to the synaptic cleft (space between the two synapses) via exocytosis 6. Neurotransmitter molecules bind to the receptors located on the post-synaptic membrane. 7. Signal is initiated in the post-synaptic neuron. Adapted from [91], [53], [92] and loretocollegebiology .

The influx of calcium in the presynaptic terminal gives the green light for the exocytosis of neurotransmitter-containing synaptic vesicles (for review, see [93]). The rise of calcium ion concentration is essential for the transmission of an action potential further in the network (Figure 2.11).

2.5.3.2 Track neuronal activity

Visualisation of neuronal activity, meaning electro-chemically mediated communication between neurons, in nervous tissues can be accomplished by following the flow of Ca^{2+}. One can do so with the use of calcium indicators that come in two flavours - chemical dyes or genetically modified and encoded proteins [25].

2.5.3.3 Use of calcium sensors

The challenge resides in introducing a Ca^{2+} reporter in the cell in an controllable and efficient way. Moreover, the selected reporter needs to have a K_d value, brightness and binding rate appropriate for the process one wants to study.

• chemical calcium sensors
Even though chemical calcium indicators have been optimized to offer a broad range of Ca^{2+} affinities, it is difficult to control their localization while introducing them into cell (loading process). In addition, this so called loading process can in itself be damaging to the cell. Finally, chemical reporters, tend to be extruded from the cell in the long term.

• genetically-encoded calcium sensors
On the other hand, genetically encoded calcium indicators can be introduced into the cell using non-invasive gene delivery methods [94]:
- virial delivery systems
- lipofectamine
- lipid nanoparticles (LNPs) as utilized in the recent mRNA vaccinines by BioNTech [95]

With these reagents, DNA or RNA of the calcium sensor is introduced in the cell and needs to be translated into a protein.

Another possibility is to modify the cell's DNA such that it produces the indicator on its own [96]. Both approaches, allow to some extent for a cell-type specific expression of the indicator.
With a control over the production of indicator molecules in the targeted structure and another method allowing to verify cell identity (for example counter-staining) one should be able to perform morphological characterization of cells in the system. Such analysis would be a step towards establishing the structure-function relationship.
In this work a fluorescent protein indicator has been used - R-GECO1. It has been created based off of a fluorescent protein mApple protein was fused to Ca^{2+} sensing domain (calmoduin) [97] in the process of directed evolution in which random mutations are introduced in the gene of interest to induce changes in the protein properties. Binding of Ca^{2+} results in a conformational change of the sensor protein

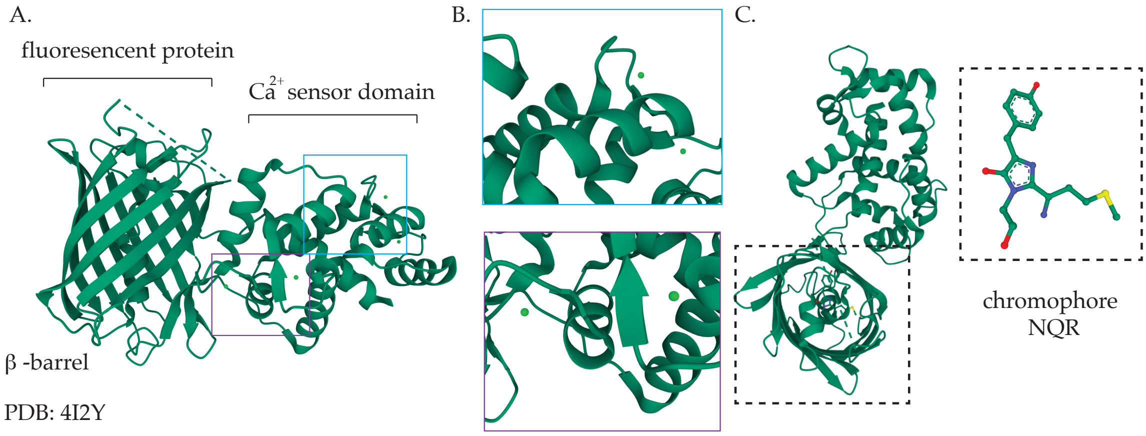

Figure 2.12: **RGECO1 sensor A.** Structure of the protein in the cartoon representation. Two parts can be distinguished : a fluorescent part (β -barrel structure represented by thick arrows with a chromophore molecule nestled inside) and the Ca^{2+} sensor part formed by EF-hand motifs (helix-loop-helix) B. each accomodating one ion (green balls). C. Rotated view of the protein, the dashed box shows the cross section of the β -barrel which hosts the chromophore (NQR).

and change of the protonation state of the chromophore molecule it contains. As a consequence a rise in fluorescence can be observed.

Only a simplified model of Ca^{2+} binding, that does not include the conservativity, will be briefly discussed. The reader is encouraged to find out more about this topic in chatper 12 of [98].
Entry of Ca^{2+} that accompanies an action potential can be written as:

$$\mathrm{Ca}^{2+} + \mathrm{B} \underset{\mathrm{k_{off}}}{\overset{\mathrm{k_{on}}}{\rightleftharpoons}} \mathrm{CaB} \tag{2.9}$$

where B represents a molecule (either naturally present in the cellular environment or introduced artificially) with a Ca^{2+} binding site and CaB is a calcium-bound complex which associate with a rate constant k_{on} $(mM^{-1}s^{-1})$ and dissociates with k_{off} (s^{-1}). The ratio $\frac{k_{off}}{k_{on}}$ defines the so-called dissociation constant K_d of process 2.9, is equal to the level of $[Ca^{2+}]_i$ (intracellular free Ca^{2+} concentration) for which half of the available Ca^{2+} binding sites are occupied.

The reverse of K_d defines the associative constant K_{as}, which decribes the level of Ca^{2+} at which a complex molecule forms. For example, for a B molecule with high affinity to Ca^{2+}, the binding process is characterized by a high K_{as} and a as consequence low a K_d.

The dynamic range of Ca^{2+} changes that can be monitored with calcium indicators depends tremendously on the indicator's affinity to Ca^{2+} and the range of Ca^{2+} concentration changes in the monitored process. If B is assumed to be the calcium indicator used in the experiment, its affinity has to match the levels of Ca^{2+} that are characterizing the system and expected to be monitored in the experiment. Too high affinity will result in instant saturation of the indicator - too low affinity will provide a non-sufficient signal to noise.

Resting intracellular level of Ca^{2+} is $< 10^{-4}$ mM and high about 0.1 mM (at the site of a Ca^{2+} influx during an action potential) High affinity 0.2-0.3 μM and low affinity are said to be about 50μM [98]. The indicator used in this work, R-GECO1, has a K_d of 0.48 μM [99].

2.5.4 Readout: Optical studies

It is now time to present the optical methods of recording neuronal activity, visualization of which is enabled by calcium indicators - fluorescent molecules that increase their quantum yield upon binding calcium ions and can thus report on intracellular calcium concentration.

If the calcium influx is assumed homogenous throughout the cell compartment and its duration is short compared to process resulting in calcium extrusion, it can be approximated by a pulse-like influx, well expressed using the Kronecker delta function:

$$j_{inside} = \Delta[Ca^{2+}]_T \, \delta(t - t_p) = \frac{Q_{Ca^{2+}}}{2FV} \, \delta(t - t_p) \tag{2.10}$$

where $\Delta[Ca^{2+}]_T$ is the total change in Ca^{2+} concentration in the cell (in free or bound form), t_p is the time at which the pulse happens, $Q_{Ca^{2+}}$ is the total charge that enters the cell during a given time period, F is the Faraday's constant and V the volume of cellular compartment.

In case multiple pulses reach the cells (a train of n spikes) 2.10 can be extended to a sum of delta functions with t_p running from 1 to n.

$$\mathrm{j_{inside}} = \frac{\mathrm{Q_{Ca^{2+}}}}{2\,\mathrm{FV}} \quad \sum\nolimits_{\mathrm{p}=1}^{n} \delta(\mathrm{t}\text{-}\mathrm{t}_p) \tag{2.11}$$

Calcium imaging has been implemented in various microscopy schemes (review on strategies for volumetric microcopy techniques and *in vivo* calcium imaging [100, 101]).
A list of some of the ingenious setups that have been employed to optically study neuronal activity in small animals, model systems and artificially generated samples is presented in Table 2.2 The diversity and multitude of approaches demonstrates how very active this field of research is. One of the categories in Table 2.2 is the transparency of the imaged sample which has been color-coded as non-transparent ($-$) and transparent ($+$). Shape of light-sheet along the illumination axis can change depending on the sample properties. The illumination profile degrades in an opaque sample. Because of that, it is more challenging to image a non-transparent sample $-$. For that reason a red colour has been selected to indicate setups that have assumed this challenge. The FOV in the table is for the majority of entries 3D. However, in the work of Samarasinghe et al. [28] and Cowan et al.[26] a 2D FOV was used.

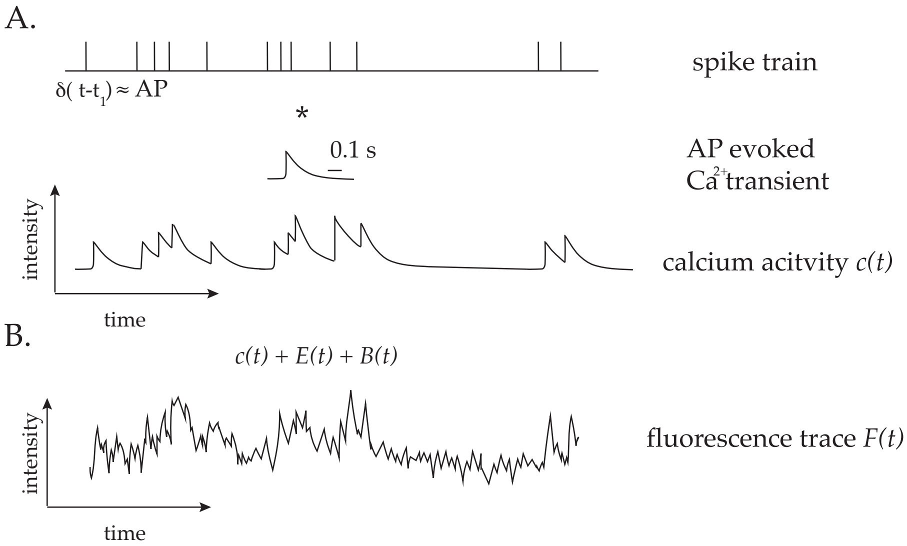

Figure 2.13: **From a spiking trains to a fluorescence trace A.** Series of action potentials (a spike train) when reported by a calcium indicator, can be represented as convolution of delta functions with the response function of the indicator. B. In an experimental setting, the fluorescence trace is recorded along with noise E(t) and background B(t) which makes the extraction of spiking trains challenging. This problem will be addressed in section 2.7.

Point-scanning:

Imaging strategies can involve point scanning of a sample of interest for example using confocal microscopy and two-photon scanning microscopy. However, these approaches do not allow for high volumetric acquisition rates necessary to study fast 3D neuronal dynamics.

Scanned focus:

In standard fluorescence microscopy, an increase in image acquisition rates can be achieved when beam scanning is performed by an optical element such as electrically tunable lenses. However, out-of-focus light is inherently part of such images as no optical sectioning mechanism is implemented. Numerical removal of such background is possible when structured illumination is used. However, the need to take multiple images per plane decreases the volumetric rate.

Multi focus:

In case the sample is weakly scattering and rather transparent, entire volumes can be captured in a light field microscopy setup. Here, light emitted from different depths in the sample is projected on the camera chip via a micro lens array. Signals can be plane de-mixed using three-dimensional deconvolution algorithms. Dynamics of extremely fast systems can be captured at the cost of spatial resolution degradation. This can be mitigated by the introduction of sectioning capabilities, for example a pinhole at the detection site.

Extended Focus:

In extended depth of focus (EDOF) imaging, use is made of an engineered PSF, designed to be axially extended. This can be achieved by means of masks modulating the wavefront of the fluorescence. Within one camera exposure, a focal sweep is performed that results in the collection of images superimposed at all depths with in the volume. Images can then be mapped to concrete planes using deconvolution algorithms. Still, it is possible to the extend that the readout is not dominated by out-of-focus background.

Scanned focus with intrinsic optical sectioning: light-sheet microscopy:

Focused and virtually background free 2D images are acquired in sequence either by physically, axially translating the sample or axially scanning an illumination beam across the sample. Volumetric functional data can be acquired with a cellular axial resolution.

Table 2.2: **Optical techniques for capturing neuronal activity**

Type	**FOV** (μm^3)	**Rate (Hz)**	**T**[3]	**Cx**[4]	**Ref**
LS	665 x 665 x 60	5	−	low	**this work**
Confocal	NA	NA	−	comm	**Lancaster** et al. [3]
laser scanning STM	200 x 200	NA	−	comm	**Cowan** et al. [26]
laser scanning STM	—	NA	−	comm	**Sakaguchi** et al. [27]
laser scanning STM	500 x 500	NA	−	comm	**Samarasinghe** et al. [28]
LS	800 x 600 x 200	0.8	+	high	**Ahrens** et al. [46]
LS	1000 x 800 x 40	5	+	high	**Panier** et al. [36]
LS	≈ 830 x 430 x 200	2-3	+	high	**Vladimirov** et al. [40]
1P and 2P LS	500 x 200 x 200	5	−	high	**Lemon** et al. [42]
LMF	≈ 830 x 430 x 200	20	+	low	**Prevedel** et al. [41]
2P with TeFo	500 x 500 x 500	5.7	−	high	**Prevedel** et al. [32]
LFM with EDoF	416 x 832 x 160	33	+	high	**Quirin** et al. [29]
SCAPE	392 x 299 x 41	10	−	high	**Bouchard** et al. [45]
SCAPE	392 x 299 x 41	25.75	+	high	**Voleti** et al. [39]
LFM AI-enchanced	≈ 350 x 280 x 120	10	+	high	**Wagner** et al. [37]
OCPI	223 x 127 x 200	20	+	high	**Greer** et al. [43]
2P with elongated focus	270 x 270 x 100	30	+	low	**Lu** et al. [102]
2P with CADoF	366 x 214 x 66	60	+	low	**Lu** et al. [103]
confocal LFM	⊘ 800 x 200	6	+	high	**Zhang** et al. [38]
2P with ETL	500 x 500 x 100	4	+	high	**dal Maschio** et al. [35]
epi-fluorescence with ETL	500 x 500 x 200	10	−	high	**Xiao** et al. [104]
2P with ETL	500x 500 x 450	10	−	high	**Han** et al. [34]
HyMS with TeFo	765x 665 x 800	≈ 4.3 - 13	−	high	**Weisenburger** et al. [31]
TPM with OPLUL	375 x 112 x 130	14	−	high	**Kong** et al. [47]
LS	NA	1.5	+	high	**Markov** et al. [33]
LBM	≈ 600 x 600 x 500	≈ 10	−	high	**Demas** et al. [44]
light-sheet with ETL	≈ 668 x 384 x 140	25	+	high	**Loza-Alvarez** et al. [105]
miniaturized 2P	≈ 510 x 510 x 40	7.5	−	high	**Zong** et al. [30]
LS	500 x 300 x 200	3.3	+	high	**Yang** et al. [106]

comm = commercially available setup
low = add-on to a microscope
high = complete stand alone custom setup
LS = Light-sheet
STM = Scanning Two-photon Microscopy
SCAPE = Swept Confocally-Aligned Planar Excitation
OCPI = Objective Coupled Planar Illumination
TeFo = Temporal Focusing
EDoF = Extended Eepth of Field
ETL = Electrically Tunable Lens
CADoF = Continuously Adjustable Depth of Focus
LFM = Light Field Microscope
2PLSM = 2-Photon laser scanning microscopy
HyMS = Hybrid Multiplexed Sculpted Light Microscopy
OPLUL = Optical Phase-Locked Ultrasound Lens
LBM = Light Beads Microscopy

2.6 Resolution: Light-sheet microscopy

In light-sheet microscopy, a thin slice within a fluorescent specimen is illuminated with a laser beam shaped such, that it locally approximates a plane of light. Light emitted by fluorophore molecules excited within the slice is collected by a detection objective commonly localized at a right angle with respect to the illumination. Thanks to the illumination's geometry, the image of only a thin focal volume of the sample is generated. This grants intrinsic optical sectioning and at the same time allows to tremendously speed up acquisition compared to point-wise sample scanning. Moreover, in such illumination schemes, the potential photodamage the sample may suffer is reduced.

Perpendicular illumination was first put forward in 1902 by Siedentopf and Zigmondy to image colloidal particles by eye [107]. Implementation of such illumination for fluorescent imaging was done over 90 years later by Voie et al. to image the internal architecture of the cochlea [108]. Later Huisken et al. idesigned selective plane illumination microscopy (SPIM) to capture *in vivo* the embryogenesis of the *Drosophila melanogaster* [109].

2.6.1 Light-sheet described as a Gaussian Beam

A static light-sheet can be described using the approximate but analytical solution to the paraxial wave equation which captures well the plane and spherical wave characteristics of a light-sheet illumination where the light mainly propagates in one direction and slowly diverges in two others. The reader is encouraged to consult the chapter of *Laser Electronics* by J.T. Verdeyen [110] for deeper insights into the subject of Gaussian Beam description, on which this discussion is based.

First, for a source free region the Gauss law in isotropic homogenous media can be written as:

$$\vec{\nabla} \cdot \vec{D} = 0 \Rightarrow \vec{\nabla} \cdot \vec{E} = 0 \tag{2.12}$$

where $\vec{D}$ and $\vec{E}$ are respectively the electric displacement vector (electric flux density) and the electric field vector. The divergence operator $\vec{\nabla}$ can be split into the transversal ($\vec{\nabla}_t$) and longitudinal ($\frac{\partial}{\partial z}$) component such that equation 2.12 can be re-written as:

$$\vec{\nabla}_t \cdot \vec{E}_t + \frac{\partial E_z}{\partial z} = 0 \tag{2.13}$$

where $\vec{E} = \vec{E}_t + E_z \hat{z}$ are respectively transverse and longitudinal components of the electric field and $\hat{z}$ is the unit vector in the longitudinal direction. Assuming that for visible wavelengths ($0.4\,\mu m \lesssim \lambda \lesssim 0.7\,\mu m$) the longitudinal electric field component E_z can be neglected as compared to the transverse electric field component, the solution to 2.13 is sought in the form

$$\vec{E}(x, y, z) = \hat{t}\, E_0\, \psi(x, y, z)\, e^{-ikz} \tag{2.14}$$

[3]Transparency (of the imaged sample)

[4]Complexity (of the setup)

where $\hat{t}$ is the unit vector in the xy plane (transverse direction) independent of x, y, z coordinates, E_0 is the amplitude factor accounting for the intensity of the wave, e^{-ikz} captures the propagation behaviour of the wave which corresponds approximately to a uniform plane wave and ψ measures the deviation from this expected behaviour. In addition, it is expected that 2.14 satisfies the time-independent wave equation - the scalar Helmholtz's equation:

$$\nabla^2 E + k_0^2\, n^2\, E = 0 \tag{2.15}$$

where the wavenumber $k = (2\pi n)/\lambda_0$, n is the medium refractive index and λ_0 is the freespace wavelength. Upon inserting the electric field in the form of 2.14 into 2.15 it is found that:

$$\nabla_t^2\, \psi - i2k\frac{\partial \psi}{\partial z} + \frac{\partial^2 \psi}{\partial z^2} = 0 \tag{2.16}$$

If the variation of ψ along z is slow, meaning that $|\partial^2\psi/\partial^2 z| \ll 2k|\partial\psi/\partial z|$, the second derivative term in 2.16 can be neglected and the paraxial wave equation is obtained:

$$\nabla_t^2\, \psi - i2k\frac{\partial \psi}{\partial z} = 0 \tag{2.17}$$

The solution to 2.17 adopts the form $\psi = \psi(r_t, z)$ where $r_t = \sqrt{x^2 + y^2}$ is the transverse radial distance away from the beam's axis. The solution is built from three factors:

$$E(r_t, z) = \overbrace{E_0 \frac{w_0}{w(z)}}^{amplitude\ factor} \underbrace{e^{-\frac{r_t^2}{w^2(z)}}}_{longitudinal\ phase\ factor} \overbrace{e^{-i\left(kz - tan^{-1}\left(\frac{z}{z_R}\right)\right)}\, e^{-i\frac{kr_t^2}{2R(z)}}}^{radial\ phase\ factor} \tag{2.18}$$

where $R(z) = z\left(1 + \left(\frac{z_R}{z}\right)^2\right)$ is the radius of curvature of equiphase surfaces of the wave fronts. As for w_0 and z_R, they are respectively the waist ("minimum spot size") of the Gaussian beam and the distance along which the depth of the light-sheet increases to $2\sqrt{2}\omega_0$, so called Rayleigh length (z_R): relation between them can be found for the profile of the Gaussian Beam in the transverse direction (meaning when $\psi(r_t, z = 0) = e^{-r_t^2/w_0^2}$)

$$w_0^2 = \frac{2z_R}{k} = \frac{\lambda_0 z_R}{n\pi} \Rightarrow z_R = \frac{\pi n w_0^2}{\lambda_0}, \tag{2.19}$$

where λ_0 is the free space wavelength. The general description of the divergence of the spot size along the propagation axis z is given as the hyperbolic relation:

$$w(z) = w_0 \sqrt{1 + \left(\frac{z}{z_R}\right)^2} \tag{2.20}$$

The solution $E(r_t, z)$ 2.18 constitutes the lowest order Gaussian Beam.

The waist of the light-sheet w_{LS} and Rayleigh length z_{LS} in an experimental setup close to the focus can be estimated with the knowledge of the illumination numerical aperture ($\mathrm{NA_{ill}}$) as proposed in [111]:

$$w_{LS} = 2\omega_0 = 2\left(\frac{\lambda_{ill}}{\pi \mathrm{NA}_{ill}}\right). \tag{2.21}$$

$$z_{LS} = 2 z_R = 2\left(\frac{\pi\, n\, w_0^2}{\lambda_{ill}}\right). \tag{2.22}$$

where λ_{ill} is the illumination wavelength. It is crucial to note that the thickness of the light-sheet decides the optical sectioning capabilities of the system and its axial resolution.

2.6.2 Optical Resolution

In this section, theoretical and experimental concepts used to evaluate the resolution will described.

2.6.2.1 Point Spread Function

Imaging capabilities of an imaging system are usually evaluated with the use of a point spread function (PSF), which is the response of the system to a point source of light. Electronic image sensors such as CMOS used in this thesis, are sensitive to light's intensity, therefore it is the intensity PSF $H(x, y, z)$ that is exploited to obtain the object's image

$$H(x, y, z) = h^*(x, y, z) h(x, y, z) = |h(x, y, z)|^2 \tag{2.23}$$

where $h(x, y, z) = |h(x, y, z)| e^{i\,\phi(x,y,z)}$ is the amplitude PSF that captures the phase (ϕ) of the electric field oscillation at the position $x,\ y,\ z$.
A fluorescent object can be thought of as a structured collection of individual point light sources. Microscope's optics convolves each point source $O(x, y, z)$ with the systems intensity PSF $H(x, y, z)$, which yields the object's image $I(x, y, z)$ as

$$I(x, y, z) = O(x, y, z) * H(x, y, z) \tag{2.24}$$

The shape of the 3D intensity PSF can be approximated by a 3D Gaussian with its lateral and axial extent σ_{xy} and $\sigma_{z,sys}$ predicted by the Stelzer-Grill-Heisenberg (SGH) theory for circular apertures [112, 113]:

$$\sigma_{xy} = \frac{\lambda_{det}}{n\sqrt{3 - 2\cos\alpha_{det} - \cos 2\alpha_{det}}} \tag{2.25}$$

$$\sigma_{z,sys} = \frac{1}{\sqrt{\frac{1}{\sigma_{z,ill}^2} + \frac{1}{\sigma_{z,det}^2}}} \tag{2.26}$$

$$\sigma_{z,ill} = \sqrt{\frac{3\lambda_{ill}\, 2\, z_R}{8\pi}} \tag{2.27}$$

$$\sigma_{z,det} = \frac{\lambda_{det}}{n\,(1 - \cos\alpha_{det})} \tag{2.28}$$

where α is the half opening angle of the illumination or detection in radians, which is given as the $\arcsin(\mathrm{NA}_{ill}/n)$ or $\arcsin(\mathrm{NA}_{det}/n)$.
Experimentally, radial and axial profiles of the intensity point spread function of the setup can be measured by imaging sub-diffraction-sized fluorescent beads. Their $\frac{1}{e^2}$ radius along corresponding axis gives a measure of the x,y and z resolution.
Evaluation for the setup will be presented in the result section 7.

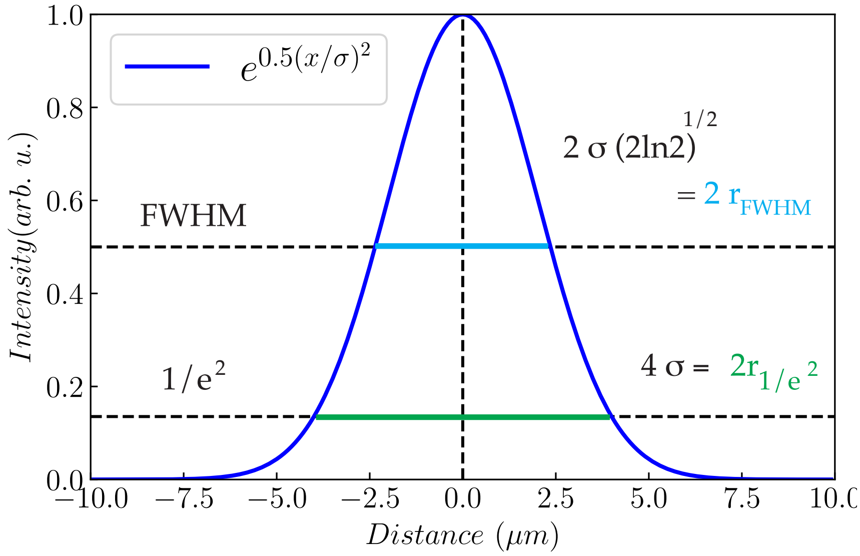

Figure 2.14: **1D gaussian as a model of 3D PSF intensity.** Two commonly used measures to characterize a Gaussian peak are its full width at half maximum (FWHM) and its $1/e^2$ diameter, which can be expressed in terms of the peak's width σ as $2\sigma\sqrt{2\ \ln 2}$ and $4\,\sigma$ respectively.

2.6.3 Scanning of the Sample

Two types of sample illumination for functional imaging can be distinguished:
• **scanning beam** illuminates an immobile sample with the use of an electro-optic element (i.e. galvo mirror system),
• **static beam** illuminates consecutive planes within a sample displaced perpendicularly with the use of a stage (i.e. piezo-electrically driven stage).

2.7 Analysis: of calcium imaging data

The advantage of using calcium imaging for neuronal networks activity studies is the ability it gives to simultaneously monitor large, complex neuronal structures at a single cell level at, in principle, single action potential resolution. However, the extraction of this information from large and often noisy images turns out to be challenging. Among popular softwares used for calcium imaging data analysis are SIMA [114], CNMF-E [115], Suite2p [116], ABLE [117], SCALPEL [118], MIN1PIPE [119], SamuROI [120] and CaImAn [48].

2.7.1 What should the software be able to do?

Main expectations towards the software are that it should:

1) correct for motion artefacts that commonly occur for live samples imaged over prolonged periods of time
2) segment images into regions of interest that often overlap and show different signal-to-noise ratios depending on their position in the field of view
3) automatically extract fluorescence signal for each region of interest (the signal can have an amplitude significantly smaller than the noise present in the image)

4) deconvolve the spiking activity from the calcium indicator dynamics.
And finally, the last point crucial for this work:
5) perform 1)-4) not only for 2D (single plane) but also 3D data (volumetric data).

A software that offers a robust pipeline that covers steps 1)-5) is CaImAn (**Ca**lcium **Im**aging data **An**alysis) toolbox [48].

2.7.2 Mathematical formulation of CaImAn

CaImAn employs the concept of matrix factorization to reduce the dimensionality of calcium imaging data and decouple temporal and spatial components. In general, the goal of matrix factorization is to approximate the data matrix V as $V \approx WH$, where W and H are non negative factors (Figure 2.15). This is because both the spatial footprints as well as their temporal components should not adopt negative values. This method has been initially proposed and applied for parts-based representation of faces and semantic features of text [121, 122].

In our case, spatio-temporal fluorescence data is decomposed into an outer product of i) a spatial matrix, that stores spatial footprints of active neurons in the field of view and ii) a temporal matrix, that describes the calcium concentration of identified neurons as function of time. In addition, background and noise terms of the same dimensionality as the raw data matrix are included to explain the remaining fluorescence signal in the field of view. Importantly, spatially overlapping neurons can be separated and their activity de-mixed. This is not possible in case when linear decomposition into independent components is sought (like in case of Principal Component Analysis(PCA) / Independent Component Analysis (ICA))

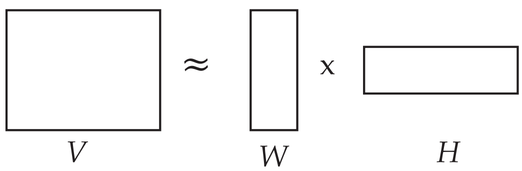

Figure 2.15: **Graphical representation of matrix factorization** where matrix V is decomposed into two smaller matrices W and H which upon mulitplication will best approximate V.

Calcium imaging data have several characteristical features that stem from the nature of the studied object, which allow to impose constraints on matrices W and H which we look for, namely:

- size of the fluorescence sources correspond to a neuron soma
- behaviour of fluorescence is dictated by the dynamics of the calcium indicator
- non-negativity of activity traces

Taking these constraints into account allows to find an elegant representation of the data where it is separated into defined contributions[123], [48] in the following form:

$$Y = AC + B + E \tag{2.29}$$

where:
- $Y \in \mathbb{R}^{dxT}$ is the observed data written in a matrix form with d being the total

number of pixels/voxels and T the number of acquired time points
- $A \in \mathbb{R}^{dxN}$ stores the spatial footprints of N active neurons in the FOV in the form $[\mathbf{a}_1, \mathbf{a}_2, ..., \mathbf{a}_N]$, $\mathbf{a}_i \in R^{dx1}$
- $C \in \mathbb{R}^{NxT}$ stores the temporal components in the form $[\mathbf{c}_1, \mathbf{c}_2, ..., \mathbf{c}_N]^T$, where individual components $\mathbf{c}_i \in R^{Tx1}$
- $B \in \mathbb{R}^{dxT}$ is the background matrix, which is modeled as $B = \mathbf{bf}$, where $\mathbf{b} \in \mathbb{R}^{dxn_b}$, $\mathbf{f} \in \mathbb{R}^{n_b xT}$ are respectively the matrices of spatial and temporal background components and n_b is the number of background components, more components can be used to model a more complex background signal
- $E \in \mathbb{R}^{dxT}$ is the noise term modeled as zero mean Gaussian with variance σ^2

2.7.3 Graphical explanation of CaImAn algorithm

To illustrate better how the concept of matrix factorization is used here, a simple example of a small (9 pixels in total) 2D field of view can be looked at (Figure 2.16). Numbers can be assigned to pixels in 2D time series (xyt stack). One can notice that major intensity changes over time take place for pixel # 5 where the soma of the neuron is located. If intensity over time for pixel #5 is extracted and plotted, it will resemble some sort of rise and decay function (see section 2.7.5.1). To filter out the background and noise present in the xyt data and extract the neuronal activity which is of interest, FOV at each time point t is linearlized to a vector and stored in matrix Y, which is then decomposed into the three terms: the spatio-temporal neuronal activity matrix $a_i\, c_i^T$ (where i runs over identified components), the background B and the noise E.
In a more complicated case, when a second neuron can be placed in to FOV (Figure 2.17), the observation can be made again that the neuronal activity is best captured by the intensity over time change of pixels #5 and #6.
The A matrix will then store two columns representing the footprints of identified neurons and the C matrix their respective activity traces - their product yields the filtered spatio-temporal activity. Authors show the algorithm achieves near-human performance in identifing active neurons in the FOV. F1 scores [5] are respectively around ≈ 0.85 for human labeler and ≈ 0.76 for CaImAn.

2.7.4 Image preprocessing

Pre-processing steps before signal extraction include filtering and motion correction. How and why these two are performed will be described below.

2.7.4.1 Filtering

Background of different type and intensity is present in calcium imaging data depending on the microscopy technique used to obtain it.
For example, in the case of two-photon data the background is reduced, as the near simultaneous absorption of two photons by the same molecule is required to access a given excited state [124] which in turn reduces the excitation volume compared

[5] F1 score combines presision and recall and is a measure of test's accuracy.

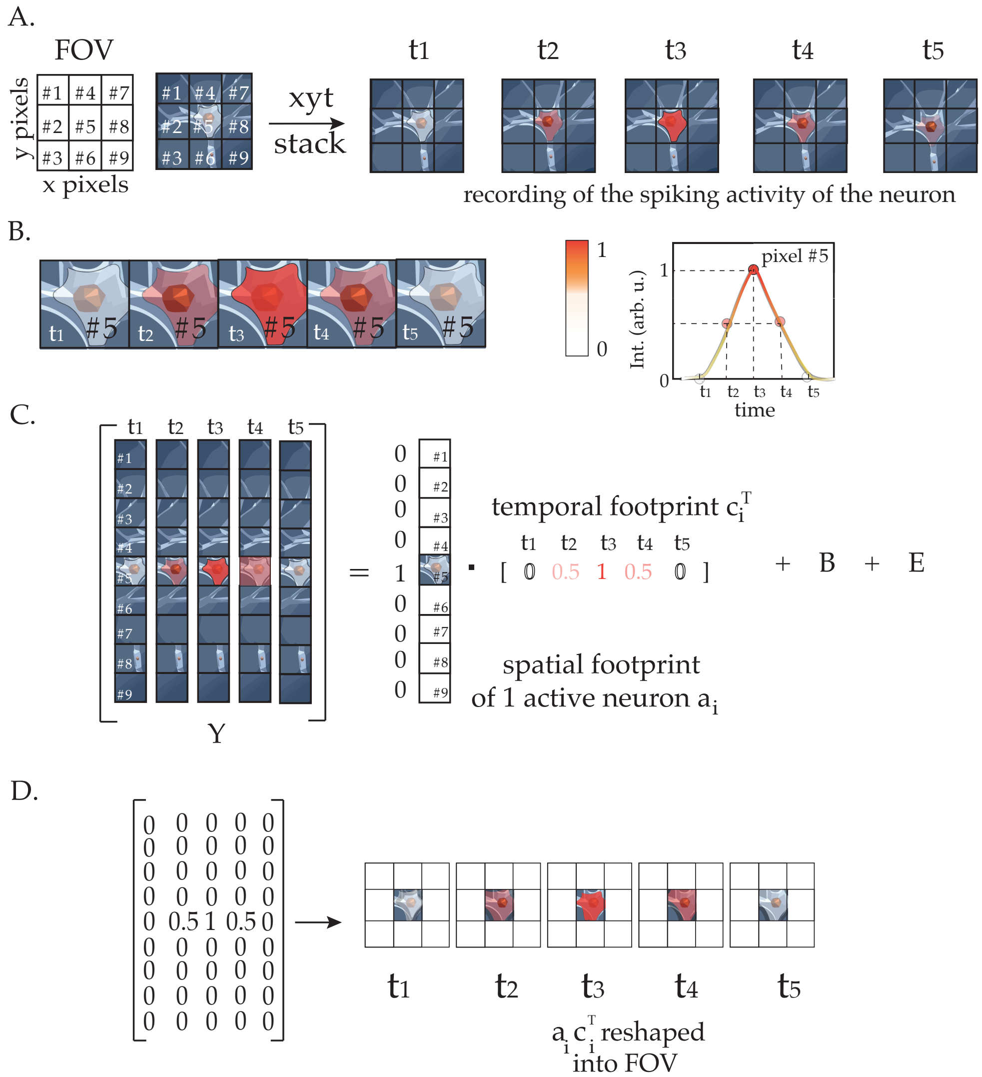

Figure 2.16: **Simplified explanation of the CNMF algorithm** with the steps taken during CNMF procedure. A. The spiking behaviour of an active neuron located in a small FOV (3 pixel x 3 pixel) is captured at different time points during 2D calcium imaging. B. Upon inspection, it is clear the main change in pixel intensity occurs for pixel # 5 where the cell body is located. The fluorescence over time can be extracted and plotted for this pixel. C. The 2D FOV at different time points t can be linearized and stored in a matrix that can then be decomposed into 3 contributions: (1)$a_i c_i^T$ product of a spatial component a_i that encodes the location and shape of the active neuron i (in this case the neuron is recapitulated by including only pixel # 5 with the neurons temporal component c_i^T that describes the calcium activity over time of the component a_i,(2) background term B and (3) noise term E. D. The extracted spatiotemporal activity a_i c_i^T can be reshaped back to the original dimensions of the FOV free from the background and noise contributions.

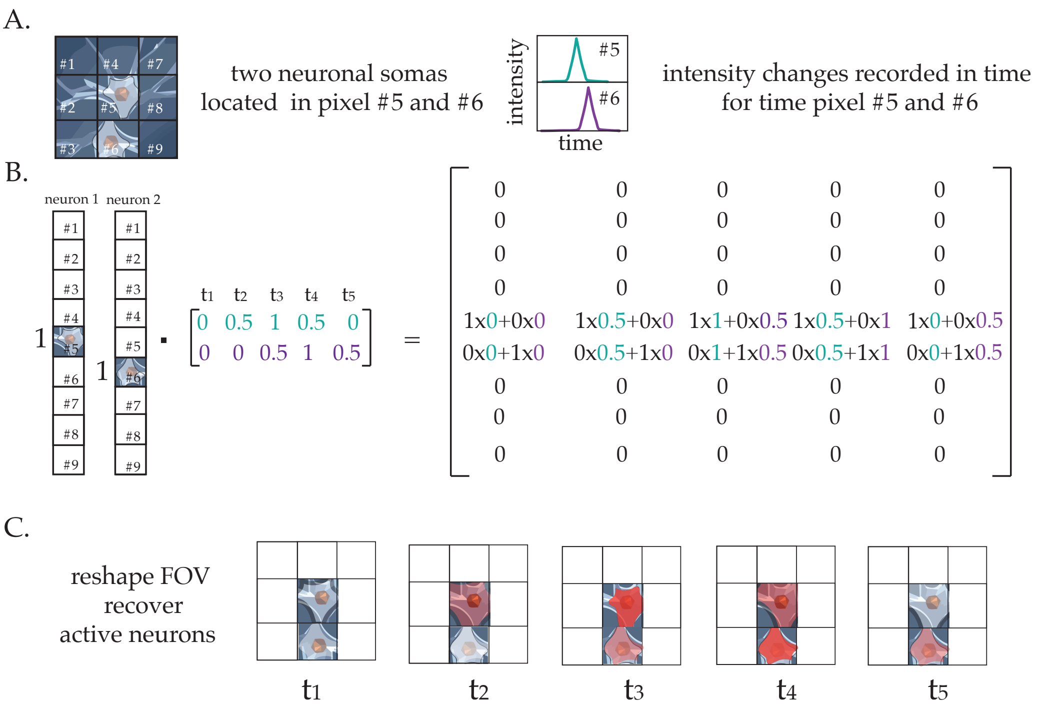

Figure 2.17: **CNMF performance when multiple neurons are present in the FOV A.** Pixels belonging to the each neuron are identified (even in case of an overlap). B. In this simple example, activity of the two neurons can be sufficiently captured when limiting their spatial footprint to pixels #5 and #6 respectively. C. The reshaped *AC* explains the observed spiking activity in the most efficient way. Importantly close or even overlapping neurons can be separated.

to the one of single-photon absorption. Light sheet data offers intrinsic optical sectioning with little to moderate out-of-focus light reaching the camera chip. When the background can be explained by global fluctuations of the FOV, the approach described above performs well for small FOV. For larger FOV, the data can be split into smaller patches and analyzed in parallel. This model can be used for two-photon and light-sheet data, both of which show low background.
However in case of the light-sheet microscopy data presented in this thesis, the background turns out to be high compared to the intensity of the activity signal (neuron firing), the reason for that being a relatively low brightness (product of quantum yield and absorption cross-section)[6]. As a result, some of the events are "sucked" into the background. Zhou et al. [115] developed and successfully applied an extended model for the background in microendoscopic data, which resembles the background displayed in the data obtained in this work. Unfortunately, this model has not been extended for 3D analysis.

2.7.4.2 Background signal removal

To partially remove some of the background signal, low-frequency contributions were filtered out using a simple Fourier filter (Figure 2.18). Low frequency signals were excluded with an adjustable circular mask applied to the Fourier domain image of individual input images, effectively setting pixels laying inside the circle to zero. Next, the resulting image was inverse transformed (IFFT) to yield a filtered image

[6]for values of brightness of RGECO1 see https://www.fpbase.org/protein/r-geco1/

(Figure 2.18). This way, only smaller objects that have the potential of being active neurons should remain in the FOV.

After that, a model dedicated to low background data, such as 2-photon calcium imaging was applied.

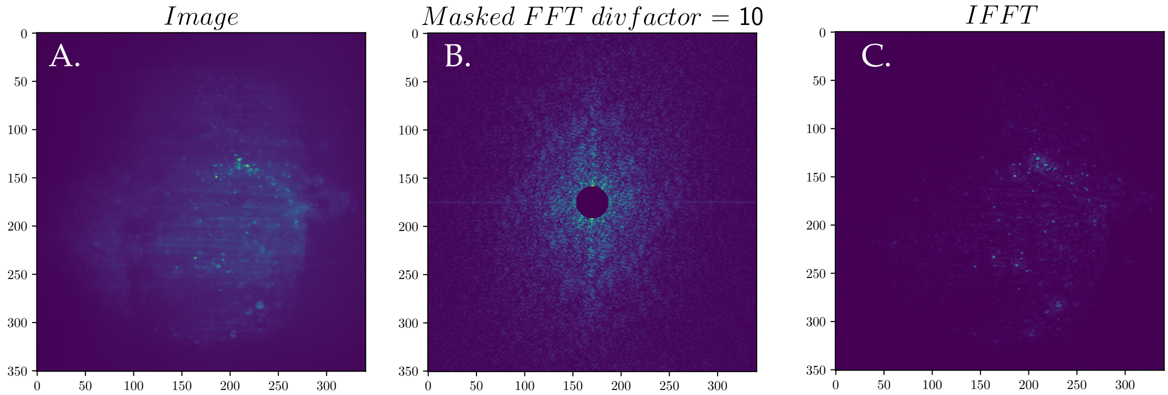

Figure 2.18: **Example of the filtering procedure A.** The original image is fast Fourier transformed to remove low frequencies contributions by B. masking them with an adjustable circular mask. C. In the next step, the filtered image is transformed back to the time domain via an Inverse Fast Fourier Transform.

2.7.4.3 Why is motion correction needed?

When performing functional imaging of live tissues one has to take into account that the sample can move in the field of view even if steps are taken to restrict the movement by applying some sort of sample-immobilization methods. Motions can include translations, rotations (rigid transformations) as well as change of shape and size of the sample (non-rigid transformations).
In this work, the sample was not fixed (for example in agarose) therefore natural tissue movements are possible. In addition, to acquire volumetric functional stacks the sample is moved by the piezo-stage along z-axis at 5 Hz through what can cause additional motion.

2.7.4.4 Magic of NoRMCorr algorithm

For motion correction, CaImAn implements NoRMCorr algorithm which belongs to the family of template matching algorithms [125] and has the advantage of being able to compensate for both rigid and non-rigid deformations.

2.7.4.5 Setting up the algorithm

The algorithm is set to operate in a piecewise fashion. First, a template is created as a median of the first few data frames along the t axis or a set of random frames.

step 1: rigid motion correction
Registration is the process of aligning the frame to the template and calculating displacement vector between the frame and the template for rigid motion correction. Each frame is registered against the template to correct for rigid deformation.

step 2: non-rigid motion correction
The FOV is split into multiple overlapping patches that are each aligned to the corresponding part of the template. Importantly non-rigid deformation along all axes (x,y,z this case) can be accounted for. By up-sampling the grid of patches, smooth motion field for each frame generate and the patches can be merged together into a coherent image by smooth interpolation.

2.7.4.6 How is the frame aligned to the template?

Optical pattern recognition followed by image matching can be achieved using correlation techniques. For example, to know if a small patch (P) (Figure 2.19) is part of the a frame template (T), one can compare the two images by "sliding" the patch across the other template. The centre of the patch is placed at each position (i, j) in the template - at each time the similarity between the patch and the (effective) part of the template (that has the same shape and size as the patch) is compared- the measure of this similarity is the correlation coefficient, which can be written as

$$c(i, j) = \mathbf{p}^T \mathbf{t}(i, j) \tag{2.30}$$

where $\mathbf{p}$ is a vector containing the pixel values of the patch and $\mathbf{t}$ a vector containing the pixel values of the "window" in the template that the patch is being matched to and which has the same shape and size. When this product is computed for all positions (i, j) in the template an output image $J(i, j)$ forms.

$$J(i, j) = \sum_{x=-h}^{h} \sum_{y=-h}^{h} T(i + x, j + y)P(i, j) \tag{2.31}$$

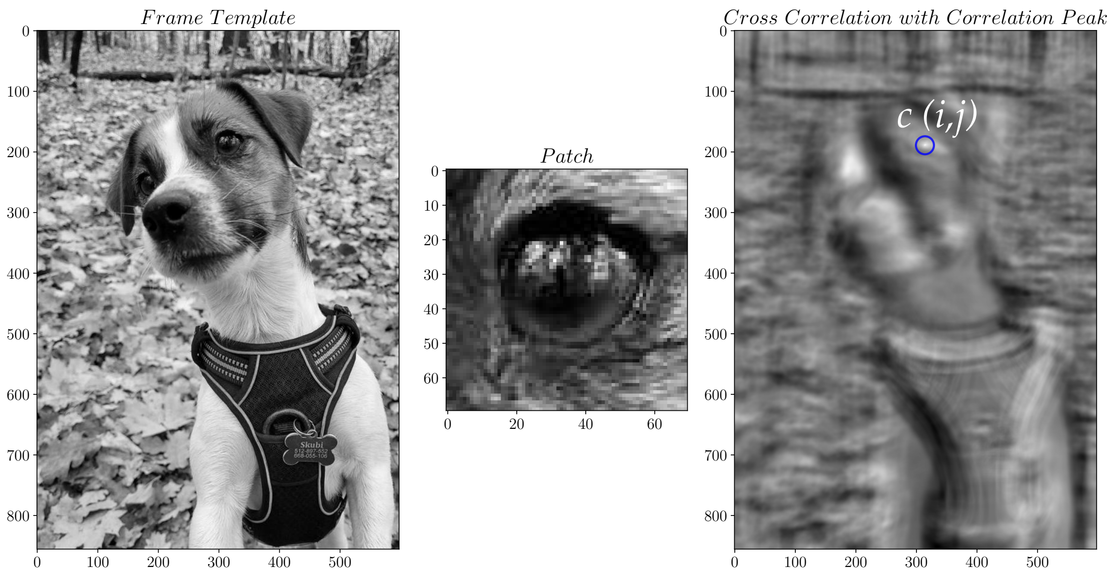

Figure 2.19: **Example of image matching** The search for the occurrences of the patch in the image can be understood a "sliding" the patch across the template and cross-correlating the patch with the "window" of the template of the same shape and size.

The choice of the summation stems from the assumption that the patch is a square image with 2h+1 pixels on their side. One can imagine the frame template and the

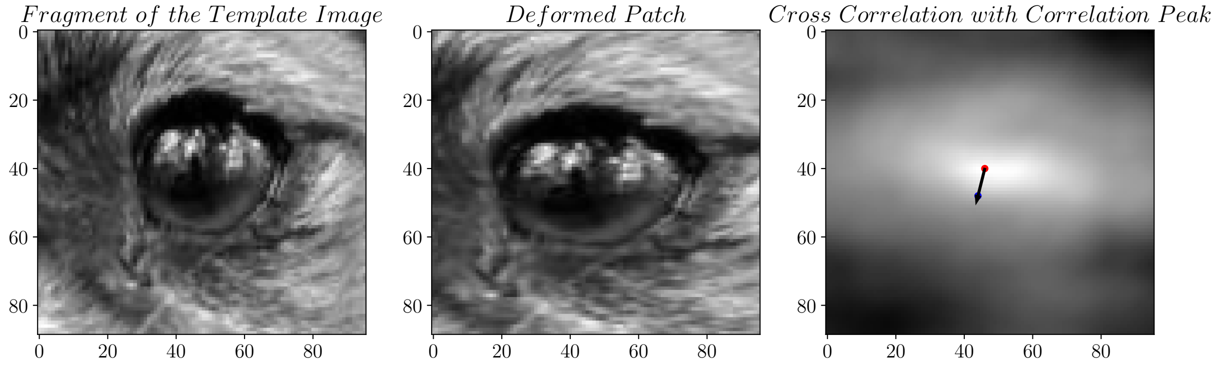

Figure 2.20: Highest cross correlation value for position (i, j) is obtained by displacing the deformed patch on the template patch by a certain displacement vector.

current frame being split into patches (Figure 2.20). Next, the computation of their the cross correlation value and position i, j of the maximum cross correlation peak can be performed. Finally, one can calculate the displacement vector allowing for best match of the current frame patch with the frame template patch. In that way, a motion field is being inferred that can be then applied to the original data frames.

2.7.5 Caiman framework step by step

The routine can be summarized in five steps:

(1) Determination of the dynamics of calcium indicator used in the study autoregressive (AR) model dynamics and noise power for each voxel.
(2) Initialization of A, $\mathbf{b}$, C, $\mathbf{f}$ using one of the initialization routines that CaImAn software includes.
(3)Application of constrained alternating matrix factorization to optimize in pairs A, $\mathbf{b}$ and C, $\mathbf{f}$.
(4) Merging and/or removal of existing components.
(5) Repetition of steps 3 and 4 until user defined conditions met.

All steps will be briefly explained in following sections.

2.7.5.1 AR process

Fluorescence measurement as reported by calcium indicators can be treated as a time series of somatic (in cell body) calcium concentration. A way to model such time series is by employing a class of autoregressive models which perform regression of the next term in the time series on a number of previous values of the same time series (p). Therefore calcium concentration over time $c(t)$ can be approximated as

$$c(t) = \sum_{k=1}^{p} \gamma_k \, c(t-k) + s(t) \tag{2.32}$$

were $s(t)$ is the number of spikes that a neuron fired at time point t. With a $p = 2$ process, both the decay (τ_d) and rise time (τ_r) of the calcium spike can be modelled in the form of :

$$\begin{cases} e^{-t/\tau_d} - e^{-t/\tau_r}, & \text{t} > 0 \\ 0, & \text{t} \leq 0 \end{cases} \tag{2.33}$$

In case sampling occurs at a slow rate or the dynamics of the used indicator is slow (our case), the events occur in the data instantaneously ($\tau_r = 0$) and then $p = 1$.

Observed fluorescence can be represented as:

$$y(t) = \alpha(c(t) + B(t)) + E(t),\ E(t) \sim \mathcal{N}(0, \sigma^2) \tag{2.34}$$

$y(t)$ is the fluorescence observed for each voxel, α is a nonnegative number that scales the spike amplitude and the noise $E(t)$ is assumed to be i.i.d. zero mean Gaussian[7] with variance σ^2. The noise term can be determined from the power spectral density of y [8]. As for the γ coefficients in 2.32, they are obtained by using the fact that the autocovarience of y has to satisfy a certain recursion. Further details regarding this and other methods employed for model parameters estimation can be found in [123] and its Supplemental Information accompanying.

2.7.5.2 ROI initialiazation routines

Greedy ROI initialization is used to obtain best guesses of for $A = [\mathbf{a_1}, .., \mathbf{a_K}]$, $C = [\mathbf{c_1}, .., \mathbf{c_K}]^T$ and **b**,**f**.
The name "greedy" stems from the problem-solving heuristic used by greedy algorithms which is to find an overall optimal solution to a problem by making at each step locally optimal choices. Greedy methods are suitable for solving problems for which a local optimal solution leads to finding a global solution.

In essence, the routine relies on locating possible neurons using spatial filtering methods [9]. Greedy ROI routine requires as inputs raw data ($Y \in \mathbb{R}^{dxT}$) which is then stored in a matrix R. Further, the user needs to specify the number of components K that should be initialized. In addition, a Gaussian kernel with standard deviation (τ_x, τ_y, τ_z) approximating the size of a cell body has to be defined along with the size of window corresponding roughly to twice the size of an average neuron (w_x, w_y, w_z). A Gaussian blur matrix $D \in \mathbb{R}^{dxd}$ is then constructed from such vectorized 2D Gaussian kernels centred in each i column at the corresponding pixel i. First, each pixel is centred around zero by subtracting its median. Next, neuron-like intensity sources are sough in the data. This is done by acting on the data with the Gaussian blurred matrix (D^T) (Figure 2.21). That way, the all voxels are probed for the possible presence of a neuron. Each identified component has a centre that is the voxel with the largest variance.

2.7.5.3 Constrained alternating matrix factorization

The process of refining the initialized A, C and **b**, **f** is done using the alternating matrix factorization: spatial components A, **b** are estimated given temporal compo-

[7] elements are Independent and identically distributed

[8] Power Spectral Density is a function of frequency that represents the distribution of signal frequency components

[9] in very broad terms, it is a group of methods which are used to alter the content of an image by removing certain spatial frequencies that make up the object of interest

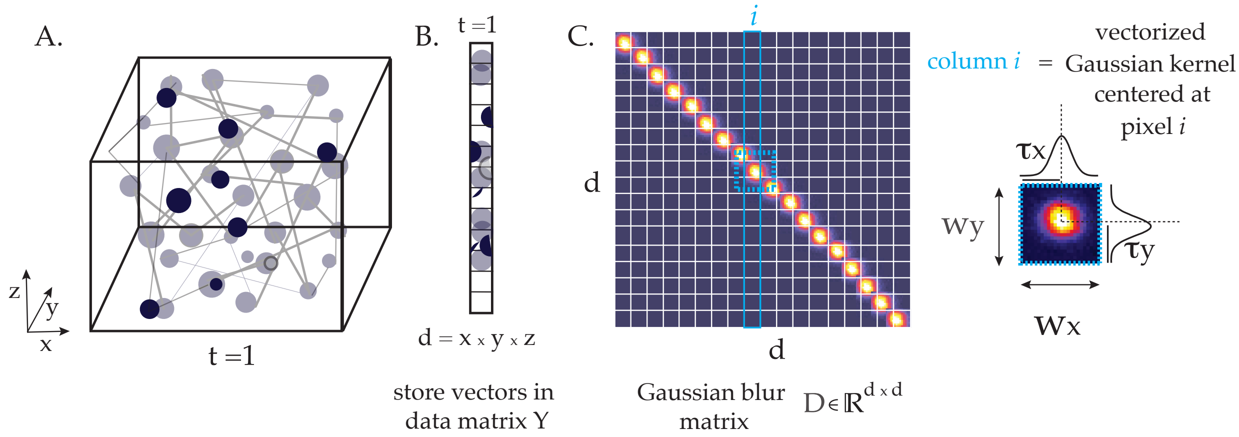

Figure 2.21: **Greedy ROI initialization A.** Neuronal network in a 3D FOV at each time step (here t = 1) can be B. linearlized to a d x 1 vector which then can be stored in a matrix form ($Y \in \mathbb{R}^{dxT}$). C. A Gaussian blur matrix $D \in \mathbb{R}^{dxd}$ is constructed from vectorized 2D Gaussian kernels centered in each i column at the corresponding i. That way, the all voxels are probed for the possible presence of a neuron. The kernel is contained in a window (w_x, w_y) with a has (τ_x, τ_y) initial point standard deviation.

nents C, $\mathbf{f}$ and the other way around. Next, C, $\mathbf{f}$ are updated using newly obtained A, $\mathbf{b}$.
Note that each column of A describes the location and shape of an active neuron in the FOV. By imposing a sparsity constraint on A shape compactness of the identified neurons is promoted. This is done by minimizing the l_1 norm[10] of A. With the knowledge of $C^{(k-1)}$ and $f^{(k-1)}$ from the previous iteration a new spatial matrix A^k and background $\mathbf{b}^k$ can be computed by solving a convex problem [11].

2.7.5.4 Merging ROIs accross planes

During initialization, a single neuron can be split into multiple components. To merge such neuron back into a single component a merging procedure needs to be implemented. CaImAn uses graph theory to identify such cases. Identified components are represented as nodes of a graph connected via edges if their spatial overlap exceeds a certain threshold. Next, a search for maximal cliques in such a graph is performed (Figure 2.22 A) [12]. A correlation matrix of the temporal components of nodes belonging to the maximal clique is then computed. Finally, a threshold for the correlation coefficient is set to find the largest principal sub-matrix[13] where all correlation coefficients exceed the threshold. In addition, at this step components might be removed if their spatial compactness and temporal behaviour does not satisfy the imposed requirements.

[10] sum of the absolute values of all matrix entries

[11] a real-valued function is convex, if one can draw a line segment between any two points on the graph of the function and finds that it is located above the part of the graph between the two points.

[12] a clique is defined as a subset of nodes of an undirected graph (order in which nodes in such graph are connected is not relevant) where every two distinct nodes are then adjacent

[13] a square matrix obtained by removing certain rows and columns of a given matrix

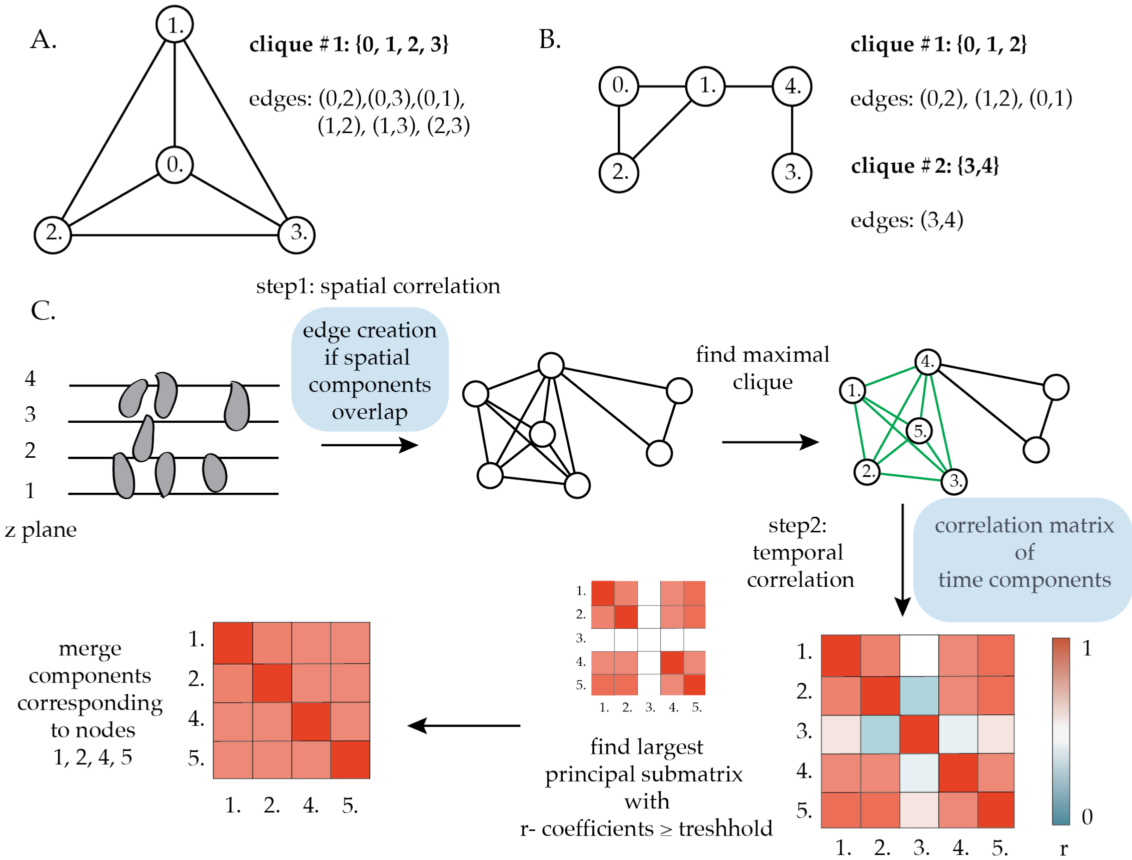

Figure 2.22: **Principle behind component merging** Examples of possible cliques are presented in A. and B. A four node graph where every node is connected with every other node via a unique edge forms a clique that is at the same time the maximal clique for this graph. On the other hand, in a five node graph in B. two cliques can be distinguished where clique #1 is the maximal clique for this graph. C. Multiple components across several z planes were identified. They are used to form a graph with edges occurring between nodes if the spatial overlap between the pair of components is above a set threshold. Next the maximal clique is searched for and a correlation matrix of the nodes which form this clique is computed. Finally, components forming the largest principal sub-matrix with correlation coefficient above a set threshold are merge together.

2.7.6 Quantify synchrony

What the C matrix stores is something like an encrypted conversation between neurons forming the network and its underlying synaptic architecture. One approach to try and decipher the code or at least get some insights regarding it, is to study how activity traces co-vary in time. This means to study synchrony between them. Two types of such synchrony can be distinguished: global synchrony and local synchrony.

2.7.6.1 What information do correlations provide?

Correlation studies can constitute the first step into studying the functional connectivity of a neural circuit and give a glimpse into how it works, if groups of neurons have common inputs or synaptic interactions. However, one has to be very careful as to making claims about insights that synchrony alone provides. For example, oscillations have been reported to arise naturally as a result of intrinsic properties of neurons[126].

2.7.6.2 Global synchrony

A "snapshot" image of global synchrony can be provided by standard correlation measures such a Pearson correlation coefficient.

$$\begin{aligned}
r_P &= \frac{cov(X,Y)}{\sigma_X \sigma_Y} \\
cov(X,Y) &= \frac{1}{n}\sum_{i=1}^{n}(x_i - \overline{x})(y_i - \overline{y}) \\
\sigma_X &= \sqrt{\frac{1}{n-1}\sum_{i=1}^{n}(x_i - \overline{x})^2} \\
\sigma_Y &= \sqrt{\frac{1}{n-1}\sum_{i=1}^{n}(y_i - \overline{y})^2}
\end{aligned} \tag{2.35}$$

where $\overline{x}$ and $\overline{y}$ are mean values of X and Y, n is the lenght of X and Y. In our case, X and Y are two fluorescence time traces $\mathbf{c}$. However, the activity signal amplitude of a neuron is influenced both by the type of neuron (biological reality of the sample) but also at its position in the FOV - close or far from the illumination site, deep or not in the imaged tissue (setup's hardware reality). Because of that, rather than studying the linear dependence between the raw traces monotonicity between rank traces can be measured. By mapping traces to the same rank range one can limit the impact that amplitude differences have on the correlation analysis. For that is suffices to replace X and Y with rank variables X_r and Y_r, σ_{X_r}, σ_{Y_r} and a new correlation coefficient - Spearman's rank correlation coefficient r_S can be computed.

$$r_S = \frac{cov(X_r, Y_r)}{\sigma_{X_r}\sigma_{Y_r}} \tag{2.36}$$

2.7.6.3 Local synchrony

The similarity between two time series can be measured using the time-lagged cross correlation that yields a shift - *lag* - for which the signals, when displaced by this shift one with respect to the other, have the largest similarity (correlation). In case the lag is not equal to zero, a leader-follower relationship between the signals can be suspected.

$$(f \star g)(\tau) \triangleq \int_{-\infty}^{+\infty} f^*(t) g(t+\tau) dt \tag{2.37}$$

where $f^*(t)$ is the complex conjugate of $f(t)$, τ is the lag, meaning that a feature that occurs at f at time t happens at g at time $t+\tau$.

2.7.7 Spike train interference for fluorescence traces

To gain deeper insights into the dynamics of the network interactions it is crucial to deconvolve the spike trains from the dynamics of the calcium indicator. It is not the broadness of the signal peaks that causes issues in further analysis, for example in time lagged cross correlation when directionality between signals is wished to be investigated. Figure 2.23 depicts a situation when action potentials are modelled as Delta Functions and much wider Gaussian peaks.

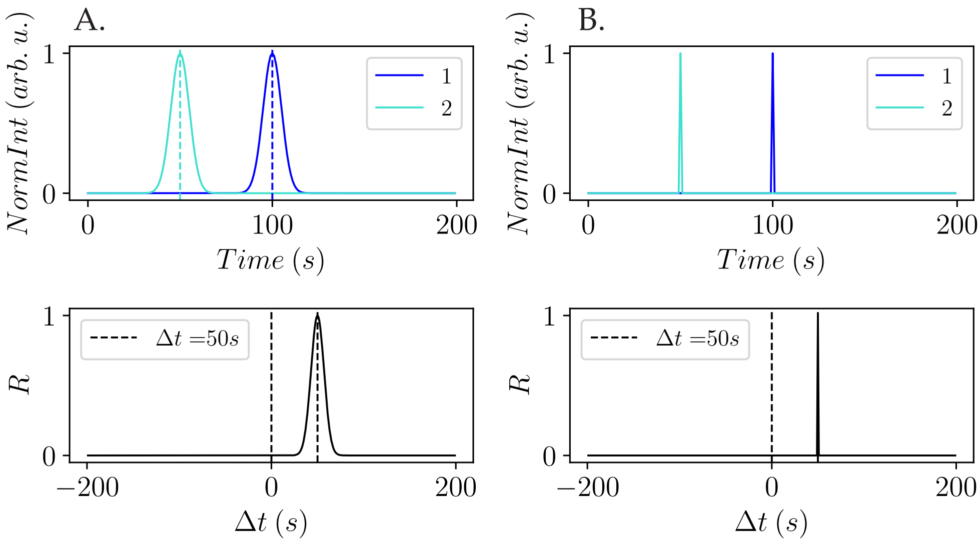

Figure 2.23: **Calcium activity vs. Spiking activity A.** Synthetic data where neuronal activity reported by calcium indicator is simulated by Gaussians and B. the deconvolved spiking activity is simulated by Delta functions. $\Delta\, t$ corresponds to the lag τ present in equation 2.37

Peaks from Figure 2.23 A. and B. could correspond respectively to events non-deconvolved and deconvolved from dynamics of calcium indicator. Still in both cases, the cross correlation operation shows the highest correlation of the two signals can be achieved with a lag of 50 s.
However, signals modelled in Figure 2.23 are noise-free. Therefore, a closer to reality situation is presented in Figure 2.24 where a hypothetical pair of neurons fires two action potentials each with the observational time.

The cross-correlation of the signals results in a clear triplet-like with peak ratios 1:2:1. This cross-correlation structure is lost when random noise is added to

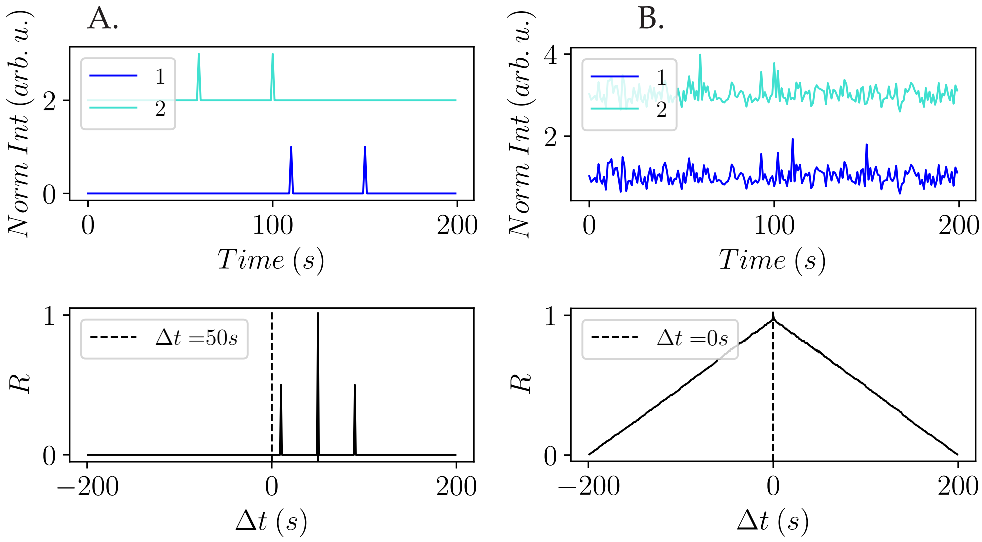

Figure 2.24: **Delta function-like spikes and noise** Synthetic traces generated for hypothetical a pair of neurons that fire two action potentials each at different times but with the same time interval. The cross-correlation of the signals results in a clear triplet-like with peak ratios 1:2:1. B. Random noise is added to the two signals from A. such that the action potentials are not easily distinguishable. The cross-correlation structure is degraded and no substantial information regrading the two inputs signals is obtained.

the two signals such that the action potentials are not easily distinguishable. The cross-correlation shape is degraded to the point where it doest not carry substantial information regrading the two inputs signals. The need for signal "cleaning", meaning going from Figure 2.24 B. to A. is now even more obvious.

2.8 Image Restoration

Light-sheet microscopy images obtained in setup with a with static beam suffer from a contrast loss away from the illumination site. In addition, a stripe artefact is observed that is a result of absorbing or scattering structures present in the illumination path. A variety of filtering tools exist that partially allow to mitigate these effects and maximize the information content. Few simple examples will be mentioned in the next section.

2.8.1 Stripe artifacts filtering

Different methods have been developed to address this issue that involve either optical or digital solutions (for a recent review see Ricci et al. [127]). Since stripes show some level of spatial regularity, a simple way to digitally to reduce the stripes and image quality is by removing characteristic frequencies components from the Fourier Transform of the original image and transforming the result back (Figure 2.25).

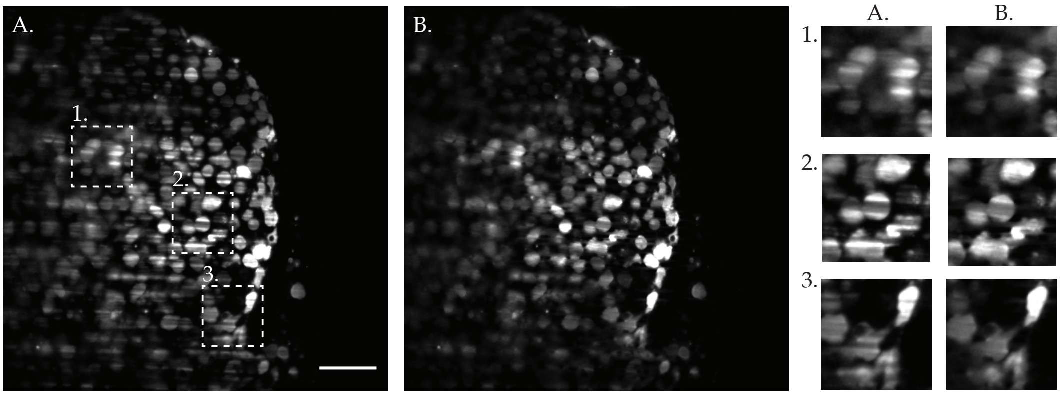

Figure 2.25: **Stripe filtering from the Fourier Transform of the original image A.** Original image with selected regions affected to different extent by the stripe artefact. B. Inverse Fourier Transformed image, in which frequencies contributions corresponding to the stripes have been removed. Right most panel depicts regions 1, 2 and 3 from A. and the corresponding regions in B. (scale bar: 100 μm)

2.8.2 Minimize blur and accentuate details

Unsharp Filter

For display purposes, one can use filters to accentuate details in shapes and decrease blur present in the image. An example of such filter is the Unsharp Filter. The procedure consists of creating a mask which can be next scaled by a weighing factor and added to the original image (Figure 2.26 C.)
In the first step the input image is Gaussian blurred to remove sharp edges. Next, it is multiplied by a factor $\geq 1.$ to produce a mask (Figure 2.26 B.) which can be added to the input image. For quantitative analysis, other types of filters are recommended. This is because image intensities are not preserved and the summation of the processed image includes only a fraction of the original image.

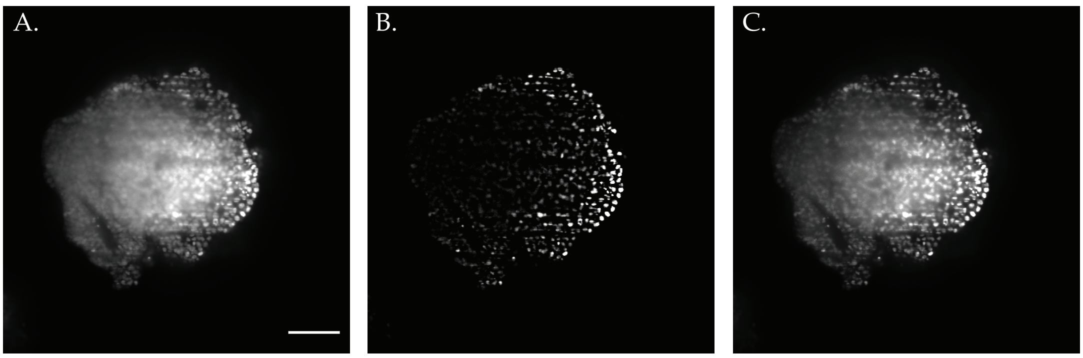

Figure 2.26: **Example of Unsharp masking an image A.** Original image is used to B. create a mask (in this case the mask is not scaled, weight = 1). which can then be C. added to the original image to yield the masked image. Scale bar: 100 μm

Top Hat Filter

One such group of filters are Morphological filters. As an example the Top Hat filter will be briefly presented. It consists of two operations: erosion followed by dilation (so called opening operation). In both cases, operations are performed by probing the input image with a matrix selected such that its shape and size match the structures one wishes to process in the input image. Such object is called the structuring element. First, the erosion is performed which will reduce shapes contained in the image, make them more visible and fill in small gaps they can contain. The structuring element is superimposed on top of the input image such that origin of the structuring element overlaps with the input pixel coordinates (red central pixel in the structuring element in Figure 2.27). The value of the inspected pixel is assigned a new value equal to the the minimum value among all pixels forming the neighbourhood of the origin of the structure element. In the next step, shapes

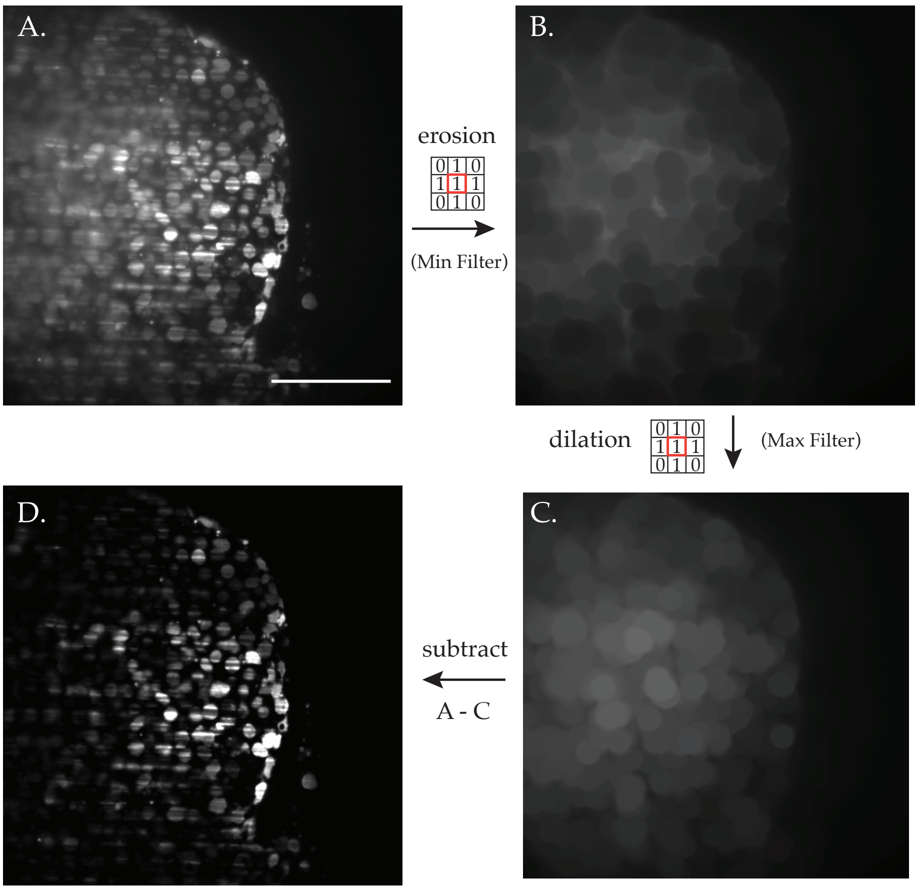

Figure 2.27: **Example of Top Hat transformed image** with a circle-shaped structuring element (not to scale) A. Original image B. is eroded with Min Filter C. which next undergoes dialtion (with a Max Filter) to yield a "grayscale opening". D. By subtracting (A.-C.) a Top Hat transformed image is obtained.Scale bar: 100 μm

are expanded back in the dilation operation. Here, the inspected pixel gets assigned the value among all pixels forming the neighbourhood of the origin of the structure element.

2.9 Image segmentation: how to make the computer see what our eyes see?

To facilitate the analysis and extraction of meaningful information from digital images, pixels forming these images can be partitioned into regions or objects based on some decided rules. This operation is referred to as image segmentation. In this thesis, an open source segmentation toolkit created in Heidelberg, Ilastik, has been used [128].

Pixel + Object Classifiction Workflow

Step 1: Pixel classification

Pixels are labelled based on:
- characteristics they display in terms of some particular features such as Color/Intensity, Edge, Texture which should be selected such that they allow for the desired discernment of pixels
- annotations provided by the user (a Random Forest classifier [14] is interactively trained by the user). For each class a probability map is generated and can be converted into individual objects.

Step 2: Object classification

Probability maps obtained in *Step 1* are threshold and pixels belonging to the same group (instance) connected to form separate regions (objects).
In this work, Ilastik Workflow (Pixel + Object Classifiction) was used to segment a nuclei structural data from light-sheet microscopy data. This is of particular interest when performing cell-type characterization of cells that build an organoid (based for example on their morphology as reported by fluoresecent markers).

[14]Random forest is a classification algorithm, which as the name suggests, allows for assignment of observations into defined groups (classes). It consists of multiple decision trees which behave as an ensemble. The data is sub-sampled and the class of each sample is predicted by a single decision trees. All predictions are collected and the class which was predicted the most times becomes the model's prediction for the dataset.

Chapter 3

Experimental Results

> "Whatever it is you're seeking won't come in the form you're expecting."
>
> — Haruki Murakami

This chapter is dedicated to the presentation of the experimental results obtained in the frame of this doctoral thesis. Results are divided into three sections. The first focuses on the characterization of the homebuilt light-sheet setup it terms of the design principles, achieved spatial resolution, beam control, laser lines and magnification of the used objectives. Next section is dedicated to the preparation and structural characterization of a sample that can be used to validate the system. Finally, functional imaging of the generated sample is performed and the obtained data analysed using the CaImAn-based pipeline described in the previous chapter.

3.1 Design goals of the setup

The advantage and at the same time, reason for home-built systems is that their design can be adjusted to the sample that is to be investigated. The requirements that the setup has to satisfy are:

- posses spatio-temporal resolution allowing to register neuronal signals propagating at millisecond timescales at a single cell level
- provide a readout in 3D with the use of calcium reporters commonly used in the field of neuroscience
- provide physiological conditions to the biological sample during functional measurements
- be characterized by a minimal complexity

The prototype of the microscope has been built before work within this thesis started. However, the set up has not yet been characterized in terms of spatial resolution. In addition, the initial set scanning mode did not allow for high-speed volumetric data acquisition (milliseconds). Finally, the mounting of the sample for imaging was not yet optimized. In the upcoming sections, I will address the implementation of advances to the prototype.

3.1.1 General concept

Functional volumetric imaging of a sample will be achieved using the scanning scheme no. 2 presented in 2.6.3, that is by precise high-speed movement of specimen with a piezostage along the axis perpendicular to a static Gaussian beam.

3.1.2 Beam geometry

The description of a Gaussian beam in section 2.6.1 assumed z as the direction of light propagation. However, for reasons that will be explained, the coordinate system will have to be rotated for further discussion as follows,

$$\begin{aligned} x &\rightarrow y \\ y &\rightarrow z \\ z &\rightarrow x \end{aligned} \tag{3.1}$$

The new direction of light propagation is therefore x. The reason for this choice of coordinates system stems from the design of the built setup. The system uses a Gaussian Beam to optically section the sample by collecting light emitted from single excited planes at a right angle with respect to the excitation. This is achieved by step-wise moving the sample along the axis perpenticular to the propgation of light-sheet with the use of a piezostage. It is natural to consider the xy axes as the lateral directions in the acquired 2D images and z as the axial direction along which the sample is moved. That means that the waist of the light-sheet will be defined as $w(x)$ and not $w(z)$ and same goes for the Rayleigh length which will turn to x_R from z_R (Figure 3.1).

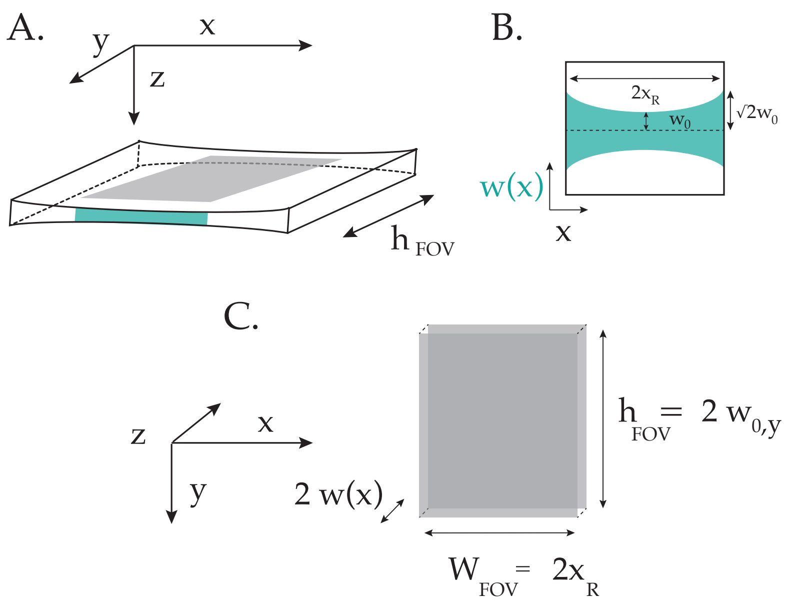

Figure 3.1: **Geometry of the used Gaussian light-sheet. A.** Beam orientation in the coordinate system with its thickness marked in turquoise B. which can described in as a function of $w(x)$, with resulting beam parameters w_0 (waist) and x_R (Rayleigh length). C. The beam, represented as the grey rectangle, with the height ($h_{FOV} = 2\, w_{0,y}$), total thickness ($2\, w(x) = 2\, w_0$) and width ($W_{FOV} = 2\, x_R$).

3.1.3 Choice of the light-sheet dimensions

Light-sheet characteristics need to be tuned so that relevant information about the specimen can be obtained. In the setup presented here, the goal was to create a system for neuronal structures imaging. That means, the light-sheet waist and Rayleigh length need to be such that:
• optical sectioning is below the size of an average neuron (average neuron soma is about 11 μm [66])
• the Rayleigh length is sufficient to capture multiple neurons in a single plane (multiples of a neuron soma).

The choice of the optics element used for shaping the beam has to allow for the fulfilment of these two requirements.

3.1.3.1 Field of view (FOV) consideration

The lateral field of view achievable with the use of a 20x objective and a camera (ORCA-Flash4.0 V3 Digital CMOS) with a pixel array of 2048 x 2048 and a pixel size of 6.5 μm is:

$$FOV \;=\; \frac{6.5}{20}\;(2048\,\mathrm{x}\,2048)\;=665.5\,\mathrm{x}\,665.5\;[\mu m^2] \tag{3.2}$$

To reliably sample neuron cells, with an assumed diameter of $\approx$ 11 μm [66], the setup needs to offer sectioning capability of around 5 μm.
According to 2.20, a light-sheet offering approximately such waist could be obtained assuming $\lambda = 0.5$ μm and an illumination aperture of about $NA_{ill} = 0.09$ (Figure 3.2).The resulting waist is $w_0 = 3.5\mu m$ and the Rayleigh length reaches > 50 μm when the waist increases to $\sqrt{2}w_0 \approx 5\mu m$. The optical section within $2x_R = 51\mu m$ (h_{FOV}) covers $\approx$ 5 neurons in width and is $< 5\mu m$ thin.

3.1.4 Beam path

To expand the colour palette of fluorescent dyes that could be imaged in a future sample, the setup was equipped with three laser lines : 488 nm, 561 nm, 643 nm. Each laser was coupled into an optical fibre which has a diameter large enough to enable propagation of more than one light-mode. The output intensity of the lasers is controlled with a crystal-based device, a Polychromatic Acousto-Optic Modulator (PCAOM). To provide physiological conditions (temperature and CO_2) during live imaging experiments, an incubation chamber made out of Plexi glass has been designed and realized by Nicoleta Dahnovici in the frame of her Bachelor Thesis (Figure 3.3 A).

The light-sheet module can be assembled using a cage system (Thorlabs) and integrated in a standard inverted microscope where it replaces the microscope's condenser and fluorescence filter (Figure 3.3 A and B).

3.1.5 Laser beams alignment and characterization

For a better control over the coupling efficiency of the laser beam to the optic fibre, a pair of mirrors is integrated into the setup. Their role can be better illustrated by

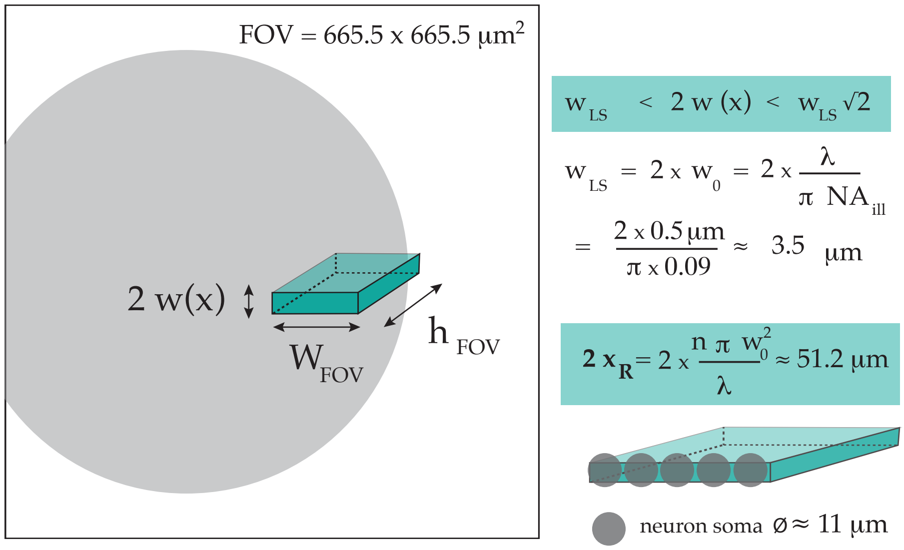

Figure 3.2: **Field of view vs. light-sheet dimensions.** Sample (grey circle) in the camera field of view (for a 20x objective), illuminated by the light-sheet beam (green rectangle). For the calculation illumination wavelength was assumed $\lambda = 0.5$, $NA_{ill} = 0.09$ and a neuron cell of an average diameter of 11 μm [66].

drawing the components from Figure 3.3 D in a straight line while maintaining the distances between them (Figure 3.4). For simplicity, only x-axis will be considered but the same is true for the y-axis. The closer mirror M1 serves as the position mirror of the setup and M2 as the angle mirror. Correction of the misalignment of the beam along PCAOM is done with M1 as it displaces the beam from the desired position at a larger distance than M2 for the same angle α (X1>X2). The offset of the beam along the optical coupler can be reduced with M2 as it can displace the beam from the optical coupler more than from the PCAOM (X2'>X2). By iteratively adjusting the knobs on both mirrors in a consistent and systematic manner, the beam is optimally reflected and translated throught the PCAOM and optic coupler. This aligning procedure is called "walking the beam".
The best indication of the beam optimal coupling to the fiber is the readout of maximum power at the exit of the fibre. Quantification of power is done with the use of a power meter (PM100A, Thorlabs). For the measurements, the light-sheet module is unmounted and instead the power sensor is fixed (Figure 3.5 A).
Walking the beam procedure is performed for each individual laser line until no higher power values can be obtained. Maximum power outputs are presented in Figure 3.5 C.

3.1.6 Beam shaping

As mentioned before, the setup's illumination aperture defines the light-sheet beam thickness and its divergence. The higher the illumination aperture, the thinner the achievable thickness of the light-sheet, however the faster the beam's divergence and therefore the smaller the usable FOV. To allow for optimal sectioning of the cellular structures and maximally use the field of view our detection objectives could grant (333 x 333 μm^2 (40x/0.8 W) and 665 x 665 μm^2 (20x/0.5 W) a light-sheet of a few microns was designed.

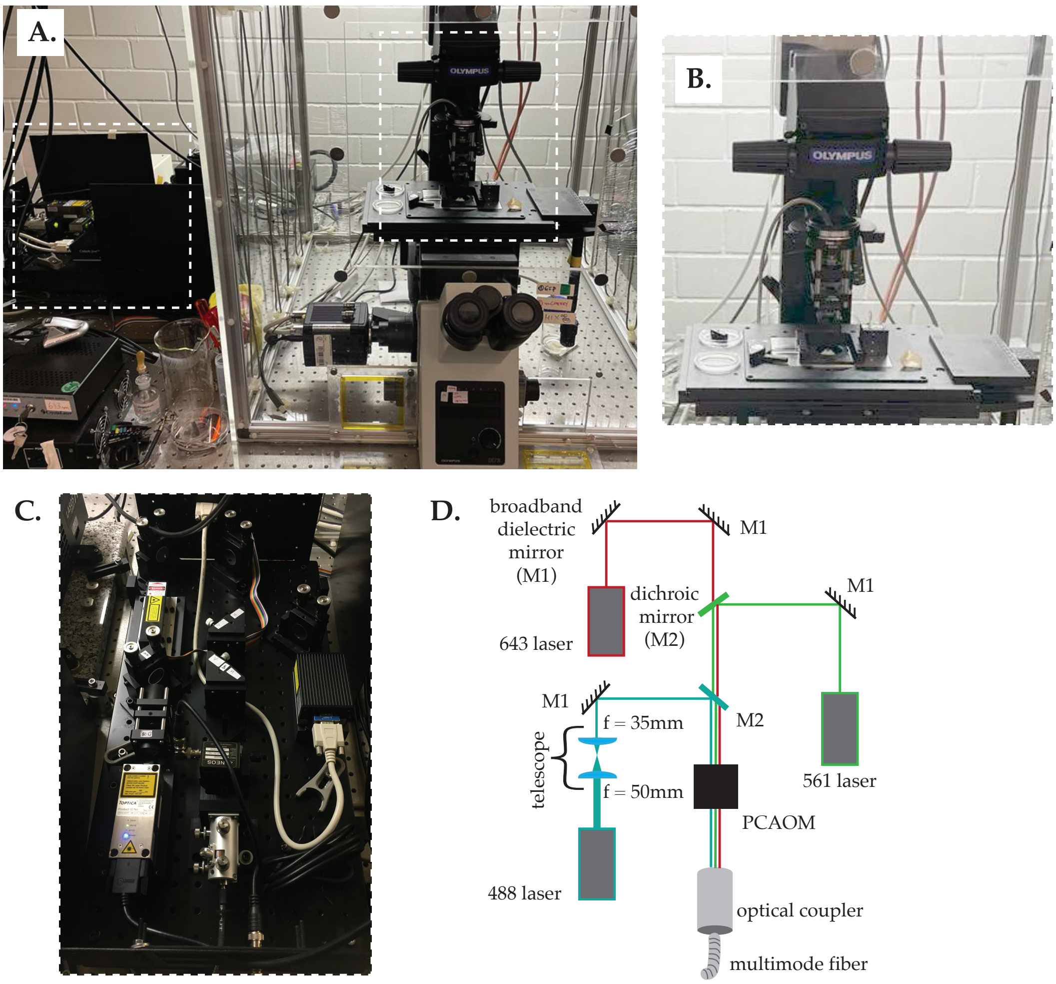

Figure 3.3: **Setup architecture A.** The body of the system consists of a standard inverted microscope with B. a light-sheet module integrated in the place of the condenser and fluorescence filter and C. a laser combiner box. D. The optical beam path of the three fibre-coupled laser. For display purposes only the beams are drawn parallel to each other when passing through the Polychromatic Acousto-Optic Modulator (PCAOM) and optical coupler

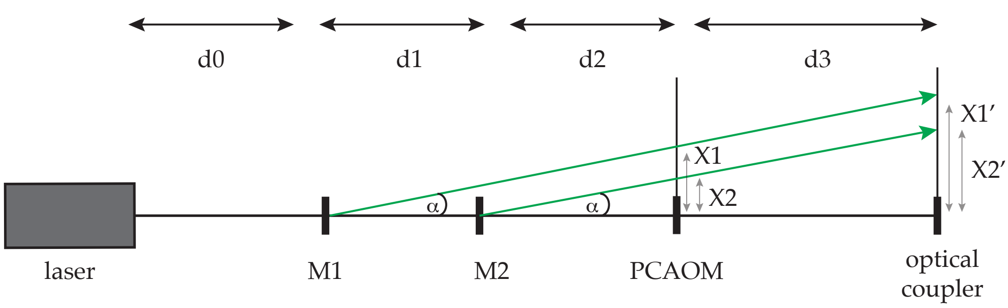

Figure 3.4: **Beam alignment** using the “walking the beam” method illustrated by drawing optics elements in a line while preserving the original distances (d0, d1, d2, d3). To eliminate offset through the PCAOM and the optic coupler, the beam is reflected and translated in the optical path using M1 and M2 that serve as position and angle mirrors respectively.

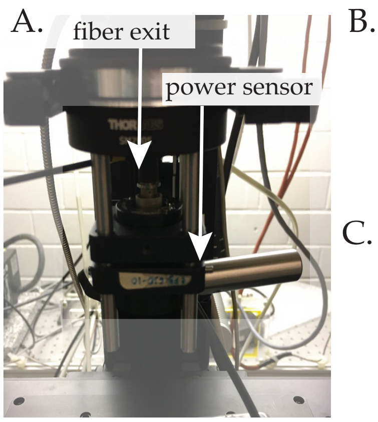

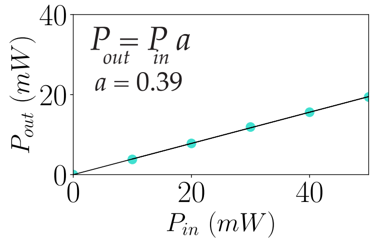

C.

λ (nm)	P_{max}(mW)
488	78.0
561	26.3
643	8.6

Figure 3.5: **Maximum Output Power Determination A.** Power meter sensor head has been mounted in the place of the light-sheet module. B. Calibration curve for the 488 nm laser C. Maximum output powers for all three laser lines.

A Light-sheet was created with the use of a cylindrical lens in conjunction with an aspherical lens (Figure 3.7). Upon exiting the optic fibre, the beam is collimated with a kinematic collimator mounting adaptor (with a focal length f_1), "flattened" by a cylindrical lens (f_2) and focused by an aspherical lens in the medium where the sample is located. The light-sheet is created f_3 away from the lens which is larger for media with higher refractive index ($n_{air} < n_{water}$).

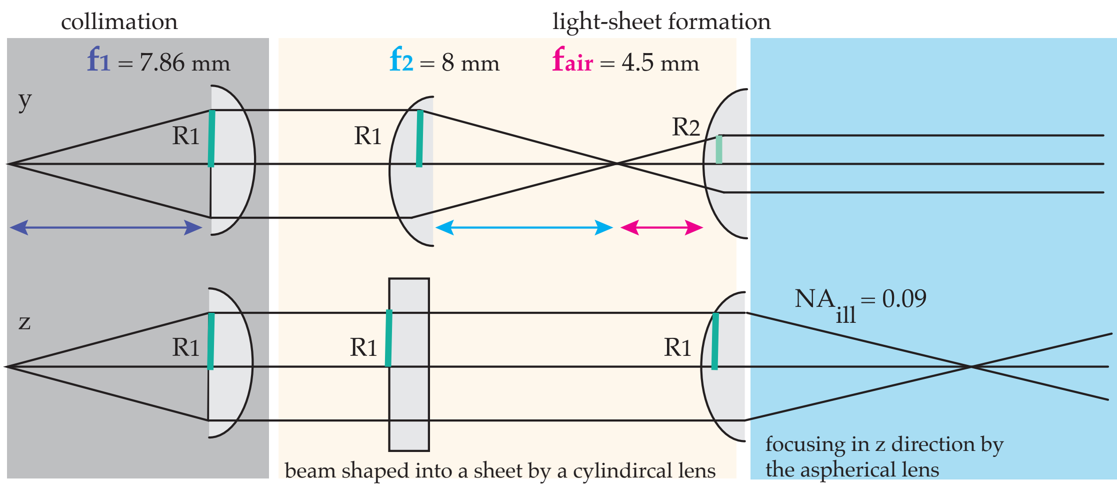

Figure 3.6: **Illumination aperture consideration** The two axes of the light-sheet are shown along which the beam is ultimately focused (z) and collimated (y) in the sample. Upon exiting the optic fibre, the beam is collimated with a kinematic collimator mounting adaptor with an focal length f_1 (at this point beam diameter is equal to R_1). Next, it reaches a cylindrical lens where it gets "flattened" at f_2. Finally, it is focused by an aspherical lens (beam radius R_2) in the medium were the sample is located. Because $n_{air} < n_{water}$ the focal length of the lens (4.5 mm) is elongated and yields and illumination aperture of 0.09.

To calculate the illumination aperture, the radius R_1 and back focal length of the aspherical lens in water (f_{water}) need to be known. The numerical aperture at the exit of the fibre is equal to $NA_{fibre} = 0.11$. Therefore, the radius of the beam hitting the collimating lens is NA_{fibre} x $R_1 = 0.865$ mm ≈ 0.9 mm .

As a next step, the lens maker's equation is used

$$\frac{1}{f_{water}} = (n_{lens} - n_{water})(\frac{1}{R_1} - \frac{1}{R_2}) \tag{3.3}$$

From the lens specification data sheet (Amstechnologies) the radii of the lens are $R_1 = 2.63$ and $R_2 = \infty$, refractive index of the lens $n_{lens} = 1.59$ (D-ZK3 Glass) and therefore $f_{water} \approx 10mm$.
One can notice that when plugging n_{air} in the place of n_{water}, the focal length that is obtained is equal to 4.45 mm which is close to the focal length stated in the specification sheet of the lens for air (4.5 mm).
The half opening angle of the illumination in water can be therefore calculated as $\alpha = \arctan \frac{0.865}{10.1}$ which then yields, after being plugged into:

$$NA = \sin \alpha \tag{3.4}$$

a numerical aperture of $NA \approx 0.09$. Note, here α was obtained for the water medium with n_{water}. Therefore equation 3.4 is modified with respect to the standard form $NA = n \sin \alpha$.
Using equation 2.21 the theoretical waist for the three laser lines can be calculated. The values are presented in Figure 3.10 D.

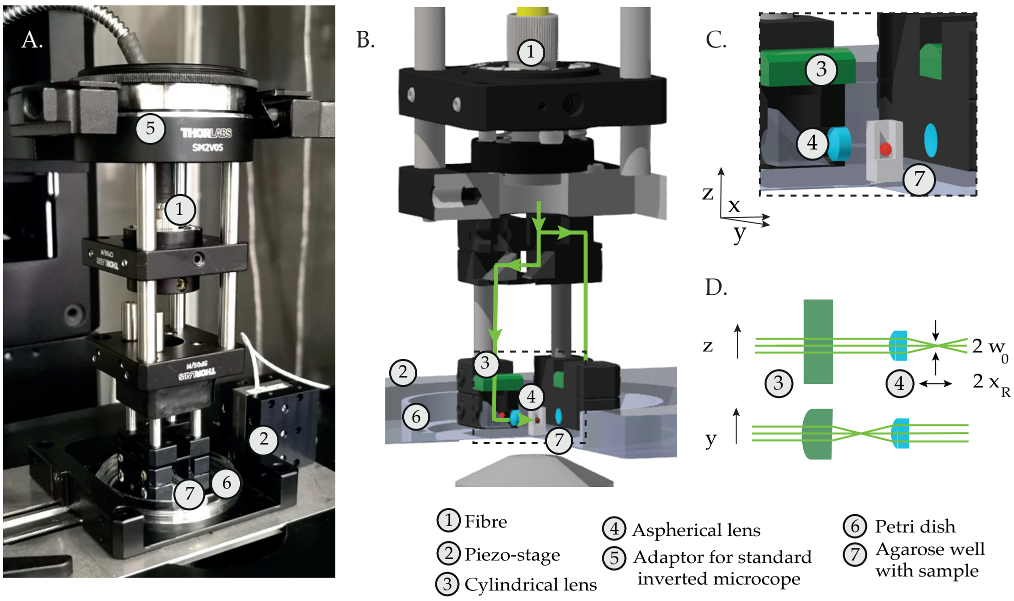

Figure 3.7: **Design and realisation of a light-sheet module A.** The light-sheet module was implemented as an add-on to a standard inverted microscope where it replaces the microscope's condenser. Fast volumetric imaging of the specimen is achieved by a stepwise axial movement of the sample along the optical axis using a custom ordered piezo-stage B. Upon exiting the fibre, the beam is split on a beam splitter and is further folded by a mirror and right-angle prisms. C. Zoom in: a static planar light-sheet is created by combining a horizontally oriented cylindrical lens (green) and an aspherical lens(cyan). The light-sheet propagates in the sample along the x-axis of the assumed coordinate system as a Gaussian beam. D. characterised by a waist of $2w_0$ and a Rayleigh length equal to $2x_R$.

3.1.6.1 Determination of the objectives' magnification

Objectives' magnification has been characterized by imaging calibration slides (Figure 3.8 A and C). Intensity profiles for multiple ticks were extracted in Fiji (line tool) and multiple peak functions were fitted to localize the maxima positions and average the distances between them, which could be compared with the expected distance. As can be seen in table in Figure 3.8 B and D, the discrepancies lie below 0.5%.

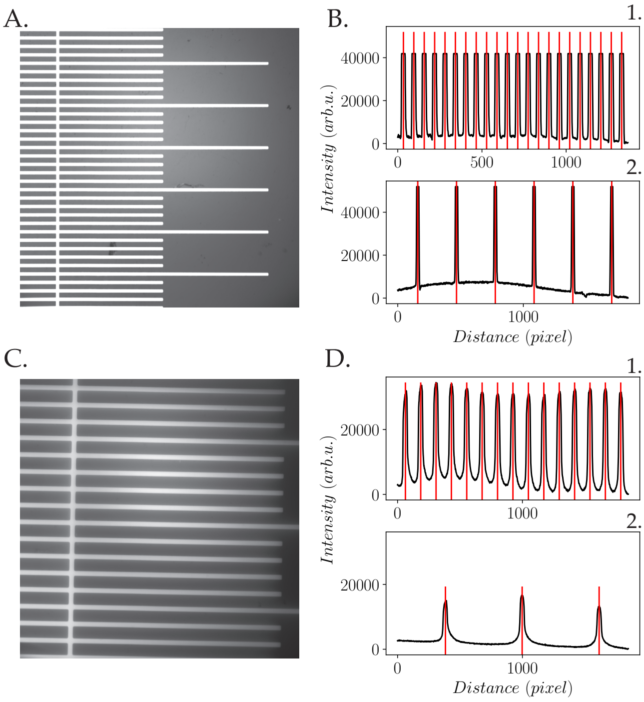

objective \ tick	measured (pixels)	calculated (pixels)
20x \ 100 µm	308.9	307.7
20x \ 20 µm	61.7	61.5

objective \ tick	measured (pixels)	calculated (pixels)
40x \ 100 µm	615.5	615.4
40x \ 20 µm	123.2	123.1

Figure 3.8: **Objectives' magnification** Bright field images of a glass ruler using A. 20x/0.5 W Olympus and C. 40x/0.8 W Olympus. Corresponding intensity profiles extracted from bright field images acquired with B. 20x and D. 40x.

3.1.6.2 Light-sheet beam characterization

To characterise the light-sheet beam parameters as well as its evolution in the FOV an alignment tool has been fabricated. It consisted of a 45° tilted mirror glued into a non-reflective custom-cute plate (Figure 3.9).
The illumination profiles of the light-sheet across the entire FOV was mapped using the tool that was moved along the optical axis with the piezostage and at each z-step deflected the light-sheet directly into the detection lens. Obtained illumination profiles were Gaussian fitted with a custom-written python script (Supplement 6.1) to extract the beam's thickness (Figure 3.10). The evolution of the beam is traced by plotting the $2\sigma_x$ as a function of axial position and fitting the data with a hyperbolic relation to extract the waist (w_0) and Rayleigh length (x_R) for three laser lines.

Thickness of the three light-sheets are higher for a factor of $\approx$ 1.3-1.5 than the expected values calculated for each laser line using equations 2.21 and 2.22 (Figure 3.10 D.). As for the Rayleigh lengths, obtained values are about a factor of $\approx$

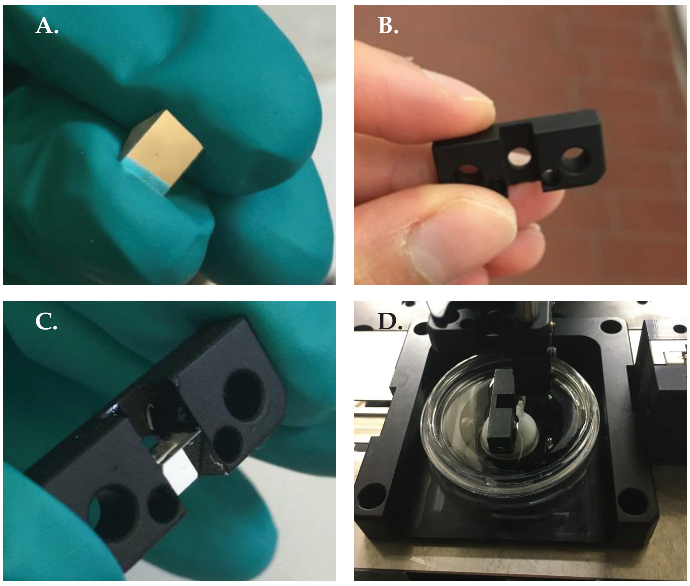

Figure 3.9: **Light-sheet alignement tool A.** mirror is glued into a B. custom-cut plate to produce a C. tool which could then be fixed to a glass-bottom Petri dish and used to directly reflect the light-sheet into the detection objective at different positions in the FOV.

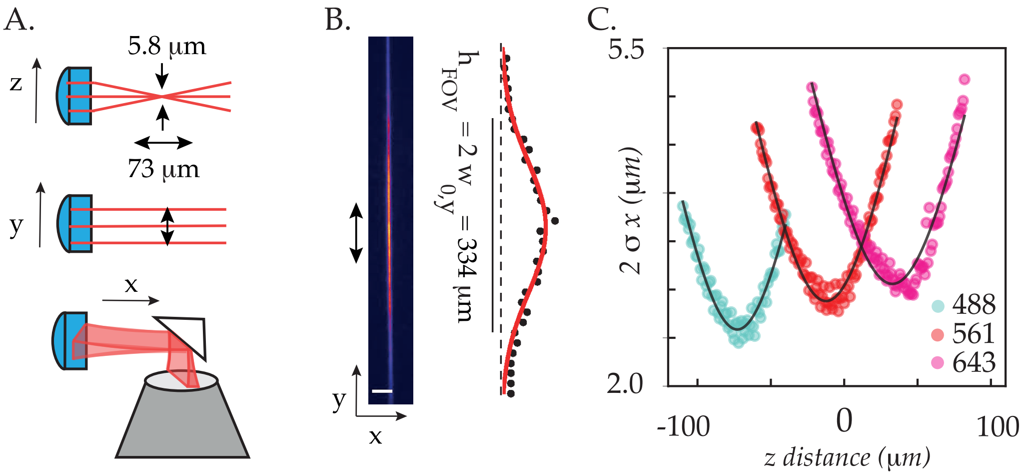

D.

λ [nm]	exp 2 w_0(μm)	exp 2 x_R(μm)	theo 2 w_0(μm)	theo 2 x_R(μm)
488	5.2 ± 0.1	65 ± 1	3.5	44
561	5.8 ± 0.1	73 ± 1	4.0	59
643	6.1 ± 0.1	81 ± 1	4.6	77

Figure 3.10: **Light-sheet beam characterization A.** Schematic representation of the light-sheet focusing in the FOV by the aspheric lens along with light-sheet parameters obtained by mapping the beam across the FOV with the use of the alignment tool (lower A.) B. Light-sheet profile acquired in the middle of the FOV with a Gaussian fit along the y-axis to determine its height $2w_{0,y}$. C. Evolution Rayleigh length in the FOV given by $2\,w_x(z)$. Data was fitted with 2.20 (black lines). Obtained fit parameters along with theoretical values calculated using 2.21 and 2.22 are presented in D. Overall, the light intensity distribution within the light-sheet is well-described by a Gaussian beam. Discrepancies between experimentally measured and theoretically predicted values arise probably from aberrations present in the physical setup. Scale bar: 25 μm (B.)

1.1-1.5 higher than the theoretical values. Generated light-sheet beams are close to being diffraction limited and their propagation can be described using Gaussian beam theory. The discrepancy in experimental values is most probably the result of spherical aberration being present in the setup.

3.1.6.3 Characterization of the setup's PSF

To characterize the 3D resolution of the setup, its point spread function (discussed in section 2.6.2) was measured by imaging agarose gel embedded beads (orange 540/560 nm beads, PS-Speck™) (Figure 3.11 A.)

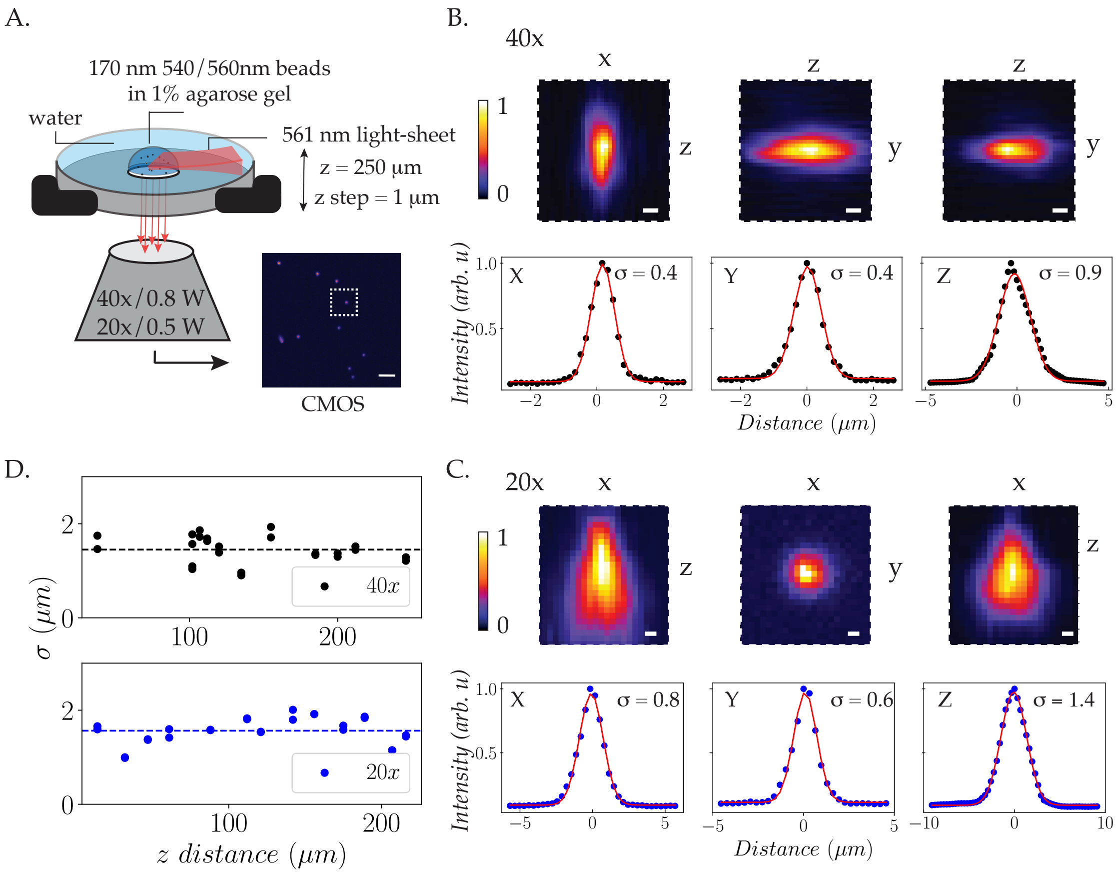

Figure 3.11: **Characterisation of the setup's resolution A.** Sub-diffraction sized fluoresencent beads (⌀ = 170nm, orange 540/560 nm beads, PS-Speck™) are embedded in 1% agarose gel (in ddH_2O) and imaged 250 μm deep into the sample with the use of a 20x and 40x objective (20x/0.5 W Olympus, 40x/0.8 W Olympus) with a z-step of 1 μm. Information on single beads can be retrieved from images created on a CMOS camera chip (dashed region). B. Exemplary lateral and axial intensity profiles along each of the two the perpendicular axes in three central planes (xy, xz, yz) for single beads acquired with 40x and C. 20x objective. D. Axial resolution defined given by σ of the profiles obtained from the beads as a function of z-depth. The dashed line corresponds to the mean value of σ. (Scale bar: 10 μm (A), 1 μm (B and C))

Procedure

For each bead, 4 lateral and 2 axial intensity profiles along each of the two perpendicular axis in three central planes (xy, xz, yz) were measured, normalized and

Table 3.1: Mean values of σ for multiple beads along with standard deviation for 561 nm laser.

Obj	σ_x (μm)	σ_y (μm)	σ_z (μm)
20x	0.8 $\pm$ 0.2	1.0$\pm$ 0.2	1.7$\pm$ 0.2
40x	0.5 $\pm$ 0.1	0.4$\pm$ 0.1	1.1$\pm$ 0.3

Table 3.2: Theoretical values of σ calculated using equations 2.25 and 2.26. Values of λ and α assumed for calculations: 488 nm: $\lambda_{ill} = 0.488$, $\lambda_{det} = 0.507$, 561 nm: $\lambda_{ill} = 0.561$, $\lambda_{det} = 0.58$, 643 nm: $\lambda_{ill} = 0.643$, $\lambda_{det} = 0.662$, $\alpha_{det} = 0.39$ rad (20x), 0.65 rad (40x).

Obj	σ_{488nm} (μm)	σ_{561nm} (μm)	σ_{643nm} (μm)
20x σ_{xy}	0.6	0.7	0.8
20 σ_z	1.7	2.0	2.3
40x σ_{xy}	0.4	0.4	0.5
40x σ_z	1.3	1.5	1.7

fitted with a Gaussian.The σ was then taken as the resolution. Representative profiles along the x, y and z axis for both objectives are depicted on (Figure 3.11 B. and C.) Finally, axial resolution for various depth in the FOV has been has been plotted and reads 1.5 $\pm$ 0.3 μm for 40x objective and 1.6 $\pm$ 0.3 μm for 20x objective (Figure 3.11 D.). Individual bead profiles were Gaussian fitted. The resulting fit error ($10^{-5} - 10^{-4}\mu m$, Supplement Figure 6.1) was negligible compared to the systematic error present in the measurements and was therefore not taken into account for further calculations. Mean σ values obtained from these profiles and the resulting standard deviations are listed in Table 3.1.

Since beads were imaged with the 561 nm laser, best comparison between predicted and experimentally measured resolution values can be made by comparing values obtained for this wavelenghts. They are blue (20x objective) and red (40x objective) coloured in Table 3.2 and correspondingly in Table 3.1 (here resolution along x and y axes are separated).

Sigma values obtained in Table 3.1 were used to simulate X,Y,Z Gaussian profiles with zero mean and the error taken as the standard deviation from corresponding Table 3.1 (Supplement Figure 6.2).

Since values obtained experimentally fall within one or two σ away from the theoretically predicted values, a good control over the setup is proven.

3.1.7 Volumetric scanning using a piezo stage

Volumetric scanning is realized with the use of a piezo stage, the control over which takes place via a Step-Direction Control System (SDC2) that comes with the product. SDC2 is integrated into the electronic architecture of the setup to receive step and direction as inputs. Each z-step is then accomplished using a closed-loop control system. [1]

3.1.7.1 Bidirectional scanning mode

Higher sampling rates can be achieved by implementing a bidirectional image acquisition scheme. Images are acquired as the stage moves both up and down and sets of forward and reverse volumetric stacks are collected. That way, the dead time caused by the stage flyback to its starting position is eliminated. This mode has been implemented in the setup and allowed to increase achievable scanning speeds. It must be noted, that in this scanning scheme all planes are sampled at a different rate, with only the central plane being scanned at the overall scanning rate. This issue has not been addressed in this thesis however, in the literature, examples of how to at least partially mitigate this problem can be found. Greer and Holy interpolated consecutive pairs of stacks in time, which resulted in stacks with a constant virtual sampling time [43].

3.1.8 Hardware control of the microscope

The setup was controlled with MicroManager 2.0 Gamma [2] application. To attain high acquisition speeds, the camera was set to streaming mode and made into the setup's master, meaning that, its clock was driving the entire system's synchronization (Figure 3.12).

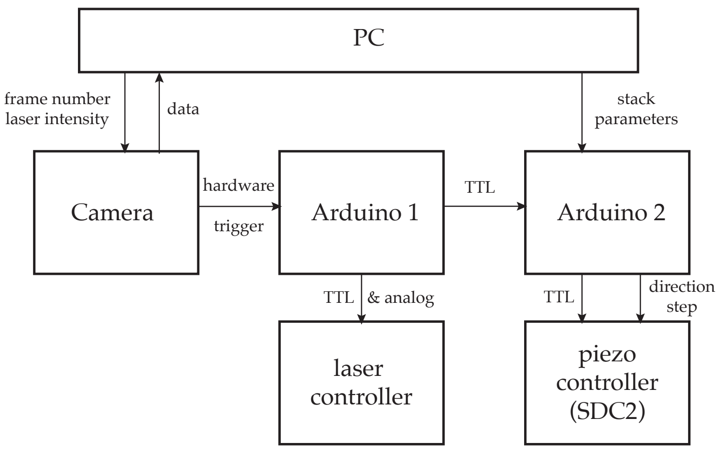

Figure 3.12: **Control of the light sheet.** The camera and controller of the PCAOM (Arduino 1) are loaded in the hardware configuration of MicroManager and can be controlled from the graphic user interface (PC). Arduino 2 is controlled using the serial Monitor (PC) and provides step commands and direction to the controller of the piezo-positioner (SDC2)

To start Multi-dimensional acquisition (MDA), parameters such as number of frames, exposure time and laser power intensity have to be set in the tab of MicroManager. The direction and number of z-planes are defined in the Serial Monitor of Arduino

[1] Two types of control systems can be distinguished. In an *open-loop system* (feedforward control), no information about the output signal is "fed back" to the system to establish if the output has reached the process "set point". The action of the controller is independent of the "process output". In a *closed loop system* (feedback control), some portion of the output signal is returned 'back' to the input and is part of the system excitation.

[2] MicroManager 2.0 Gamma

2. MicroManager translates all parameters into a sequence of states for each device. The control over the setup is then handed to the Camera. The setup's master pulls all other devices through their sequence of states by hardware-triggering them i.e. issuing transistor-transistor logic (TTL) signals at each exposure. Exposure time is set to 10 ms per frame, z-step (3 μm) takes about 150 μs, assuming a positioner speed of 20 mm/s.

3.2 Quest to grow a fluorescent sample

Now that the setup has been confirmed to have a spatio-temporal resolution allowing to image activity of individual neurons, a real sample is needed to validate the setup's capabilities.

3.2.1 Easily accessible *in vitro* generated neural network

Generation of 3D structures mimicking part of the CNS - cerebral organoids - from induced pluripotent cell or stem cells has granted access to nervous tissue that has so far been rather limited [3, 129]. If one decides for the creation of a mouse sample as opposed to a human one, time needed for growth can be up to 10-fold reduced. For that reason, the choice was made to follow published protocols [72, 73] for the culture of mouse retinal organoid (retina is considered part CNS) which is 24 days long.

3.2.2 Growth of 3D neuron cultures

First, a mouse embryonic cell line (mESC) [3]was obtained. The cells express two fluorescent proteins - a Histone-GFP fusion protein (green fluorescent localized in the nucleus) and a red-fluorescence calcium sensor R-GECO1. The absorption and fluorescence properties of these two biomolecules are presented in Figure 3.13.

3.2.2.1 step 1: pluripotency check-up

For the cells to be able to assume neuronal differentiation path, they need to start of as pluripotent cells. The presence of four commonly used mouse embryonic stem cell pluripotent markers: Oct4, Sox2, SSEA1, Nanog (Figure 3.13) [130, 131, 132, 133, 134].

3.2.2.2 step 2: induction of cell differentiation

The control over self-organizing systems such as organoids is very difficult as they are sensitive to changes in the initial conditions, such as medium composition, cell number and passage number, coating of the plates used for the culture. In addition intrinsic cell line properties influence its ability to self-organize. Upon many trials and some modifications in the initial protocols, a sample was created, however its growth was limited to 2 weeks not 24 days as reported in the literature (for a possible explanation see 3.2.3).

[3]kind gift from Bendzhov lab MPI for Molecular Biomedicine, Münster, Germany

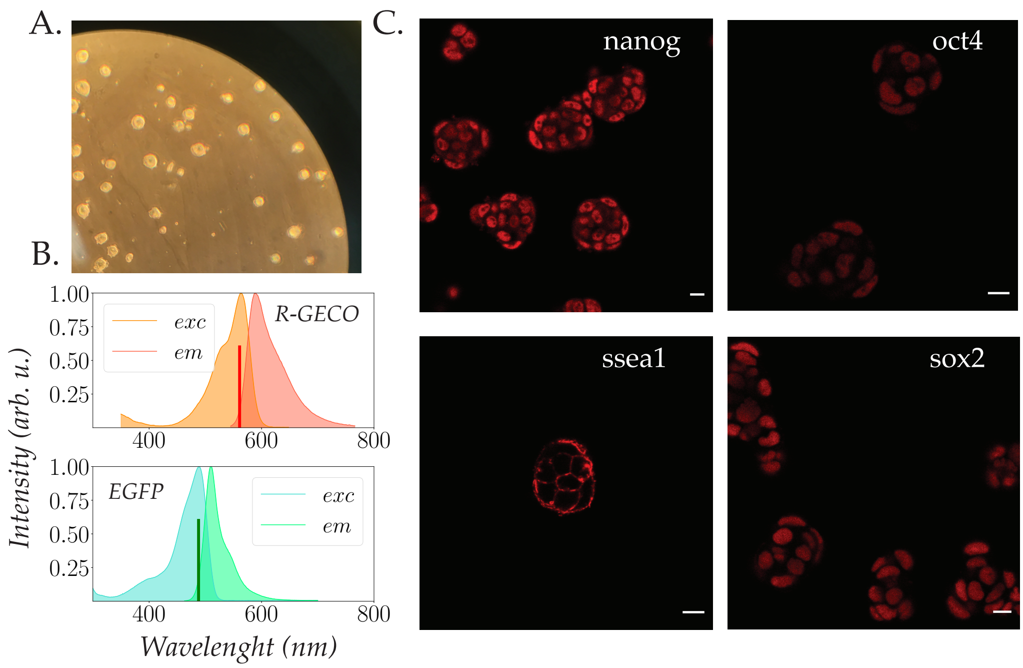

Figure 3.13: **Characterization of mESC R-GECOH2B. A.** Cells are cultured in gelatine coated flask and grow in compact semi-spherical colonies. B. They have been genetically modified to produce a histone H2B-GFP fusion protein and a red fluorescence Ca^{2+} sensor R-GECO1. Their absorption and emission spectra are displayed (data from: FPbase). C.Pluripotent status of the cells has been confirmed by immunostaining for markers (Nanog, Oct4, SSEA1, SOX2). This means mESC R-GECOH2B are capable of developing into neuronal cells.

In short the established protocol involved:

• formation of initial spheroids (embryoid bodies) via the aggregation of a predefined initial number of mESCs cells in ultra-low attachment U-bottom well plates[4].

• triggering of neural differentiation for 7 days via the addition of Matrigel and differentiation medium under physiological conditions (5% CO_2, 37°C)

• at day 7, U-bottom wells are filled-up with appropriate medium and the sample is transfered to 40% O_2, 5% CO_2 and 37°C conditions to optimize differentiation into specific neuron subtypes [73].
• at day 10, di- or tri-sectioning under a stereomicroscope (Nikon, Stereoscope) is performed, the medium is changed and the sample is transferred back into 40% O_2, 5% CO_2 and 37°C conditions

• by day 15 the culture is stopped

One of the key differences between published protocols and the one used here, was that the sample was kept longer in U-bottom wells (until day 10). An observation was made that the sample's compactness degrades after medium change and transfer

[4]U-bottom refers to the round shape assumed by the well - such geometry imposes cell aggregation upon sedimentation. The number of wells in such plates - 96 - grants high culture throughput.

into flat bottom wells to new conditions (40% O_2, 5% CO_2 and 37°C) that takes place on day 7 according to the protocol. From that, it was concluded the stress the that the sample experiences upon transfer is having a negative impact on its development. Therefore, the decision was made to simply fill-up the U-bottom wells in with fresh medium and not change plates until day 10.

3.2.3 Mycoplasma contamination

Only after the experiments were performed mycoplasma contamination was detected in the received batches of cells.

3.2.3.1 What are Mycoplasma?

Mycoplasma are small procaryotic organisms with a minimalistic organelles composition, which is mainly accounted by the cell membrane, ribosomes and a circular double stranded DNA. Since they do not posses a cell wall they show high resistance to β-lactam antibiotics (e.g., penicillin). Mycoplasma contamination in cell cultures affects general cell homeostasis. It can among others alter cellular metabolism, signalling and differentiation. In addition, it can induce chromosomal aberrations and change cell membrane composition (surface antigen and receptor expression)[135]. It is important to mention that the problem of mycoplasma is difficult to tackle and wide-spread as 15 to 35% of cell lines in cell banks both in USA and in Europe are estimated to be affected [136].

3.2.3.2 Did mycoplasma presence affect the culture?

It is possible that the presence of mycoplasma in a 2D monolayer goes undetected as it might not affect the proliferation and behaviour of cells in a culture with a reduced dimensionality. However, the complexity of the development of a 3D tissue exposed the compromised metabolism of cells and impact on other aspects of their physiology. Therefore, the culture could not develop long-term. Similar findings have been reported by Desrochers et al. [137] where they observed effects upon the number, size and structure of *in vitro* generated 3D kindey cysts, where no such effects manifested for 2D culture.

3.2.3.3 How to detect mycoplasma contamination?

One of the means of testing cultures for mycoplasma contamination is to measure the presence of mycoplasma-specific enzymes in culture medium with the use of commercially avaiable kits. The test used in this thesis (MycoAlert Assay) exploits enzymes catalyzing the conversion of adenosine diphosphate (ADP) into adenosine triphosphate (ATP) (acetate kinase or carbamate kinase cite patent by Pitt et al., EPO, 2012).

The tested sample is examined before (Reading A) and after (Reading B) the addition of Mycoalert substrate. ATP levels in mycoplasma positive samples will increase which will be reported by a bioluminescent reaction with the use of a luminometer. In mycoplasma negative samples reads before and after addition of the substrate

will not be affected. The ratio of the two reads yields information whether the culture is mycoplasma positive or negative. It is accepted that B/A Ratio > 1.2 is indicative of a contaminated sample, for B/A Ratio < 1 the sample is mycoplasma negative and B/A Ratio $1 - 1.2$ is boreline and re-testing the cell line after 48 h is recomended.
The earliest passage available (#8) and a later passage (#9 and #10) were tested.

Table 3.3: MycoAlert assay performed on the cell line mESC gecoR H2B

passage	A	B	B/A
positive ctrl	18.298	68.184	3.7
negative ctrl	25.702	10.314	0.4
#8	14.704	48.839	3.3
#9	10.599	40.384	3.8
#10	158.416	14.023	11.3

$$\mathrm{ATP} + \mathrm{Luciferin} + \mathrm{O_2} \xrightarrow{\mathrm{Mg^{2+}}\ \ +\mathrm{Luciferase}} \mathrm{Oxyluceferin} + \mathrm{AMP} + \mathrm{PPi} + \mathrm{CO_2} + \mathrm{h}\nu \quad (3.5)$$

where *Luciferase* is an enzyme that produces light ($h\nu$) when it oxidises its substrate, *Luciferin* into *Oxyluciferin* in the presence of magnesium ions (Mg^{2+}), AMP is adenosine monophosphate, PPi is pyrophosphate, O_2 and CO_2 are molecular oxygen and carbon dioxide respectively.
All three samples display extremely high B/A ratios, in fact, 2 out of 3 are higher than the positive control. The result clearly indicates that the culture was contaminated with mycoplasma before it arrived to our lab.

Importantly, this explains difficulties that were faced to keep their 3D culture longer than 10 days.

3.2.4 Recipe for 3D neural organoids

Below, readers interested in the creation of the sample used in this thesis will find a detailed protocol with media compositions and other instructions. The growth of the sample in analogy to the one presented in the background section (Figure 2.7) can be seen on Figure 3.17.

Embryonic stem cell culture (ES)
Mouse embryonic stem cell line (kind gift from Yung Su Justin Kim from Dr. Ivan Bedzhov, MPI Münster) were maintained under 5% CO_2 and 37°C conditions on 10% gelatine-coated (Sigma, G1393) T25 flasks in DMEM high glucose medium (Sigma D5671) containing 15% FBS (Sigma S0615), 100 U/ml Penicillin-Streptomycin, 2 mM L-Glutamine, 1 mM sodium pyruvate (Sigma, S8636), 0.1 mM NEAA (Sigma, M7145), 0.1 mM 2-mercaptoethanol (Sigma, M3148). Maintenance medium was freshly supplemented with 0.44 nM mLif (Amsbio, AMS-263) 0.4 μM PD 0325901 and 3 μM CHIR 99021 inhibitors (Cayman Chemicals). Seeding cell number was set to 4.2 x 10^5 cells (for 2 day interval passaging) or 1.5 x 10^5 (for 3 day interval

passaging).

Induction of neural differentiation of ES cells Protocol to generate retina organoids adapted from [72, 73]. mES cells were dissociated in 0.25% EDTA trypsin (Gibco, 25200056), centrifuged (5 min, 1000 rpm) and resuspended in differentiation medium to achieve cell count 3 x 10^4 ml. To form embryoid bodies, cells were allowed to reaggregate in U-bottom 96 well plates (3 x 10^3 cells per well) (Nunc). Differentiation medium was G-MEM-based (Gibco, 21710-025) supplemented with 1 mM sodium pyruvate, 0.1 mM NEAA, 0.1 M 2-mercaptoethanol and 1.5% Knock-out Serum Replacement (Gibco, 10828-028). The culture was kept under 5% CO_2 and 37°C conditions for 7 days and afterwards each well was filled with additional 200 μl of maturation medium I and transferred to 40% O_2, 5% CO_2 and 37°C conditions. Maturation medium I was DMEM/F12 supplemented with 100 U/ml Penicillin-Streptomycin and 1% N-2 Supplement (Gibco, 17502048). On day 10, spheroids were di- or tri-sectioned under a stereomicroscope (Nikon, Stereoscope), transferred to low adhesion 24-well plates filled with maturation medium II and placed back into 40% O_2, 5% CO_2 and 37°C conditions. Maturation medium II was DMEM/F12 freshly supplemented with 100U Pen/Strep, 1% N2-suplement, 0.5 μM retinoic acid (ec23®, SRP002), 1 mM taurine. By day 15, the culture was stopped.

3.2.5 Neuronal activity reported by Ca^{2+}

In this work, a cell line modified to endogenously (on its own) produce indicator molecules (R-GECO1) has been used. Thus, in this strategy the sensor did not have to be delivered. What has to be stressed is that the response function of the sensor

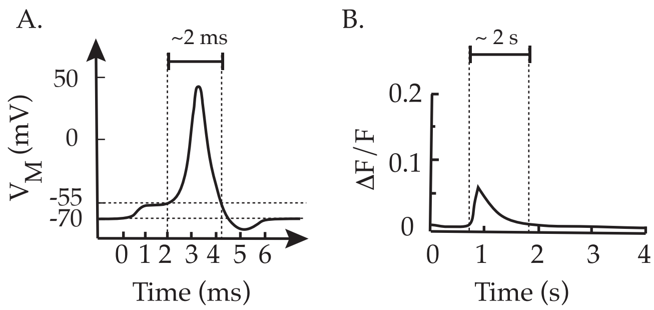

Figure 3.14: **Response to an action potential A.** Membrane potential as a funtion of time during an AP occurs within milliseconds whereas B. Response of the calcium sensor measured as a change in fluoresnece signal over time changes over a timescale of second. Data of R-GECO1 response reproduced from [138].

as a reaction to the memebrane depolarization due to an AP is a factor of 1000 slower (Figure 3.14). That means the width of the observed calcium spikes will be much broader than the width of an actual AP spike.

3.2.6 Reproducible sample mounting for light-sheet imaging

The light-sheet beam exits the aspherical lens at the height of 2.5 mm with respect to the bottom of the Petri dish (Figure 3.15 A). Because of that, for the beam to reach the sample to be imaged is has to be mounted at least at this height. The procedure involves few easy steps and and yields reproducible, simple to manipulate and use imaging chambers:

• The two plates are first joined together and placed on a clean surface.
• Warm liquid 2% agarose (2% high gelling temperature in ddH2O) is pipetted between them.
• The well-template is then placed on top of the plates and the assembled mold maker is moved to 4°C.
• Once agarose solidifies, the well-template is carefully lifted and the plates sequentially removed.
• As a result, a transparent block of agarose with a hollow well is obtained. Thin transparent wells can be cut out and used as single-use imaging chambers.
• Such chamber is then fixed to a glass-bottom Petri Dish between two parafilm stripes with the use of warm liquid agarose.
• As a last step, an organoid is transferred with a tip-cut P200 pipette to the well and the dish is filled with a medium of choice. For that purpose, a simple mold

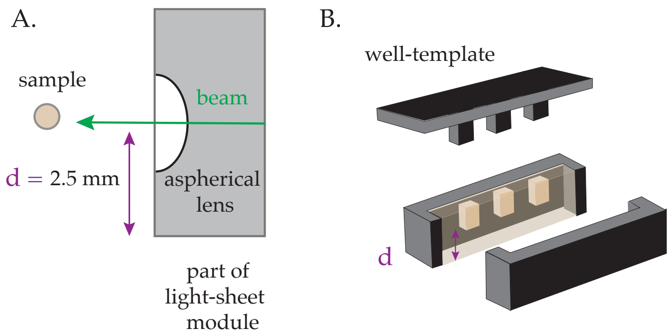

Figure 3.15: **Sample mounting consideration A.** The beam is focused by the aspherical lens in the FOV at a minimal height of 2.5 mm. B. Schematic drawing of a molder maker that would allow for the generation of thin, hollow agarose wells that could host samples.

maker was designed (Figure 3.15 B). The mold maker consists of two twin plates and a well-template. The design was translated into an Autodesk Inventor drawing which could be printed (Figure 3.16).

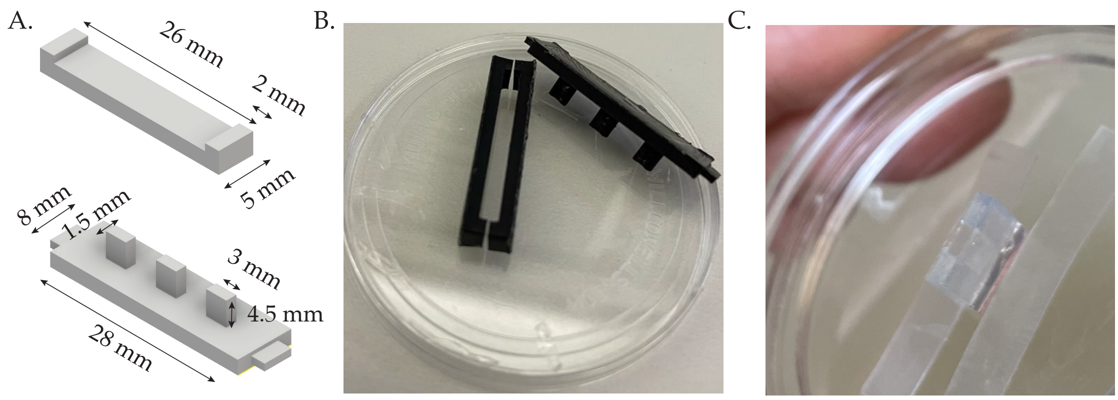

Figure 3.16: **Design and realization of imaging chamber A.** Design of the mold maker in Autodesk Inventor B. 3D printed elements C. Example of the imaging chamber that is used during the experiments.

3.2.7 Sample development monitored using Light-sheet Microscopy

Even though organoids could not be maintained until day 24 as in the original protocols [72, 73] organized structures were grown that could be further used in studies of early functionality emergence (Figure 3.17).

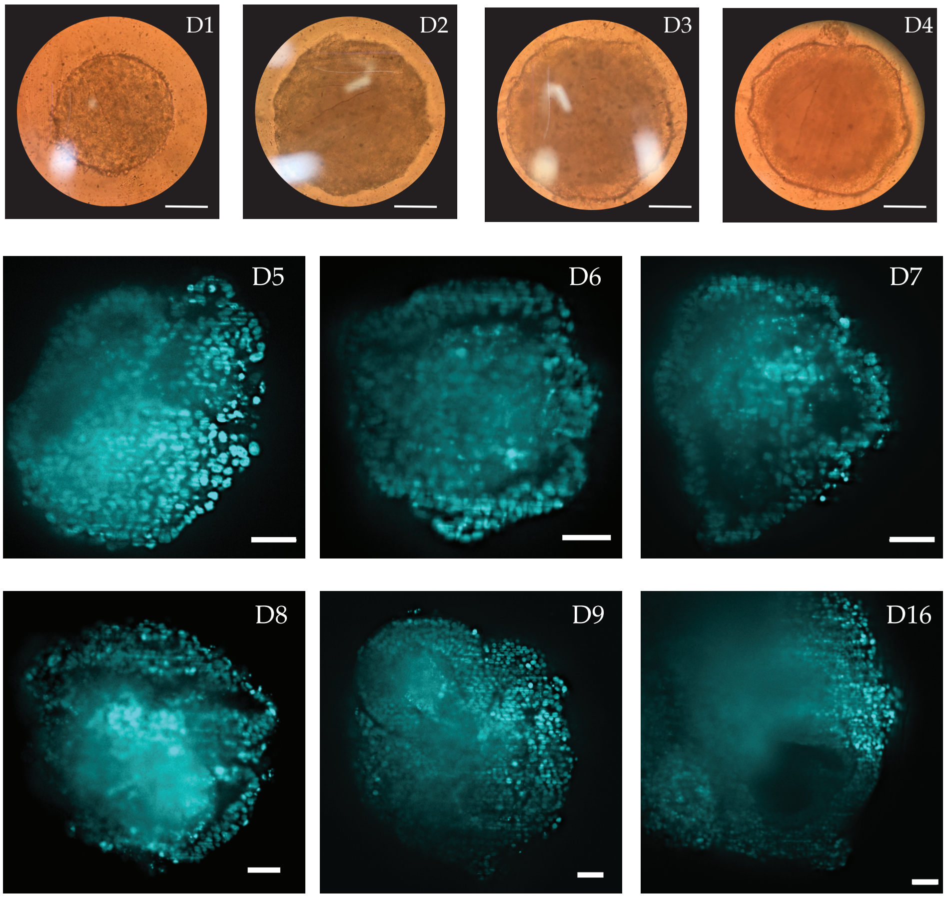

Figure 3.17: **Organoids Development** Structure emergences in organoids during their growth. During the first 4 days (D1-D4) cells in the inital agregate self-organize which manifests itself by the appearance of the characteristic disk-like structure (D4). Thanks to the H2B-GFP (cyan) we can monitor structural changes by imaging radial and layered organization of the nuclei in the growing organoids. Between D5-D16 a change in size of about a factor of 2 occurs. Images from D1-D4 were aquired with widefield microscopy in the cell culture and images from D5-D16 were acquired with our light-sheet setup. D5-D16 Images were filtered with a Unsharp Filter (radius = 4 or 6 pixels and weight mask = 0.6). Scale bar: 50 μm.

3.2.8 Architecture of the sample

Whole-tissue staining might not result in a clear readout since penetration of antibodies across multiple cellular layers is limited. Fortunately, the cellular composition of organoids can be determined by performing immunostaing on frozen sections of the tissue (cryo-sections).

3.2.8.1 Neural identity of the tissue

To confirm successful differention into neurons, D 12 organoids were cryosectioned and stained for neural progenitor markers (Figure 3.18). Each section was stained for one marker in the far red channel (alexa 647) as the green and red channel were not available. Three markers were selected : nestin, SOX2 and Pax6 [5]. The presence of nestin and SOX2 was confirmed. Specific secondary antibodies bound towards the cellular membrane and nucleus respectively/ This did not occur in the control sample. On the other hand, Pax6 staining was not successful as secondary antibody displayed in case of the sample and the control an ubiquitous non-specific binding. (Images are maximum intensity projections (MIP) of double channel z-stacks acquired with Zeiss LSM 980.

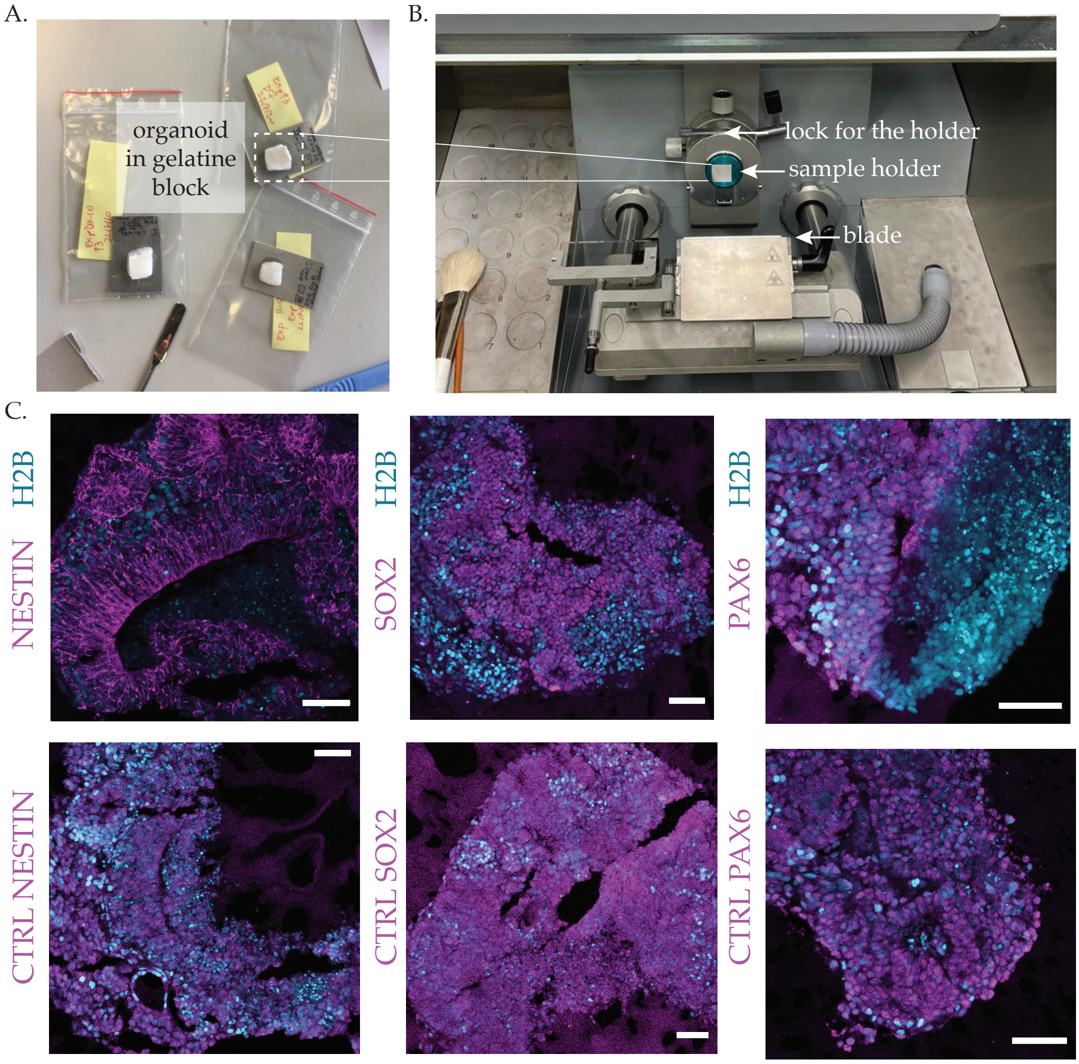

Figure 3.18: **Cryosectioning of neural organods A.** Frozen gelatine blocks embedding organoids B. Mounting of a block in a holder C. Stainings of sections, upper row is the sample and lower row is the control. Scale bar: 50 μm.

[5]Nestin is an intermediate filament protein, produced in the cytoplasm of stem and progenitor cells [139, 140], and SOX-2 [141] and Pax-6 [142] are both transcription factors that show localization to the nucleoplasm.

3.2.9 Sample intensity as a function of input laser power

Due to the camera bandwidth limitation, the fastest frame rate achievable in the current setup's configuration is 100 fps. To increase volumetric scanning rate a frame exposure of 10 ms has been set. To excite the most photons from the sample the power of 561 nm laser was set to 100 %. The output intensity signal from the sample as a function of input power was measured (Figure 3.19). Intensity signal was dark current-corrected, by evaluating the signal without laser excitation at 10 ms. The signal is about $1.6x10^3$ arbitrary units (Supplement Figure 6.3)

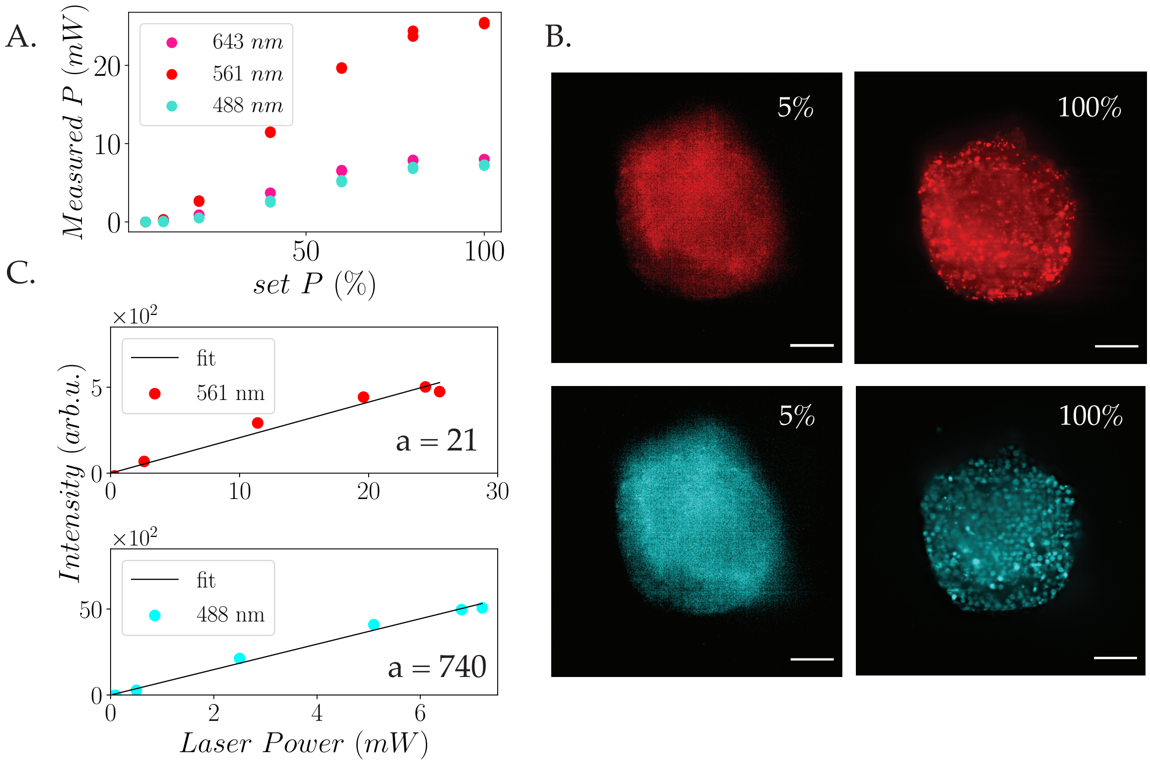

Figure 3.19: **Output signal as a function of laser input power A.** Mapping of input laser power set in the computer interface in percent and the resulting output power in mW at the exit of the fibre as measured by a power meter (Thorlabs). B. Single planes (4x4 binning, 20x/ 0.5 W, Olympus) from samples acquired at different laser powers for a 10 ms exposure time. C. Mean Image Intensity value corrected for dark current of the camera as function of power as measured by the power meter in A. for a 10 ms exposure time. For display purpose, Unsharp Filter has been applied on the images (radius = 6 pixels, mask weight = 0.6) (Scale Bar: 100 μm (B.))

The non-linear behaviour between the input and output visible in Figure 3.19 A. is a result of non-perfect digital to analog signal conversion and not fluorophore saturation what is proven when image mean intensity is plotted versus actual laser power not the percent laser power.

3.3 Functional imaging

Adding complexity to a system is a way to gradually deepen its understanding. Therefore, neuronal activity of the sample as reported by calcium indicator R-GECO1 is first explored in 2D with the use of confocal microscopy (Figure 3.20) and next in 3D, with the light-sheet setup.

3.3.1 Confocal microscopy: 2D functional imaging

In terms of kinetics, R-GECO1 displays a 0.09 ± 0.02 s time-to-half-rise and 0.78 ± 0.13 s time-to-half-decay of action potential-evoked fluorescence[143]. With a an

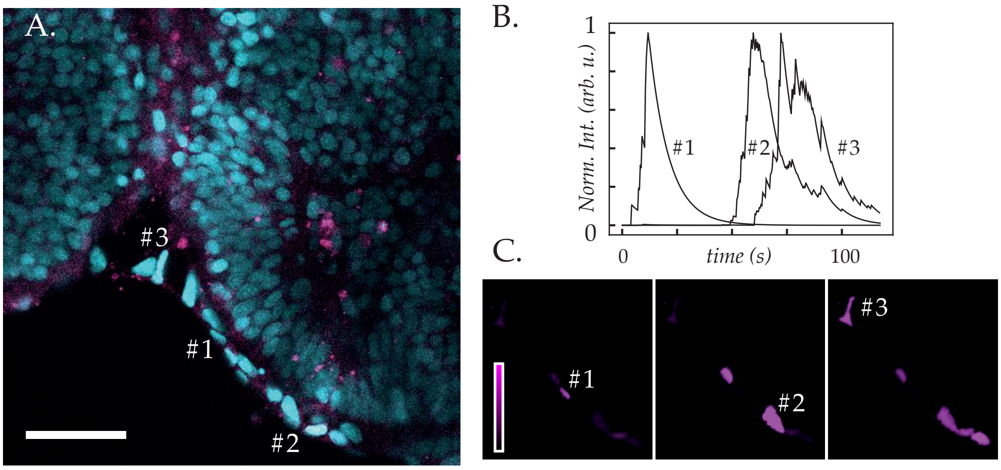

Figure 3.20: **Confocal 2D Ca^{2+}imaging A.** Confocal fluorescence image of a day 11 neural organoid (cyan:H2B; magenta:R-GECO1). B. Signal propagating across 3 neurons selected in A. shown in separate panels in C. Exposure time was set to 320 ms per frame, images were acquired with LSM 920 Zeiss, 40x/1.2 W. Scale bar: 50 μm, Color bar: 0-1 in normalized arbitrary units

320 ms exposure time per frame, the decay of the signal can be sampled in a way that satisfies the Nyquist condition (Figure 3.20) in a 2D single plane time series.

3.3.2 Light-sheet microscopy: 3D functional imaging

As a final assessment of the setup's capabilities, functional imaging of a D10 neural organoid will be discussed. First the imaging conditions and settings will be presented. Next, necessary pre-processing setups will be pointed-out. Finally analysis results will be put in context using concepts from graph theory.

3.3.3 Setting up light-sheet microscopy experiment

Conditions in setup's incubation chamber were adjusted to physiological conditions of 37 °C and 5 % CO_2 and left for equilibration. Lasers 561 nm (functional imaging) and 488 nm (structural imagin) were turned on and allowed to heat-up. An imaging chamber was prepared as described 3.2.6.
Imaging was performed with a water immersion objective (Olympus, 20x/0.5 W) which resulted in a 665 x 665 μm^2 FOV. Pixel binning is set to 4x4 which creates 512x512 pixel images. Z-step was set to 3 μm. Therefore, by setting the number of z-planes to 20, the sample was inspected up to 60μm deep in the tissue. Exposure time per frame is set to 10 ms which is the maximum acquisition rate the camera could offer (100 frames per second). With 200 ms per volume, a bidirectional scanning rate of 5 Hz was achieved (5 vol/s).
The structure of the network was examined by imaging the GFP channel of the

nuclei using the 488 nm laser (Figure 3.23 A.). The presence of characteristic neural rosettes was assessed. Next, a 200 s long functional imaging was performed.

3.3.4 Image processing

Image processing includes three steps. In the first, images are re-ordered using a self-written Fiji script. Afterwards they are filtered to remove low-frequency contributions using a Fourier Filter (3.21). Next, images are motion corrected and the matrix factorization CaImAn pipeline is initiated. All the steps will be demonstrated on a single dataset.

3.3.4.1 Filtering

The user removes from the data low-frequency contributions by applying the previously described filter (Figure 2.18). That way, only smaller objects, which have the potential of being active neurons are preserved in the FOV of the raw volumetric data (Figure 3.21 A and B). Next, in the process of matrix factorization, spatio-temporal calcium activity of active neurons in the FOV is extracted (the AC signal in Figure 3.21).

Raw data are written as Integer, 16 Bit Unsigned: meaning the unsigned whole or natural numbers range from 0 to +65535. The filtered and processed data (AC) are written as Integer, 16 Bit: Signed Integers and range from -32768 to +32767. This explains why on the histogram (Figure 3.21 C.) the signal of the raw data adopts only positive values and the one of the filtered and processed data both positive and negative. Importantly, it can be noticed that with each processing step the signal content decreases, so that the AC signal of active neurons is effectively very small compared to the background and noise.

3.3.5 Motion Correction

To compensate for rigid and non-rigid transformation the sample is undergoing throughout the imaging session, the data is motion corrected right before the matrix factorization step. NoRMCorr algorithm is applied to identify shifts along x, y and z direction and correct for them (Figure 3.22). The shifts in all axes does not exceed 2 pixels which corresponds to 2.6 μm.

Interestingly, motion along x and z displays a similar behaviour, that is somewhat the reverse of the one along the y axis.

3.3.6 Reconstruction of spatio-temporal calcium activity

In the following section, the output data obtained with the CaImAn pipeline will be further analysed. The main information of interest that is extracted are the A and C matrices that store respectively the spatial footprints of firing neurons in the FOV and their activity traces. The product of the two can be used to reconstruct the spatio-temporal profile of the imaged structure.

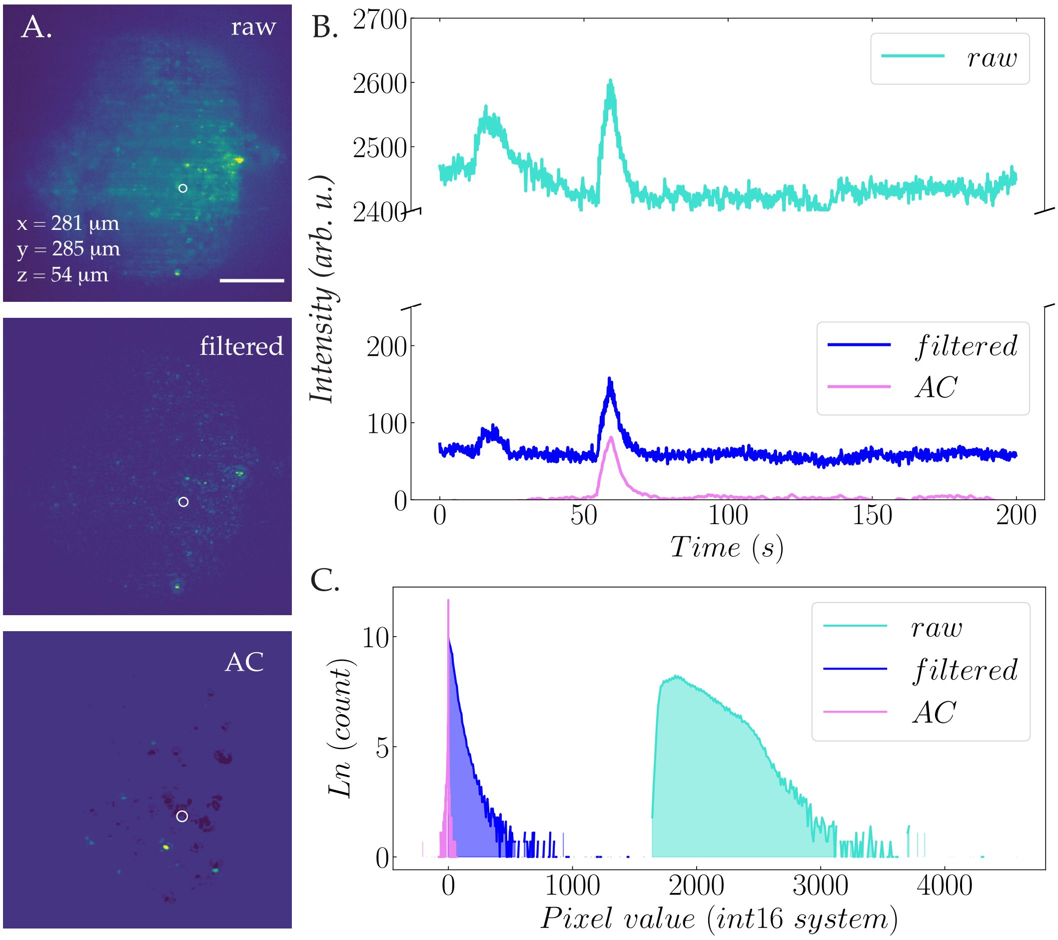

Figure 3.21: **Fluorescent trace of raw vs low-frequency filtered and CaImAn processed region of interest A.** In the raw data, a region of interest corresponding to a firing neuron (white circle, with x,y,z coordinates) is selected. In the pre-processing and processing steps, the background and noise signal are removed from the images so that in the end, only a small portion corresponding to the neuronal calcium activity remains visible upon fluorescence trace inspection (B.) The gradual removal of irrelevant signal from the data can be traced by plotting a histogram of pixel values corresponding to raw, filtered and final data. Because the raw data is written as Integer, 16 Bit Unsigned as oppsed to the filtered and AC data (Integer, 16 Bit: Signed Integers) the pixel value ranges are different.

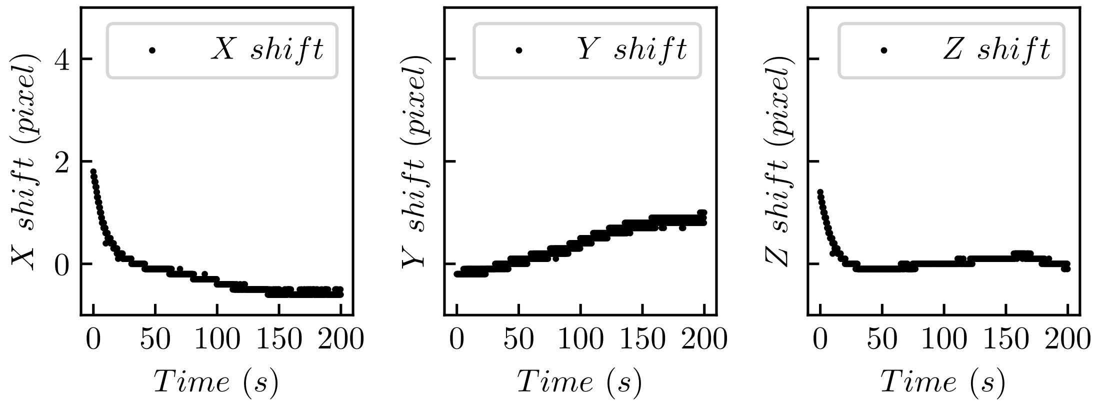

Figure 3.22: **NoRMCorr Motion correction along x, y and z axis** for a shift of about 2 pixels along all the three axes is made (2.6 $\mu\, m$). The motion along the x and z axes follows a somewhat similar trend that seems opposed to the trend of the motion along y axis.

3.3.7 Active neurons in the FOV

Not every neuron in the network seems to be firing. At least this is the observation that can be made for this dataset according to the result presented in Figure 3.23. The structure of the sample can be inspected thanks to the endogenously expressed nuclear marker H2B-GFP (Figure 3.23 A.). On the other hand, the structure reconstructed using identified footprints from the A matrix does not involve all of the neurons visible in the structural channel. As a rough estimate of the maxima identified in both channels (maxima location tool, Fiji), only around 1/6 of the all the neurons in A. displays a firing behaviour in B. The centre of mass of each spatial footprint is known, what allows to compute the centre of mass of the entire active network (Figure 3.23 B.). Its location with respect to the overall approximate shape of the structure, suggests a rather homogenous distribution of firing neurons in the tissue.
Visual inspection of the activity traces of identified neurons plotted as function of time (Figure 3.24 C.) constitutes a first sanity check for successful segmentation of the structure in the FOV. In case the same trace is present for what has been identified as separate neurons, the values of parameters, such as the threshold for component merging need to be optimized.

The number of firing neurons in this dataset is equal to 102 (Figure 3.24 C.). Components output by the CaImAn algorithm were manually inspected to select good traces. In the future, the analysis pipeline can be fully automatized. One of the ways this can be done is currently being developed by Filippo Kiessler (master student at the Faculty of Physics, LMU). He developed a Variance Filter that uses the variability of the spatial fast fourier transform of the raw dataset to filter out the unwanted background structures, and leaves the neuron signal mostly unaffected

3.3.7.1 Interactions between neurons

Before all the traces shown in Figure 3.24 C. are subject to a correlation analysis, it will be instructive to inspected pairs traces corresponding to neurons localized at

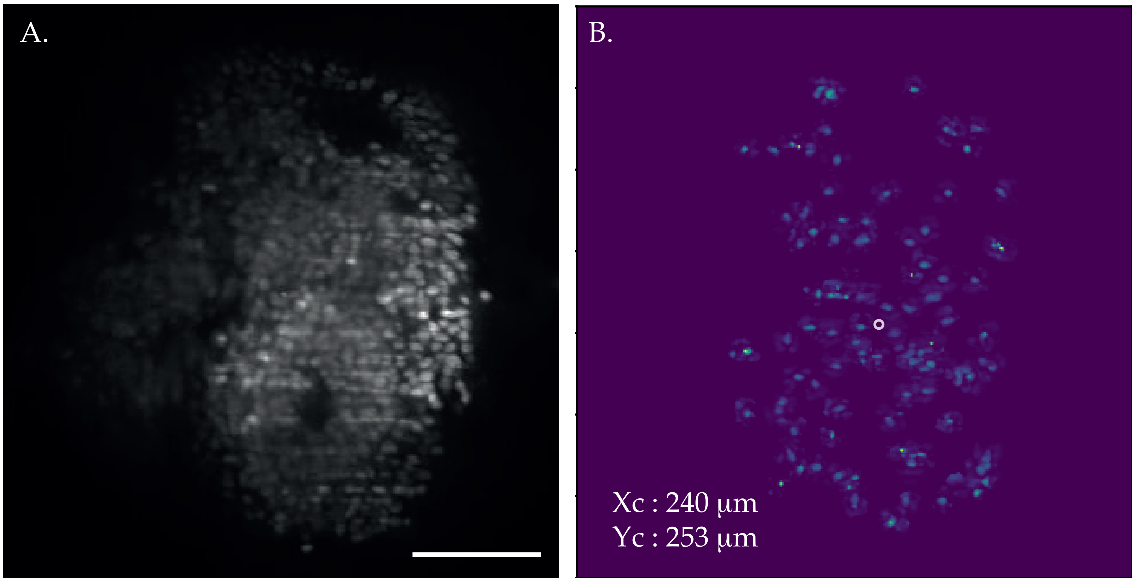

Figure 3.23: **Active neurons in the FOV A.** Unsharp masked raw image of the H2B-GFP expressing organoid B. Maximum intensity projection of the spatial footprints of active neurons identified in the FOV. White dot corresponds the computed center of mass of the structure (scale bar: 100 μm)

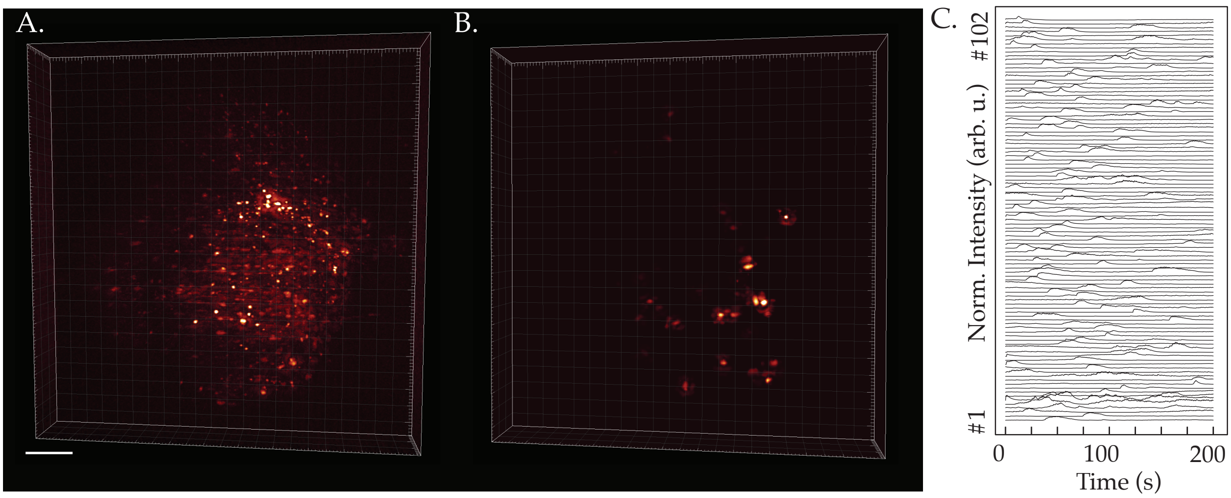

Figure 3.24: **Extraction of active neurons A.** Single time frame from a low-frequency filtered 4D functional imaging of an organoid B. The same time frame obtained by reconstruction of processed data. Only active neurons are present in the FOV. C. De-noised, 0-1 normalized fluorescent traces of neurons (in the number of 102) identified in B. (Scale bar: 40 μm)

different positions in the FOV (Figure 3.25). One could roughly say that neurons in A. and B. seem to be firing very close in time and that the activity of neurons C. and D. is rather shifted one with respect to the other. Following on that, it is interesting to learn that the distance separating neurons in A. B. is larger (68 and 50 μm respectively) than the distance separating neurons in C and D. (33 and 19 μm respectively). It seems that the position in the network and distance between neurons is not the primary factor dictating possible types of the interactions.

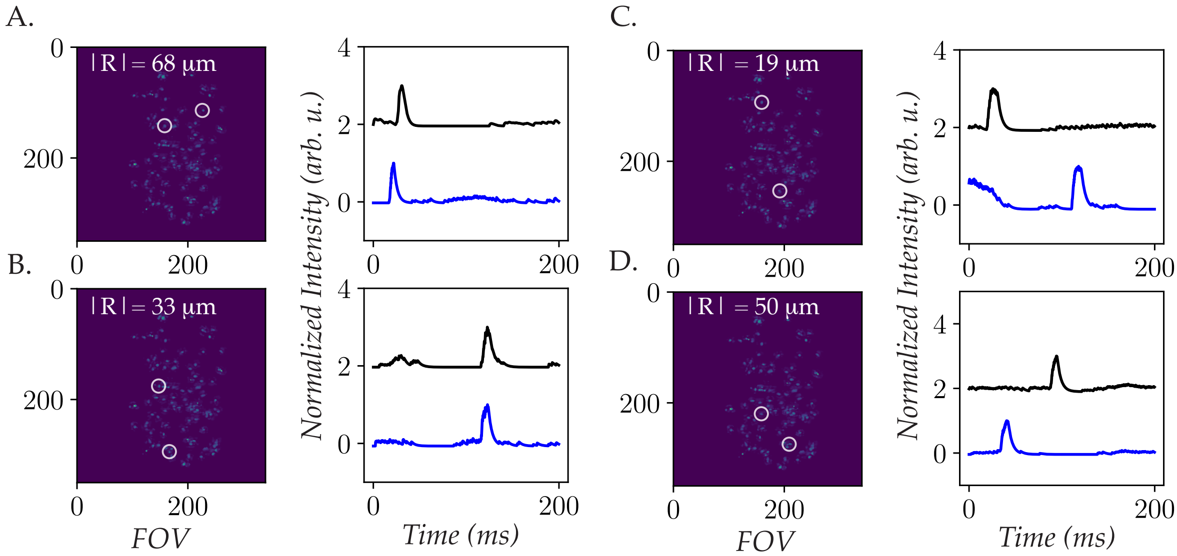

Figure 3.25: **Possible neuronal interactions** All panels depict a pair of neurons localized at different distances with respect to each other in the FOV (in pixels) and their corresponding 0-1 normalized traces. Separation between pairs of neurons in 3D indicated by $|R|$ is equal to A: 68 μm, B: : 33 μm, C: 19 μm, D: 50 μm. One trace in each pair is offset for display purposes.

3.3.8 Directionality in the signals

In future analysis, it would be useful to define whether neurons establish sender-receiver dynamics. To obtain first insights into that, time-lagged correlation analysis can be performed. As an example, time-lagged cross correlation of traces B. and C. from Figure 3.25 are presented (Figure 3.26).

The interpretation of the cross-correlation curves in both cases is not obvious. Detection of peaks by eye seems a rather straightforward task in both cases. Roughly speaking, peaks in A. are shifted one with respect to the other for about 100 s and and in B. they seem to happen at the same time. Therefore the time-lagged cross correlation should show a peak for $\approx \Delta t = 100$ and $\approx \Delta t = 0$ respectively. It is not exactly what happens. Although the expected peak does show for more or less the expected Δt some other features are displayed in both cases. The reason for that is that the traces are far from displaying delta-function like peaks. Other irregularities are present which distort the structure of the time-lagged cross correlation.
Importantly, traces in the example show only a single peak. One can only imagine that the situation becomes even worse in the presence of multiple peaks. The need for a robust algorithm for the deconvolution of the spiking trains from the dynamics of the calcium indicator becomes more obvious.

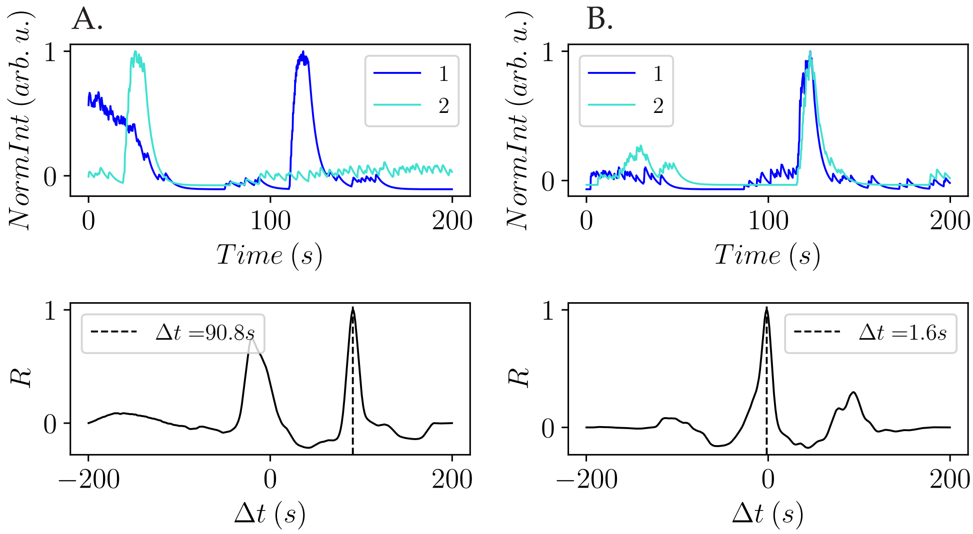

Figure 3.26: **Time Lagged Cross Correlation of experimental data.** Operation is performed on traces shown in Figure 3.25. A. Highest correlation is obtained for a lag of 90.8 s which corresponds to the time shift of the two peaks in trace 1 and 2. However, a large and somewhat misleading correlation peak is also present for lag 0 s. It is due to the overlap of the broad unstructured band present in the first 30 s in trace 1 with the well-structured peak of trace 2. B. Traces 1 and 2 display peaks at almost the same and therefore the largest correlation is obtained for a lag of 1.6 s. The non-symmetric shape of the correlation peak is the result of the overlap of the smaller peaks present in two signals around time = 20 s.

3.3.9 3D connectivity map of the network

A more quantitative analysis of the interactions involves measuring of the global synchrony between neurons in the network. This is achieved by computing Spearman rank correlation matrix for each possible pair of neurons. The coefficients (R_S) reflect the strength and type of interaction that exist between them. The diagonal represent the autocorrelation of the neuronal trace with itself and is therefore equal to 1 (Figure 3.27 A).

Small patches of strong ($|R_S| > 0.8$) positive and negative correlations can be distinguished. It is possible that by such interactions a functional circuits form, where neurons engage in the same type of activity. Interestingly, R_S values follow a Gaussian distribution and adopts mostly values between -0.4 and 0.4 (σ) with a mean μ close to 0 (Figure 3.27 C.). This means the inter-neuron interaction landscape is dominated by weak interactions. Moreover, it seems that the strength of the interaction between a pair of neurons (measured by value of the correlation of the R_S coefficient) does not depend on the distance separating them (Figure 3.27 B.). That would suggest that the speed at which the interactions propagate is high and faster than the response time of the sensor.

3.3.10 3D network of active neurons

Since the positions of all the components can be computed, it is possible to represent the network and interactions of its units in 3D (Figure 3.27 D.). For that, use is made of basic graph theory where neurons become nodes of an undirected graph

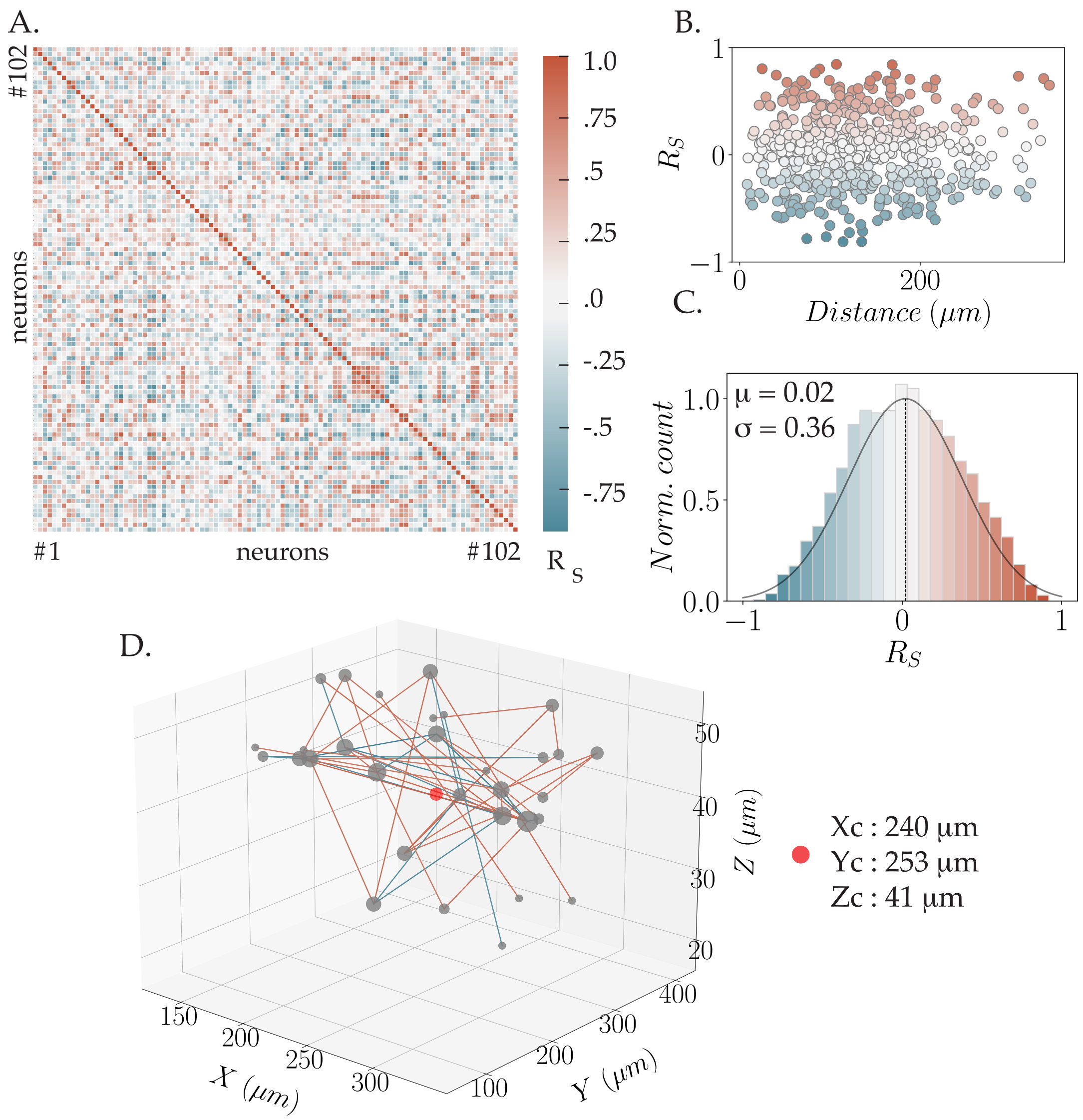

Figure 3.27: **3D Connectivity analysis A.** Spearman rank correlation matrix of all 102 active neurons identified in the FOV. The value of the correlation ranges from 1 to -1. Positive correlation value suggest two neurons are likely to fire together while in case of a negative correlation, the firing of one neuron is likely to inhibit the firing of the other in the pair. B. Correlation coefficients are plotted as a function of the distance between neurons in the pair for which the correlation is computed. C. A histogram of all the correlation coefficients from A. is computed. One can notice that it follows a Gaussian distribution, and that week interactions (around 0) contribute the most to an entire pool. D. 3D representation of interactions in structure using a graph layout. Nodes correspond to active neurons and the edges represent their interaction with the rest of the network. Edges are color-coded according to A. To remove possibly spurious interactions, connections with $R_S \geq 0.8$ are displayed. Node size is degree coded. The red dot corresponds to the centre of mass of the structure.

and the connections between them - edges - are colour-coded according to the correlation coefficient computed for this pair. To keep only the strongest connections and remove possible false ones, a threshold is set, namely $|R_S| > 0.8$. The result of such operation is depicted in Figure 3.27 B. The subset of nodes and edges forms a graph where nodes posses direct and/or non-direct functional connections to other units. In addition, node size is degree coded - the more connections a node has the bigger it appears in the graph.

Synaptic modification and refinement during the activity-dependent neural development is believed to be achieved via correlated activity (an idea originally proposed by Hebb [144] and further extended by others as reviewed by Bi and Poo [145]). It is possible that local spontaneous activity correlation observed for small groups of neurons extend later on to global synchrony as a result of the emergence of a functional neuronal circuit.

Such hypothesis can be explored by imaging the network of a neural organoid at other developmental stages.

3.3.10.1 Which interactions matter?

Thresholding network connections to keep only the strongest ones was just one of the possible ways to start network analysis. It has been reported that weak firing correlation between neighboring pairs of neurons in vertebrate retina are relevant for the maintenance of strongly correlated network states upon visual stimulus presentation [146]. Therefore, both strongly and weakly correlated interactions should be looked at.

3.3.10.2 Receivers, Renders and Brokers nodes

Moreover, to obtain more detailed information on the dynamics of the signals in the network, time-lagged cross correlation between each pair of signals should be performed [147, 148]. This would allow for the study of local synchrony in the network, gain insight into the directionality between signals and help establish if a leader-follower relationship takes place between pairs of nodes. A similar approach was followed by Sharf et al. where receivers, senders and brokers nodes were identified in the human brain organoid network[7]. To permit such studies some changes would have to be introduced into our setup which will be discussed in 5.2.1 .

3.4 Cluster firing

Apart from an overall and at first site non-coordinate firing pattern, another behaviour can be observed. Namely, the firing of a cluser of neurons (Figure 3.28).

Excitingly, results obtained in Figure 3.28 allow for estimating the signal propagation velocity in the structure as reported by the R-GECO1 calcium indicator. Assuming the travelled distance to be r (Figure 3.28 A.) and time to be 35 s (Figure 3.28 B and C.) The velocity would therefore be approximately 1.4 μm/s. The result should be considered as merely showing the type of information one should be able to extract with the use of a setup similar to the one being discussed here. CaImAn pipeline identified the structure in Figure 3.28 B. as one component which seems to

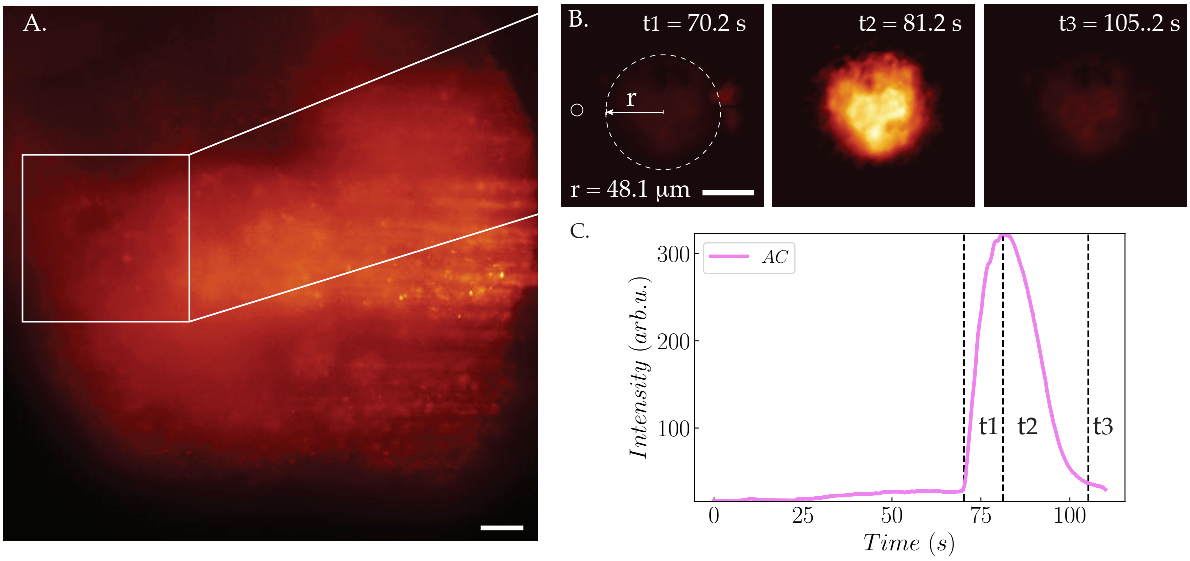

Figure 3.28: **Explosion behaviour** Calcium imaging of day 15 neural organoid in which the concerted firing of a cluster of neurons has been observed. Panel A represents maximum intensity projections of the entire organoid in the FOV with a selected region for which the cluster firing is observed. The small circle has been placed for comparison purpose - it has a diameter of 10 μm and corresponds to an average single neuron. B. Selected region at time t_1, t_2, t_3 which correspond to the time points right before, during, and right after the firing event marked as dashed lines in C. The images correspond to single planes extracted from a 3D activity reconstructed with CaImAn pipeline. C. Fluorescence trace extracted from one-plane time series belonging to a CaImAn-reconstructed 3D activity. Scale bar: 50 μm (A. and B.)

exceed the size of a single neuron - rather it is a cluster of multiple neurons displaying an activity so similar it has been identified as a single unit. Such behaviour could be explained if the neurons in the small cluster simultaneously received an input from another source. Cluster firing was observed in some form in both young(D7) and older samples (D15).

What is the difference between an overall firing and a cluster firing behaviour and where does is come from? What role does it have? Can one control it depending on the organoid growth conditions? To answer these and many other questions, further investigations need to be conducted.

3.4.1 Image segmentation - towards linking structure with function

To complement correlation analysis, real-time neuronal network morphology at high resolution should be characterized.

Network architecture is defined by spatial distribution and orientation of its units (neurons) and the shape of their arbours (dendritic inputs and axonic output) which strongly impact network connectivity. Such information can therefore be used to deepen the understanding of the structure-function relationship in the nervous system at the circuitry level[149, 150]. Depending on the type of fluorescent reporter that is introduced into the network, various features of the tissue can be obtained. For example, membrane labelling can allow for cellular shape retrieval.

3.4.1.1 Network structure deduced from the nuclear marker

In this study, a very approximated network architecture could be obtained using the structural channel where nuclei are visualized (Figure 3.29 A.). Simple image restoration operation (Top-Hat Filter 2.27) was applied to partially remove blur from image, which could then be segmented using Ilastik workflow. Segmentation result was then enhanced by applying a Watershed filter to separate nuclei that were merged (Figure 3.29 B. and C).

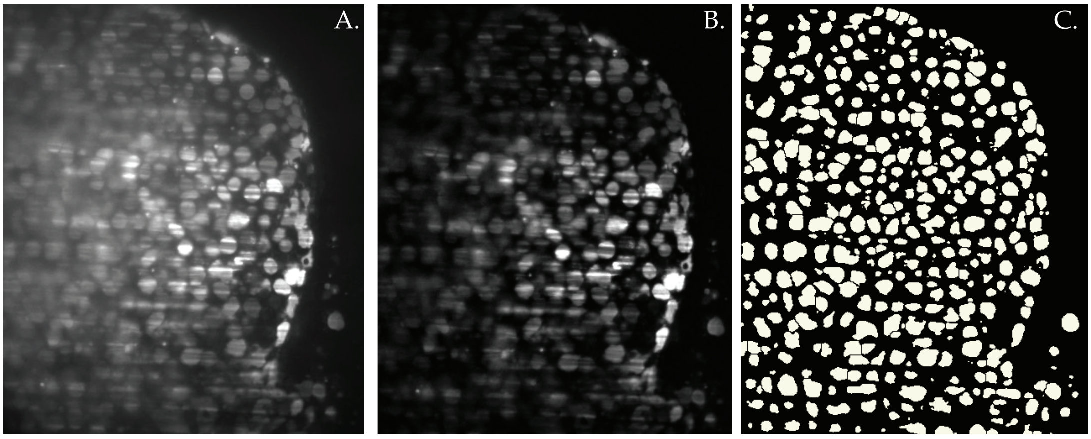

Figure 3.29: **Image Preprocessing** Simple image preprocessing consist of filtering the A. raw image with a Top-Hat Filter to B. partially remove the blur and be able to C. segment individual nuclei using a machine learning-based approach. First, Pixel and Object Classification Workflow with two categories was used to obtain a segmentation image that was next watershed transformed to separate nuclei that have been merged together.

In the resulting image pixels have been grouped and assigned to one of the two object categories: nuclei or background. The number of nuclei-objects along with their centre coordinates can be extracted. Such analysis could be done for an entire structural volumetric stack to for example characterize cellular density as a function of tissue depth ($\rho(R)$) with a recently developed deep learning-based segmentation method called Cellpose [151].

Chapter 4

Summary

"Slaby ze mnie
piastun nicosci
nigdy w zyciu
nie udalo mi sie
stworzyc
przyzwoitej abstrakcji"

— Zbigniew Herbert,
Epilog Burzy

This thesis was dedicated to the development of a low complexity experimental pipeline for functional imaging of neuronal systems. To achieve this goal, a light-sheet microscope tailored for state-of-the art calcium indicators and computational analysis tools has been developed.

The setup has been equipped with three laser lines to enable multichannel imaging. It provides a subcellular resolution in both lateral and axial directions for the two objectives used in the study (Tab. 3.1). In addition, the thickness of the light-sheet beam that can be generated (between 3-5 μm) allows for optical sectioning and resolving single neurons.

The volumetric imaging speed of the setup was maximized to 5 Hz by setting the stage into a bidirectional scanning mode, the frame exposure time to 10 ms, z step to 3 μm and the plane number to 20. With this, the setup can be placed among the state-of-the art instruments for functional imaging while maintaining a relatively low level of technical complexity.

In order to validate the setup, a fluorescent sample was created. For that purpose, a mouse embryonic stem cell line (kind gift from Bedzhov lab, MPI Muenster) was obtained, which intrinsically produced a fluorescent green nuclear marker and red calcium sensor. The presence and functionality of the two was confirmed in the experiments conducted in this thesis.

The potential of cells despite their mycoplasma contamination to differentiate into neurons was confirmed by performing pluripotency stainings. Next, a protocol for mouse retinal organoid culture was optimized and used to create a 3D neuronal network. The presence of neuronal markers was assessed using immunostaing of tissue cryo-sections generated in the lab with the use of a cryotome.

A mold-maker tool was designed and 3D-printed to allow for the creation of a transparent gel chamber that could host organoids for structural and functional imaging. The tool yielded reproducible chambers and was easy to use which tremendously facilitated the experimental procedure.

As a next step, 4D high speed volumetric imaging of the spontaneous activity in neural organoids reported by the red calcium indicator was carried out at 5 Hz (665 x 665 x 60 μm^3). It must be noted that the imaging of mammalian tissue is challenging as the sample displays highly scattering and light absorption properties in opposition to model systems such as the zebrafish.

Two types of firing patterns have been observed - overall and cluster firing. The latter, allowed for the determination of the signal velocity in the network which was about 1.4 $\mu m/s$. This is orders of magnitude slower than the conduction speed reported in both non-myelinated and myelinated neurons, which suggests that in the future, a faster sensor needs to be used. Excitingly, a new generation of calcium indicators has recently been created which have a rise time of few miliseconds [77].

Spontaneous activity is present in immature circuits in various regions of the central nervous system. It participates in the development of synaptic circuitry [152, 153, 154, 155]. Long before the onset of vision, mammalian retinal ganglion cells exhibit spontaneous, periodic bursts of action potential [156, 157, 147, 158]. It is not known how and to what extent such processes occur in a dish. This could be addressed in future studies.

Obtained 4D data was pre-processed with a custom written filter and analysed using an open source tool CaImAn. It applies the concept of constrained non-negative matrix factorization to reconstruct the spatio-temporal calcium activity of firing neurons in the field of view. Small spatial footprints of active neurons and their fluorescence activity traces are stored in two separate easily accessible matrices. Remarkably, calcium spikes can be extracted from a high noise and static fluorescence background.

Moreover, the data was analysed as a whole stack, not plane by plane. Such approach can provide insights into some aspects of the activity of 3D neuronal systems and its connectivity that could be missed otherwise.

Measurements performed in the frame of this thesis give information on the spontaneous behaviour of 3D-cultured and organized neurons. They constitute a first step in characterizing the functional connectivity of such systems.

As a next step, a directed or targeted stimulation (for example, using another laser source or a drug) could be used to study network dynamics by induced network activity. The response and relaxation of the system to such perturbation could help to deepen our understanding of the time and length scales that play a role in the emergence of functional neuronal circuits.

Chapter 5

Outlook and Prospects

"Above all, don't lie to yourself. The man who lies to himself and listens to his own lie comes to a point that he cannot distinguish the truth within him, or around him, and so loses all respect for himself and for others. And having no respect he ceases to love."

— Fyodor Dostoevsky,
The Brothers Karamazov

How to link together the experimentally obtained information on the architecture and activity patterns in a biological neuronal network and model them theoretically? For detailed discussion of the subject with focus on the brain, the reader is encouraged to look into [159, 160, 161].
The first complete mapping of nervous system at a cellular level and description in terms of a small-world network [1] has been done for Caenorhabditis elegans [162, 163].
Here, only a modest attempt will be made to look at the studied biological network in terms of a simple physical model with basic, well-defined properties.

5.1 Hopfield network

The complexity that even a few-unit neural network can display is astounding [164, 165]. Is there then a way to reasonably simplify the behavior of a multi-unit network to the degree it can be understood? In 1982 John Hopfield proposed a physical model, now called Hopfield Net, with emergent computational properties. The model consists of an ensemble of computing, fully connected devices - neurons. It can be regarded as an undirected graph where neurons are represented as nodes and the strength of their interactions is given by weighted edges. In addition, neurons can adopt one of the two states: not firing (-1) and firing at maximum rate (1).

[1] In a small world network, the path between two nodes tends to involve only a few edges. This notion is expressed by the popular *six degrees of separation* idea that any two people (nodes in a social network graph) can be connected by six of less acquaintances (edges.)

Such an ensemble probably reminded the reader of another model that describes a system of particles able to adopt one of two states - the Ising model!
In case of a ferromagnetic material, its atoms (ions) can be modelled as particles (sites) with a spin $\frac{1}{2}$ (up) or spin $-\frac{1}{2}$ (down). Spins flip and tend to align parallel to lower the energy of the system. This way long range spatial correlations of magnetization arise. It resembles a situation where adjacent neurons like to be (enter) the same state. Change of state of one neuron provokes the change of state in an adjacent neuron so that effectively a signal can propagate through the structure.

In order to show the close relationship between the Hopfield and the Ising Model, the energy of both systems will be discussed.

The total magnetic field h_i experienced by an atom i in an a system of atoms equals to the sum of the individual fields that each atom induces on their neighbor and and (if present) the external field h^*

$$h_i = \sum_{j=1}^{n} w_{ij} x_j + h^* \tag{5.1}$$

w_{ij} corresponds to the value of the magnetic coupling between the considered atom i and all the other atoms j. The potential energy of a given state in an n-element Ising material takes the form of :

$$E(\mathbf{x}) = \frac{1}{2} \sum_{i=1}^{n} \sum_{j=1}^{n} w_{ij} x_i x_j + \sum_{i=1}^{n} -h^* x_i \tag{5.2}$$

The factor $\frac{1}{2}$ is used because of the identical terms $w_{ij}x_ix_j = w_{ji}x_jx_i$ sum. For a Hopfield network of n-unit, a weight matrix W expressing the effectiveness of synapses can also be defined. Even though is is not likely to occur in biological networks, the matrix is symmetric meaning $w_{ij} = w_{ji}$. Once assigned, these weights do not change during a simulation. No unit is self-connected to avoid constant feedback of its own state value. In addition, a threshold activation value θ is assigned to each unit.

Biological synapses are activated by arriving action potentials and the incoming signal to a neuron i can be written as $w_{ij}x_j$. Neurons update their state asynchronously – each unit maintains its state until it is selected for an update. In that situation, the neuron evaluates the net contributions it received from other units

$$\begin{aligned} x_i &\rightarrow 1 \;\; if \sum_{j \neq ii} w_{ij} x_j > \theta_i \\ x_i &\rightarrow -1 \;\; otherwise \end{aligned} \tag{5.3}$$

And adjusts its state accordingly. The energy E($\mathbf{x}$) of a state $\mathbf{x}$ of the network is given by

$$E(\mathbf{x}) = \frac{1}{2} \sum_{i=1}^{n} \sum_{j=1}^{n} w_{ij} x_i x_j + \sum_{i=1}^{n} \theta x_i \tag{5.4}$$

Equation 5.4 is isomorphic to the equation 5.2.

How are the weights selected? A number of patterns μ corresponding to stable states can be stored in the n-unit network. A pattern is a n-long binary word that gives the configuration of active and non-active neurons in the network. Following the Hebb's learning rule [144] that states that simultaneous firing of a pair of neurons i, j increases the synaptic coupling between them it can be written that

$$W_{ij} = \sum_{\mu=1}^{p} \zeta_i^\mu \zeta_j^\mu \tag{5.5}$$

If the system is started sufficiently close to one of the states corresponding to those stable patterns it will settle in an energy minimum after finite number of time-steps. For example, the state of an n-unit network is given by a vector $\mathbf{x}$ which describes the configuration of firing and non-firing units. This network has several stable limit points given by vectors $\mathbf{x}_a$, $\mathbf{x}_b$, ... On the condition that the network is started sufficiently close to one of the stable point vectors, the network will adopts states located down the energy landscape to settle in one of local minimum.

As a an example, a simple 3-units Hopfield network(Figure 5.1 A.) can be studied. The state of each unit is defined as x_i, the symmetric weights connecting them are assigned just as the acitvation tresholds (θ). The network can take on 2^3 different states and for each, their energy in arbitrary units can be computed using equation 5.4 as

$$\begin{aligned}
&E\left(x_1 = 1, x_2 = 1, x_3 = 1\right) = -\tfrac{1}{2}\left(-2\right) + \tfrac{1}{2}\left(1+1+1\right) = -1 + 1.5 = \mathbf{0.5}\\
&E\left(x_1 = -1, x_2 = 1, x_3 = 1\right) = -\tfrac{1}{2}\left(2\right) + \tfrac{1}{2}\left(-1+1+1\right) = -1 + 0.5 = -\mathbf{0.5}\\
&E\left(x_1 = -1, x_2 = -1, x_3 = 1\right) = -\tfrac{1}{2}\left(2\right) + \tfrac{1}{2}\left(-1-1+1\right) = -1 - 0.5 = -\mathbf{1.5}\\
&E\left(x_1 = -1, x_2 = -1, x_3 = -1\right) = -\tfrac{1}{2}\left(2\right) + \tfrac{1}{2}\left(-1-1-1\right) = -1 - 1.5 = -\mathbf{2.5}\\
&E\left(x_1 = 1, x_2 = -1, x_3 = -1\right) = -\tfrac{1}{2}\left(2\right) + 1\tfrac{1}{2}\left(1-1-1\right) = -1 - 0.5 = -\mathbf{1.5}\\
&E\left(x_1 = 1, x_2 = 1, x_3 = -1\right) = -\tfrac{1}{2}\left(2\right) + \tfrac{1}{2}\left(1+1-1\right) = -1 + 0.5 = -\mathbf{0.5}\\
&E\left(x_1 = -1, x_2 = 1, x_3 = -1\right) = -\tfrac{1}{2}\left(-2\right) + \tfrac{1}{2}\left(-1+1-1\right) = 1 - 0.5 = -\mathbf{0.5}\\
&E\left(x_1 = 1, x_2 = -1, x_3 = 1\right) = -\tfrac{1}{2}\left(-6\right) + \tfrac{1}{2}\left(1-1+1\right) = 3 + 0.5 = \mathbf{3.5}
\end{aligned}$$

An energy levels digram with possible state transitions for the network can be created mapping states to their corresponding energies (Figure 5.1 B.). The interaction weights reflect the mean firing rate a neuron displays.

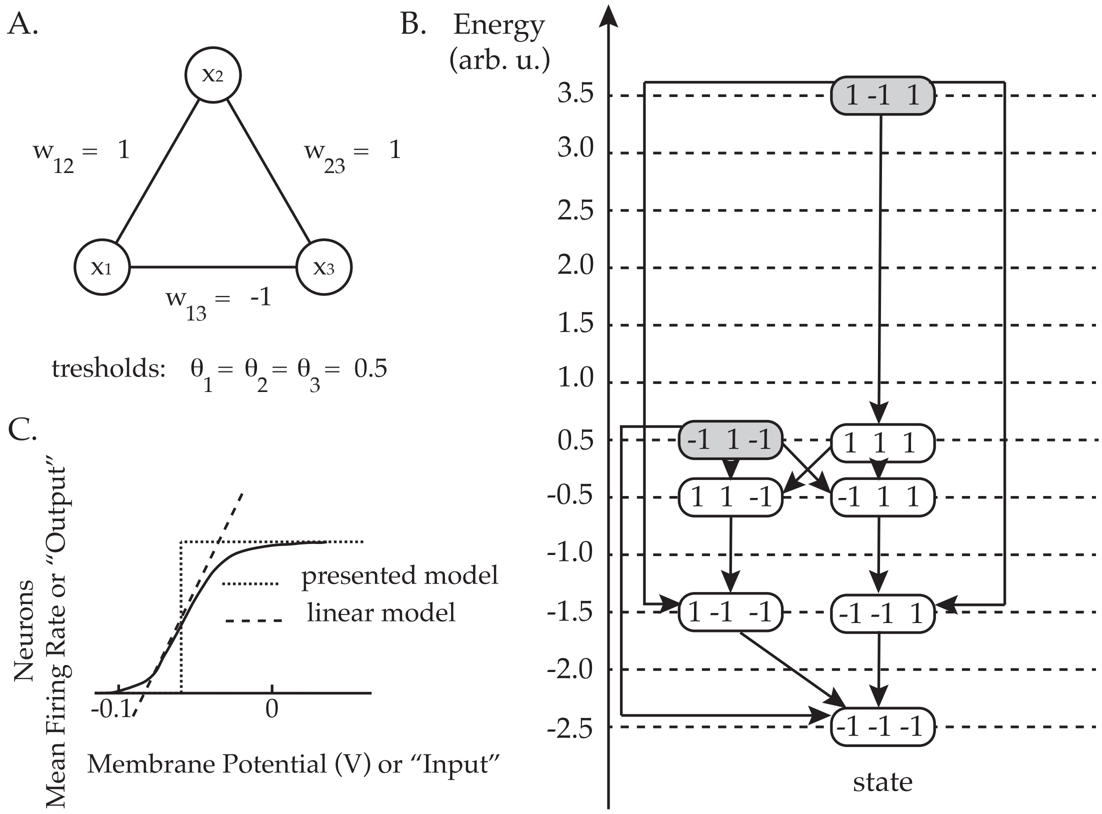

Figure 5.1: **Hopfield network A.** A Hopfield network composed of three units in states x_1, x_2, x_3. The activation treshold is set equal for each unit ($\theta = 0.5$) and the symmetric connections between the units have assigned weights ($w_{12} = w_{21} = 1$, $w_{13} = w_{31} = -1$, $w_{23} = w_{33} = 1$). B. The network in A. can take $2^3 = 8$ states. The energy of each state can be computed according to 5.4 with possible transitions leading to the lowest energy state. The states marked in grey which do not have predecessors are called Garden-of-Eden. Unless they are induced from outside before the simulation starts, they can not be arrived at. C. The solid curve represents input-output relationship between sender neurons and receiver neuron captured by the mean firing rate as a function of membrane voltage for a neuron [166]. The mean rate at which action potentials are created increases smoothly with positive membrane potentials until saturation is reached. No action potentials are generated for large negative membrane potentials thus the firing rate is equal to zero in that region. The two dashed lines represent a simplified way this behaviour can be modelled - as discrete or linear. The former (discrete) model was used in B. Network and energy diagram adapted from [167]

5.2 Our network as a Hopfield Net

A tempting thought experiment imposes itself: could the experimentally obtained network be considered in terms of a Hopfield network? Since it was not possible to retrieve mean firing rates for each neuron in the network correlation coefficients could be used to represent the synaptic connection strengths (Figure 5.2 A.).

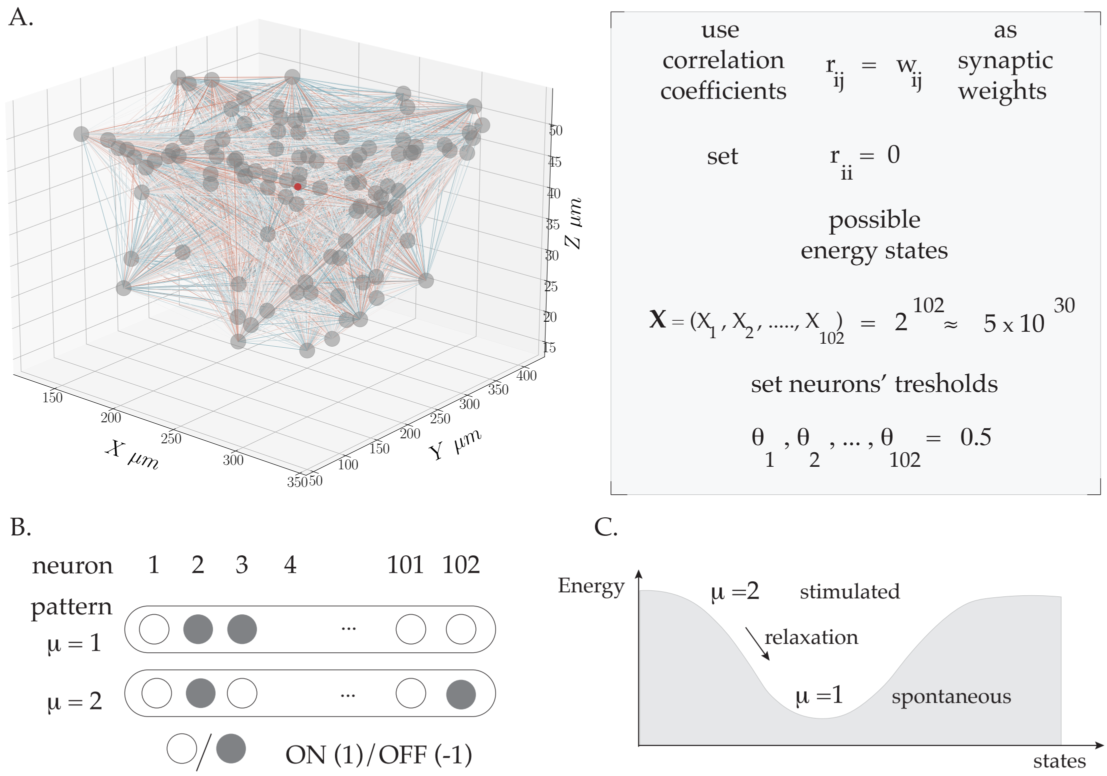

Figure 5.2: **Neural organoid modelled as a Hopfield network A.** An Experimentally obtained network formed in a neural organoid. The network is fully connected and the the strengths of the interactions are given by the correlation coefficients obtained as ... If each node can be either firing or not firing (1 or -1) with a threshold 0.5, the network formed by 102 units can take 2^{102} states. B. Hypothesised situation where the spontaneous activity of the network corresponds to a stable state represented by a pattern $\mu = 1$ which gives the configuration of firing (ON) and non firing (OFF) neurons. Upon maintained stimulation, a new metastable state corresponding to another pattern $\mu = 2$ can emerge. C. When the stimulation is no longer maintained, the network relaxed back to pattern $\mu = 1$ which corresponds to settling into an energy minimum in the energy landscape. Activity pattern representation inspired by [53].

The following scenario could be imagined: the observed spontaneous activity corresponds to a stable state (pattern $\mu = 1$). Upon system stimulation, the system could be induced into another less likely and thus not stable state (pattern $\mu = 2$) which could be maintained during stimulation. However, once the stimulus is removed, the network would relax back to its stable state (Figure 5.2 B. and C.). Or would it not and another state would be created? This could be explored!

Induction of an excited state (new firing pattern) could be achieved by integrating a stimulation agent during functional imaging. For example :
• optical stimulation using another laser source (local) or pattern illumination using a liquid-crystal display (LCD) projector (global)

• electrical: by incorporating electrodes into the sample throughout development

• chemical: exposure a substance that interferes with sample's physiological processes (i.e. diazepam)

In the long run, proper stimulation would allow for controlled activity modulation.

5.2.1 Modifications that could improve future studies

The kinetics of the reporter used in this study makes it suitable to probe slower neuronal communications. To fully resolve individual spikes and subsequently deconvolve the traces to extract firing rates and compute time-lagged cross correlations, the imaging scanning rate in the setup should satisfy the Nyquist criterion for the half-rise-time of the sensor's response. There are two straightforward ways to achieved that.

• The first solution would be to increase z-step between consecutive planes, as a 3 μm step might result in slight oversampling. However, this is acceptable only to the extent where individual neurons can still be segmented in 3D.

• Another solution would be to increase the camera frame rate, which is possible with the camera implemented in the setup. This would require validation if the number of emitted and collected photons with a reduced exposure time per frame (<10 ms) results in a sufficient SNR. A way to mitigate that would be to either increase the laser power intensity or select a brighter reporter. The choice of the imaging parameters is crucial for the viability of the biological sample, especially the laser power intensity used in the experiment. In case of the setup discussed here used laser powers are rather low.)

To improve the understanding of the network dynamics different approaches to obtain the most likely spiking trains that best account for the recorded fluorescence should be explored [123, 168, 169, 170, 171].

• Faster calcium sensors

New generation of calcium indicators with ultra-fast kinetics (rise times, 2 ms) and high brightness has been reported [77]. They could allow for monitoring of activity of neuronal populations on a timescale matching the time scale of AP propagation which is important for neural computation.
Such indicators could be used to map sample's activity at short timescales.

• Voltage indicators

Optical recordings of nerve excitation with the use voltage sensitive organic dyes with fast kinetics were first reported by Tasaki et al. and some years later by Cohen et al. [172, 173]. Changes in membrane potential could be precisely tracked since they induced changes in the fluorescent properties of those cell-membrane bound dyes. A number of genetically encoded voltage indicators (GEVIs) are now available. Still, extraction of circuit-level information from acquired is very challenging since analysis tools are being simultaneously developed [174].

- Scanning mode

In this work, the sample was moved along a static beam to perform volumetric imaging. Such continuous and fast motion might be disadvantageous for some type of samples, for example a zebrafish. A scanning illumination might turn out to be more suitable. In such a scenario, the sample is immobile while being rapidly scanned by a focused light-sheet beam. The image of the illuminated plane is acquired by a camera, usually orthogonally located with respect to the illumination. Yet, high-accuracy synchronization of the co-registration of the focal plane with the light field plane might become challenging.

5.2.2 Healthy sample

It would be important to evaluate how the mycoplasma contamination affected the behaviour of the cell line. Another healthy mouse embryonic stem cell line should be used to generate other datasets. Then the spontaneous behaviour of two generated tissues could be compared. Potentially, there would be major functional differences as in case of kidney cysts by cultured by DesRochers et al. [137].

Chapter 6

Supplements

6.1 2D gaussian fitting

PSF: 3D intensity PSF was obtained by imaging 1% gel-embedded 170 nm fluorescent beads with a 561 nm laser (1% low gelling temperature agarose in ddH¬2O, orange 540/560 nm beads, PS-Speck™ Microscope Point Source Kit P 7220). We cropped ten cuboids with one central bead each. For each bead we then measured 4 lateral and 2 axial intensity profiles along each two perpendicular axes in three central planes (xy, xz, yz) of the bead (Fiji) and further Gaussian-fitted them:

$$y = d + A\,exp(-\frac{(x - x_0)^2}{2\sigma^2}) \tag{6.1}$$

to extract 1/e^2 radii that were assumed to be the lateral and axial resolution. In equation 6.1 d is the offset, A is the amplitude, x_0 is the expected value and σ space the width. We performed this procedure for both 20x and 40x objective. To estimate the light-sheet thickness, height and homogeneity, illumination profiles across 200 x 200 μm^2 of the FOV were mapped. For this purpose, we used a 45deg tilted mirror that was moved along the optical axis to deflect the light-sheet directly into the detection lens. Acquired images were then 2D-gaussian fitted with a custom written Python code to extract σ_x:

$$f(x, y) = d + A\,exp(-(a(x - x_0)^2 + 2b(x - x_0)(y - y_0) + c(y - y_0)^2) \tag{6.2}$$

where

$$\begin{aligned} a &= \frac{\cos^2\theta}{2\sigma_x^2} + \frac{\sin^2\theta}{2\sigma_y^2} \\ b &= -\frac{\sin 2\theta}{4\sigma_x^2} + \frac{\sin 2\theta}{4\sigma_y^2} \\ c &= \frac{\sin^2\theta}{2\sigma_x^2} + \frac{\cos^2\theta}{2\sigma_y^2} \end{aligned} \tag{6.3}$$

by setting the rotation angle to zero ($\theta = 0$) sin terms in a, b, c disappear and we get

$$f(x, y) = d + A\,exp\,(-\frac{(x - x_0)^2}{2\sigma_x^2} + \frac{(y - y_0)^2}{2\sigma_y^2}) \tag{6.4}$$

where d is the offset, A is the amplitude, x_0 is the expected value along x -direction, y_0 is the expected value along y -direction, and σ_x and σ_y are widths along x and y axis respectively. We can then assume the radius of the beam to be σ_x and plot σ_y as a function of z. Data points can be fitted with the theoretical description of a Gaussian beam:

$$w(x) = w_0 + \sqrt{1 + (\frac{x - x_0}{x_R})^2} \tag{6.5}$$

where $2w_0$ is the beam waist and $2x_R$ is the Rayleigh length, x_0 corresponds to the shift with respect to the origin of the coordinate system.

6.2 Experimental and simulated PSF profiles

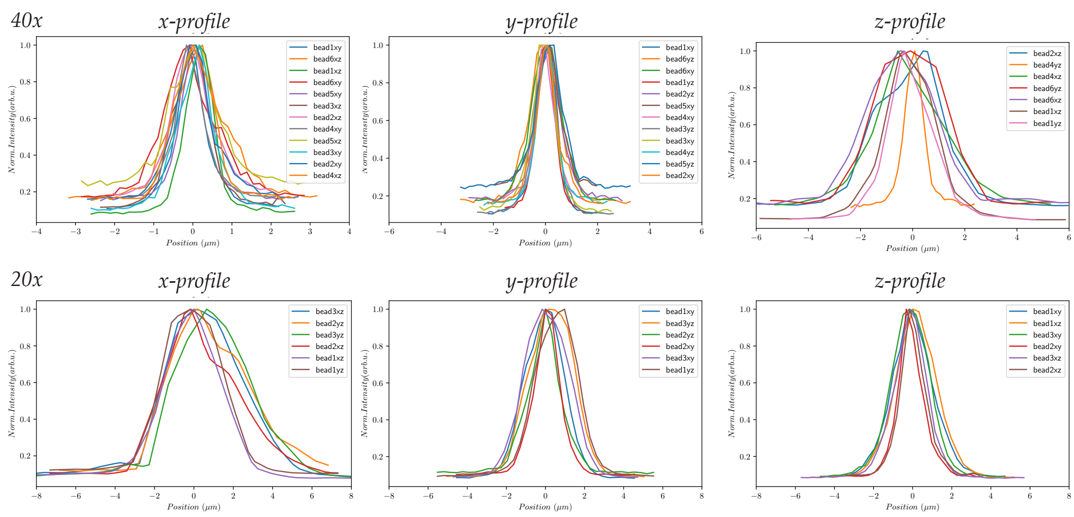

Figure 6.1: **Experimental PSF profiles**

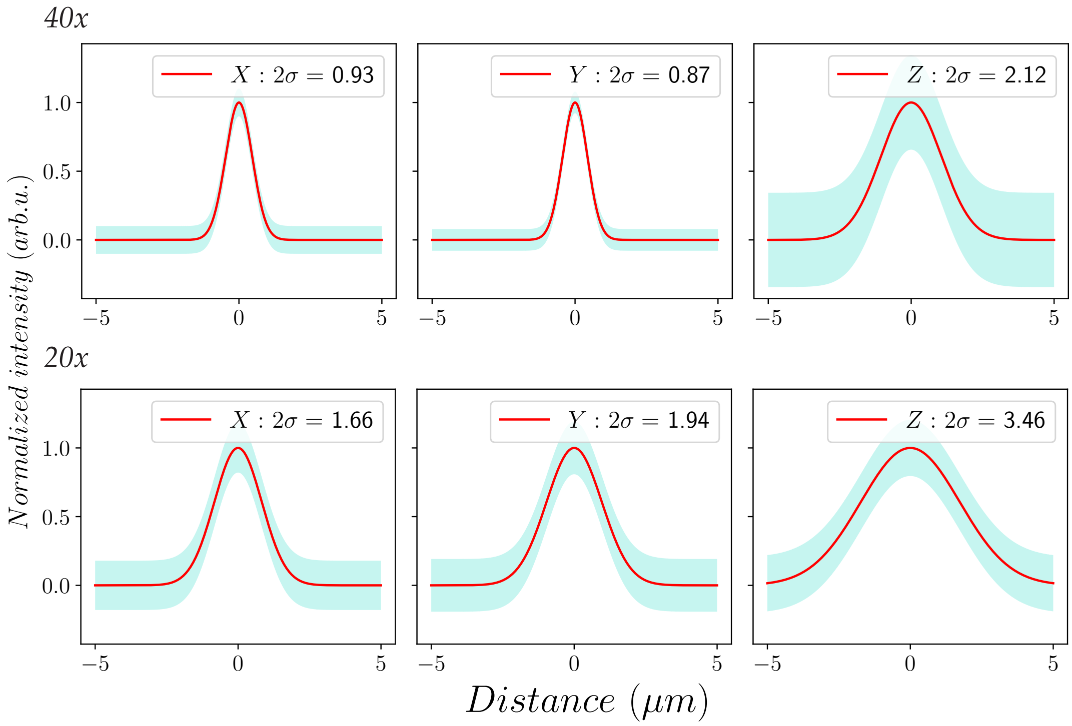

Figure 6.2: **Simulated PSF profiles**

6.3 Dark current measurement

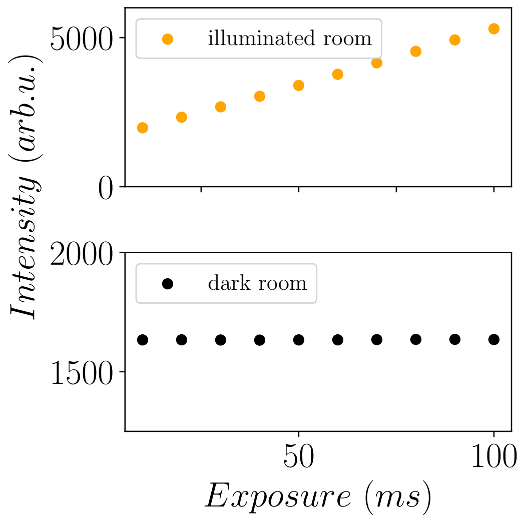

Figure 6.3: **Dark current measurments**

Chapter 7

Closing remarks

"I believe it is impossible to be sure of anything."

— Han Fei Zi

The aim of this project was to study neuronal network activity of a fully developed mouse retinal organoid, a sample that has at that time already been characterized in the lab. To do that, a calcium sensor had to be introduced in the retinal tissue. Several methods have been tried such as viral transduction, plasmid delivery via lipofectamine or electroporation. They did not however yield a suitable sample. Because of that, another strategy has been pursued. It involved the generation of a sample from another cell line, intrinsically expressing sensor molecules.
Creation of a new sample turned out to be very challenging, time consuming and confusing. The induction of neural differentiation of the cell line did not go as expected from the protocol. Back then, the fact that the cell line was contaminated with mycoplasma was not known and has been discovered only after all experiments were performed.
Even though the biological relevance of the obtained results decreases because of the contamination (a soul crushing news indeed), from a physics point of view, the sample served its purpose. The light-sheet setup along with the image analysis pipeline could be validated and are now ready to be used in experiments were a healthy sample will be studied. In addition, the fascinating observation could be made: even though negatively affected (mycoplasma contaminated), embryonic stem cells were able to self-assemble and build a somewhat functioning and organized structure. It is difficult to say if were they not contaminated they would develop into a retina as according to the protocol. It is however a possible hypothesis that could now be tested.

To close the thesis, I decided to cite one of my favourite quotes.

"Simplicity is the ultimate sophistication."

— Leonardo Da Vinci

Bibliography style Reference template
for articles:
Author(s), Title, *Journal*, volume:first page-last page (or article number), year

for books:
Author(s), Title, *Publisher*, chapter:first page-last page, year

Bibliography

[1] Frederico A. C. Azevedo, Ludmila R.B. Carvalho, Lea T. Grinberg, Jose Marcelo Farfel, Renata E.L. Ferretti, Renata Elaine Paraizo Leite, Wilson Jacob Filho, Roberto Lent, and Suzana Herculano-Houzel. Equal numbers of neuronal and nonneuronal cells make the human brain an isometrically scaled-up primate brain. *The Journal of Comparative Neurology*, 513:532–541, 2009.

[2] Christine A. Curcio, Kenneth R. Sloan, Robert E. Kalina, and Anita E. Hendrickson. Human photoreceptor topography. *The Journal of Comparative Neurology*, 292:497–523, 1990.

[3] Madeline A. Lancaster, Magdalena Renner, Carol-Anne Martin, Daniel Wenzel, Louise S. Bicknell, Matthew E. Hurles, Tessa Homfray, Josef M. Penninger, Andrew P. Jackson, and Juergen A. Knoblich. Cerebral organoids model human brain development and microcephaly. *Nature*, 501:373–379, 2013.

[4] Austin P. Passaro and Steven L. Stice. Electrophysiological analysis of brain organoids current approaches and advancements. *Frontiers in Neuroscience*, 14:622137, 2021.

[5] Michelle O'Hara-Wright and Anai Gonzalez-Cordero. Retinal organoids: a window into human retinal development. *Development*, 147:dev189746, 2020.

[6] Stefano L. Giandomenico, Susanna B. Mierau, George M. Gibbons, Léa M. D. Wenger, Laura Masullo, Timothy Sit, Magdalena Sutcliffe, Jérôme Boulanger, Marco Tripodi, Emmanuel Derivery, Ole Paulsen, Andras Lakatos, and Madeline A. Lancaster. Cerebral organoids at the air–liquid interface generate diverse nerve tracts with functional output. *Nature Neuroscience*, 22:669–679, 2019.

[7] Tal Sharf, Tjitse van der Molen, Elmer Guzman, Stella M. K. Glasauer, Gabriel Luna, Zhouwei Cheng, Morgane Audouard, Kamalini G. Ranasinghe, Kiwamu Kudo, Srikantan S. Nagarajan, Kenneth R. Tovar, Linda R. Petzold, Paul K. Hansma, and Kenneth S. Kosik. Intrinsic network activity in human brain organoids. *Biorvix*, https://doi.org/10.1101/2021.01.28.428643, 2021.

[8] Pascal Gervois, Tom Struys, Petra Hilkens, Annelies Bronckaers, Jessica Ratajczak, Constantinus Politis, Bert Brône, Ivo Lambrichts, and Wendy Martens. Neurogenic maturation of human dental pulp stem cells following neurosphere generation induces morphological and electrophysiological characteristics of functional neurons. *Stem Cells and Development*, 24:296–311, 2015.

[9] Amir Minovi, Ainhara Aguado, Daniela Brunert, Stefan Kurtenbach, Stefan Dazert, Hanns Hatt, and Heike Conrad. Isolation, culture optimization and functional characterization of stem cell neurospheres from mouse neonatal olfactory bulb and epithelium. *European Archives of Oto-rhino-laryngology*, 274:3071–3085, 2017.

[10] Bilal Cakir, Yangfei Xiang, Yoshiaki Tanaka, Mehmet H. Kural, Maxime Parent, Young-Jin Kang, Kayley Chapeton, Benjamin Patterson, Yifan Yuan, Chang-Shun He, Micha Sam Brickman Raredon, Jake Dengelegi, Kun-Yong Kim, Pingnan Sun, Mei Zhong, Sangho Lee, Prabir Patra, Fahmeed Hyder, Laura E. Niklason, Sang-Hun Lee, Young sup Yoon, and In-Hyun Park. Engineering of human brain organoids with a functional vascular-like system. *Nature Methods*, 16:1169–1175, 2019.

[11] Rui Li, Le Sun, Ai Fang, Peng Li, Qian Wu, and Xiaoqun Wang. Recapitulating cortical development with organoid culture in vitro and modeling abnormal spindle-like (ASPM related primary) microcephaly disease. *Protein and Cell*, 8:823–833, 2017.

[12] Elizabeth Di Lullo and Arnold R. Kriegstein. The use of brain organoids to investigate neural development and disease. *Nature Reviews Neuroscience*, 18:573–584, 2017.

[13] Sangbae Kim, Albert Lowe, Rachayata Dharmat, Seunghoon Lee, Leah A. Owen, Jun Wang, Akbar Shakoor, Yumei Li, Denise J. Morgan, Andre A. Hejazi, Ales Cvekl, Margaret M. DeAngelis, Z. Jimmy Zhou, Rui Chen, and Wei Liu. Generation, transcriptome profiling, and functional validation of cone-rich human retinal organoids. *Proceedings of the National Academy of Sciences of the United States of America*, 116:10824–10833, 2019.

[14] Jinyan Li, Yijia Chen, Shuai Ouyang, Jingyu Ma, Hui Sun, Lixia Luo, Shuyi Chen, and Yizhi Liu. Generation and staging of human retinal organoids based on self-formed ectodermal autonomous multi-zone system. *Frontiers in Cell and Developmental Biology*, 9:732382, 2021.

[15] Xiufeng Zhong, Christian Gutierrez, Tian Xue, Christopher Hampton, M. Natalia Vergara, Li-Hui Cao, Ann Peters, Tea Soon Park, Elias T. Zambidis, Jason S. Meyer, David M. Gamm, King-Wai Yau, and M. Valeria Canto-Soler. Generation of three-dimensional retinal tissue with functional photoreceptors from human iPSCs. *Nature Communications*, 5:4047, 2014.

[16] Margot Mayer, Onetsine Arrizabalaga, Florian Lieb, Manuel Ciba, Sylvia Ritter, and Christiane Thielemann. Electrophysiological investigation of human embryonic stem cell derived neurospheres using a novel spike detection algorithm. *Biosensors and Bioelectronics*, 100:462–468, 2018.

[17] Christopher L. Frank, Jasmine P. Brown, Kathleen Wallace, William R. Mundy, and Timothy J. Shafer. Developmental neurotoxicants disrupt activity in cortical networks on microelectrode arrays: Results of screening 86 compounds during neural network formation. *Toxicological Sciences*, 160:121–135, 2017.

[18] Ellese Cotterill, Diana Hall, Kathleen Wallace, William R. Mundy, Stephen J. Eglen, and Timothy J. Shafer. Characterization of early cortical neural network development in multiwell microelectrode array plates. *Journal of Biomolecular Screening*, 21:510–519, 2016.

[19] Cleber A. Trujillo, Richard Gao, Priscilla D. Negraes, Jing Gu, Justin Buchanan, Sebastian Preissl, Allen Wang, Wei Wu, Gabriel G. Haddad, Isaac A. Chaim, Alain Domissy, Matthieu Vandenberghe, Anna Devor, Gene W. Yeo, Bradley Voytek, and Alysson R. Muotri. Complex oscillatory waves emerging from cortical organoids model early human brain network development. *Cell Stem Cell*, 25:558–569.e7, 2019.

[20] Timothy J. Shafer, Jasmine P Brown, Brittany Lynch, Sylmarie Davila-Montero, Kathleen Wallace, and Katie Paul Friedman. Evaluation of chemical effects on network formation in cortical neurons grown on microelectrode arrays. *Toxicological Sciences*, 169:436–455, 2019.

[21] Madel Durens, Jonathan E. Nestor, Madeline Williams, Kevin Herold, Robert F. Niescier, Jason W. Lunden, Andre W. Phillips, Yu-Chih Lin, Derek M. Dykxhoorn, and Michael W. Nestor. High-throughput screening of human induced pluripotent stem cell-derived brain organoids. *Journal of Neuroscience Methods*, 335:108627, 2020.

[22] Dean Hallam, Gerrit Hilgen, Birthe Dorgau, Lili Zhu, Min Yu, Sanja Bojic, Philip Hewitt, Michael Schmitt, Marianne Uteng, Stefan Kustermann, David H. W. Steel, Mike Nicholds, Robert J. Thomas, Achim Treumann, Andrew Porter, Evelyne Sernagor, Lyle Armstrong, and Majlinda Lako. Human induced pluripotent stem cells generate light responsive retinal organoids with variable and nutrient dependent efficiency. *Stem Cells*, 36:1535–1551, 2018.

[23] Tim Gollisch and Markus Meister. Eye smarter than scientists believed: Neural computations in circuits of the retina. *Neuron*, 65:150–164, 2010.

[24] Meimanat Fathi, Cody T. Ross, and Zohreh Hosseinzadeh. Functional 3-dimensional retinal organoids: Technological progress and existing challenges. *Frontiers in Neuroscience*, 15:668857, 2021.

[25] Christine Grienberger and Arthur Konnerth. Imaging calcium in neurons. *Neuron*, 73:862–885, 2012.

[26] Cameron S. Cowan, Magdalena Renner, Martina De Gennaro, Brigitte Gross-Scherf, David Goldblum, Yanyan Hou, Martin Munz, Tiago M. Rodrigues, Jacek Krol, Tamas Szikra, Rachel Cuttat, Annick Waldt, Panagiotis Papasaikas, Roland Diggelmann, Claudia P. Patino-Alvarez, Patricia Galliker, Stefan E. Spirig, Dinko Pavlinic, Nadine Gerber-Hollbach, Sven Schuierer, Aldin Srdanovic, Márton Balogh, Marton Balogh, Riccardo Panero, Akos Kusnyerik, Arnold Szabo, Michael B. Stadler, Michael B. Stadler, Selim Orguel, Simone Picelli, Pascal W. Hasler, Andreas Hierlemann, Hendrik P. N. Scholl, Guglielmo Roma, Florian Nigsch, and Botond Roska. Cell types of the human retina and its organoids at single cell resolution. *Cell*, 182:1623–1640.e34, 2020.

[27] Hideya Sakaguchi, Yuki Ozaki, Tomoka Ashida, Takayoshi Matsubara, Naotaka Oishi, Shunsuke Kihara, and Jun Takahashi. Self-organized synchronous calcium transients in a cultured human neural network derived from cerebral organoids. *Stem Cell Reports*, 13:458–473, 2019.

[28] Ranmal A. Samarasinghe, Osvaldo A. Miranda, Jessie E. Buth, Simon Mitchell, Isabella Ferando, Momoko Watanabe, Thomas F. Allison, Arinnae Kurdian, Namie N. Fotion, Michael J. Gandal, Peyman Golshani, Kathrin Plath, William E. Lowry, Jack M. Parent, Istvan Mody, and Bennett G. Novitch. Identification of neural oscillations and epileptiform changes in human brain organoids. *Nature Neuroscience*, 24:1488–1500, 2021.

[29] Sean Quirin, Nikita Vladimirov, Chao-Tsung Yang, Darcy S. Peterka, Rafael Yuste, and Misha B. Ahrens. Calcium imaging of neural circuits with extended depth-of-field light-sheet microscopy. *Optics Letters*, 41:855–858, 2016.

[30] Weijian Zong, Horst A. Obenhaus, Emilie R Skytøen, Hanna Eneqvist, Nienke L. de Jong, M. R. Jorge, May-Britt Moser, and Edvard I. Moser. Large-scale two-photon calcium imaging in freely moving mice. *Cell*, 185:1240–1256.e30, 2021.

[31] Siegfried Weisenburger, Frank Tejera, Jeffrey Demas, Brandon Chen, Brandon Chen, Jason Manley, Fraser T. Sparks, Francisca Martínez Traub, Tanya L. Daigle, Hongkui Zeng, Attila Losonczy, and Alipasha Vaziri. Volumetric Ca^{2+} imaging in the mouse brain using hybrid multiplexed sculpted light microscopy. *Cell*, 177:1050–1066.e14, 2019.

[32] Robert Prevedel, Aart J. Verhoef, Alejandro J Pernía-Andrade, Siegfried Weisenburger, Ben S. Huang, Tobias Nöbauer, Alma Fernández, Jeroen E Delcour, Peyman Golshani, Andrius Baltuška, and Alipasha Vaziri. Fast volumetric calcium imaging across multiple cortical layers using sculpted light. *Nature Methods*, 13:1021–1028, 2016.

[33] Daniil A. Markov, Luigi Petrucco, Andreas M. Kist, and Ruben Portugues. A cerebellar internal model calibrates a feedback controller involved in sensorimotor control. *Nature Communications*, 12:6694, 2021.

[34] Shuting Han, Weijian Yang, and Rafael Yuste. Two-color volumetric imaging of neuronal activity of cortical columns. *Cell Reports*, 27:2229–2240.e4, 2019.

[35] Marco Dal Maschio, Joseph C. Donovan, Thomas O. Helmbrecht, and Herwig Baier. Linking neurons to network function and behavior by two-photon holographic optogenetics and volumetric imaging. *Neuron*, 94:774–789.e5, 2017.

[36] Thomas Panier, Sebastián A. Romano, Raphaël Olive, Thomas Pietri, Germán Sumbre, Raphaël Candelier, and Georges Debrégeas. Fast functional imaging of multiple brain regions in intact zebrafish larvae using selective plane illumination microscopy. *Frontiers in Neural Circuits*, 7:65, 2013.

[37] Nils Wagner, Fynn Beuttenmueller, Nils Norlin, Jakob Gierten, Juan Carlos Boffi, Joachim Wittbrodt, Martin Weigert, Lars Hufnagel, Robert Prevedel,

and Anna Kreshuk. Deep learning-enhanced light-field imaging with continuous validation. *Nature Methods*, 18:557–563, 2021.

[38] Zhenkun Zhang, Lu Bai, Lin Cong, Peng Yu, Tianlei Zhang, Wanzhuo Shi, Funing Li, Jiulin Du, and Kai Wang. Imaging volumetric dynamics at high speed in mouse and zebrafish brain with confocal light field microscopy. *Nature Biotechnology*, 39:74–83, 2020.

[39] Venkatakaushik Voleti, Kripa Patel, Wenze Li, Citlali Perez Campos, Srinidhi Bharadwaj, Hang Yu, Caitlin Ford, Malte Casper, Malte J. Casper, Richard Wenwei Yan, Wenxuan Liang, Chentao Wen, Koutarou D. Kimura, Kimara L. Targoff, and Elizabeth M. C. Hillman. Real-time volumetric microscopy of *in vivo* dynamics and large-scale samples with SCAPE 2.0. *Nature Methods*, 16:1054–1062, 2019.

[40] Nikita Vladimirov, Yu Mu, Takashi Kawashima, Davis V. Bennett, Chao-Tsung Yang, Loren L. Looger, Philipp J. Keller, Jeremy Freeman, and Misha B. Ahrens. Light-sheet functional imaging in fictively behaving zebrafish. *Nature Methods*, 11:883–884, 2014.

[41] Robert Prevedel, Young-Gyu Yoon, Maximilian Hoffmann, Nikita Pak, Gordon Wetzstein, Saul Kato, Tina Schrödel, Ramesh Raskar, Manuel Zimmer, Edward S. Boyden, and Alipasha Vaziri. Simultaneous whole-animal 3D imaging of neuronal activity using light-field microscopy. *Nature Methods*, 11:727–730, 2014.

[42] William C. Lemon, Stefan R. Pulver, Burkhard Höckendorf, Katie McDole, Kristin Branson, Jeremy Freeman, and Philipp J. Keller. Whole-central nervous system functional imaging in larval drosophila. *Nature Communications*, 6:7924, 2015.

[43] Cody J. Greer and Timothy E. Holy. Fast objective coupled planar illumination microscopy. *Nature Communications*, 10:4483, 2019.

[44] Jeffrey Demas, Jason Manley, Frank Tejera, Kevin Barber, Hyewon Kim, Francisca Martínez Traub, Brandon Chen, and Alipasha Vaziri. High-speed, cortex-wide volumetric recording of neuroactivity at cellular resolution using light beads microscopy. *Nature Methods*, 18:1103–1111 , 2021.

[45] Matthew B. Bouchard, Venkatakaushik Voleti, César S. Mendes, Clay O. Lacefield, Wesley B. Grueber, Richard S. Mann, Randy M. Bruno, and Elizabeth M. C. Hillman. Swept confocally-aligned planar excitation (SCAPE) microscopy for high speed volumetric imaging of behaving organisms. *Nature Photonics*, 9:113–119, 2015.

[46] Misha B. Ahrens, Michael B. Orger, Drew N. Robson, Jennifer M. Li, and Philipp J. Keller. Whole-brain functional imaging at cellular resolution using light-sheet microscopy. *Nature Methods*, 10:413–420, 2013.

[47] Lingjie Kong, Jianyong Tang, Justin P. Little, Yang Yu, Tim Lämmermann, Charles P. Lin, Ronald N. Germain, and Meng Cui. Continuous volumetric imaging via an optical phase-locked ultrasound lens. *Nature Methods*, 12:759–762, 2015.

[48] Andrea Giovannucci, Johannes Friedrich, Pat Gunn, Jeremie Kalfon, Brandon L Brown, Sue Ann Koay, Jiannis Taxidis, Farzaneh Najafi, Jeffrey L. Gauthier, Pengcheng Zhou, Baljit S. Khakh, David W. Tank, Dmitri B. Chklovskii, and Eftychios A. Pnevmatikakis. Caiman an open source tool for scalable calcium imaging data analysis. *eLife*, 8:e38173, 2019.

[49] W. Waldeyer. Über einige neuere forschungen im gebiete der anatomie des centralnervensystems (fortsetzung aus no. 45.). *Deutsche Medizinische Wochenschrift*, 17:1244–1246, 1891.

[50] Walther Nernst. Die elektromotorische wirksamkeit der jonen. *Zeitschrift für Physikalische Chemie*, 4:129–181, 1889.

[51] David E. Goldman. Potential, impedance, and rectification in membranes. *The Journal of General Physiology*, 27:37–60, 1943.

[52] Alan Hodgkin and Bernard Katz. The effect of sodium ions on the electrical activity of the giant axon of the squid. *The Journal of Physiology*, 108:37–77, 1949.

[53] Wulfram Gerstner, Werner M. Kistler, Richard Naud, and Liam Paninski. Neuronal dynamics: From single neurons to networks and models of cognition. *Cambridge University Press*, 2014.

[54] John D. Robertson. Membrane structure. *The Journal of Cell Biology*, 91:189s–204s, 1981.

[55] Stephen H. Wright. Generation of resting membrane potential. *Advances in Physiology Education*, 28:139–142, 2004.

[56] Peter Dayan and L. F. Abbott. Theoretical neuroscience: Computational and mathematical modeling of neural systems. *The MIT Press*, 6:220–224, 2001.

[57] Dale Purves and Stephen M. Williams. Neuroscience. 3rd edition. *Sinauer Associates*, 2-3:31–91, 2004.

[58] John W. Griffin and Wesley J. Thompson. Biology and pathology of non-myelinating schwann cells. *Glia*, 56:1518–1531, 2008.

[59] Alan Hodgkin and Andrew Huxley. A quantitative description of membrane current and its application to conduction and excitation in nerve. *The Journal of Physiology*, 117:500–544, 1952.

[60] John Z. Young. The functioning of the giant nerve fibres of the squid. *The Journal of Experimental Biology*, 15:170–185, 1938.

[61] George Marmont. Studies on the axon membrane. i. a new method. *Journal of Cellular and Comparative Physiology*, 34:351–382, 1949.

[62] Liqun Luo. Principles of neurobiology. *Garland Science, Taylor & Francis Group*, 2:50,53, 2001.

[63] Janusz E. Jacak and Witold A. Jacak. New wave-type mechanism of saltatory conduction in myelinated axons and micro-saltatory conduction in C fibres. *European Biophysics Journal*, 49:343–360, 2020.

[64] Witold Jacak. Quantum nano-plasmonics. *Cambridge University Press*, 2020.

[65] Tetsuya Akaishi. Saltatory conduction as an electrostatic compressional wave in the axoplasm. *Tohoku Journal of Experimental Medicine*, 244:151–161, 2018.

[66] Alison M. Harman and S.R. Moore. Number of neurons in the retinal ganglion cell layer of the quokka wallaby do not change throughout life. *Anatomical Record-advances in Integrative Anatomy and Evolutionary Biology*, 256:78–83, 1999.

[67] Martin J. Evans, Mathew J. Evans, and Matthew H. Kaufman. Establishment in culture of pluripotential cells from mouse embryos. *Nature*, 292:154–156, 1981.

[68] Gail R. Martin. Isolation of a pluripotent cell line from early mouse embryos cultured in medium conditioned by teratocarcinoma stem cells. *Proceedings of the National Academy of Sciences of the United States of America*, 8:7634–7638, 1981.

[69] Rudolf Jaenisch and Richard A. Young. Stem cells, the molecular circuitry of pluripotency and nuclear reprogramming. *Cell*, 132:567–582, 2008.

[70] Waseem K. Raja, Alison E. Mungenast, Yuan-Ta Lin, Tak Ko, Fatema Abdurrob, Jinsoo Seo, and Li-Huei Tsai. Self-organizing 3D human neural tissue derived from induced pluripotent stem cells recapitulate Alzheimer's disease phenotypes. *PLOS One*, 11:e0161969, 2016.

[71] Juan Yin and Antonius M. J. VanDongen. Enhanced neuronal activity and asynchronous calcium transients revealed in a 3D organoid model of Alzheimer's disease. *ACS Biomaterials Science & Engineering*, 7:254–264, 2020.

[72] Mototsugu Eiraku, Nozomu Takata, Hiroki Ishibashi, Masako Kawada, Eriko Sakakura, Satoru Okuda, Kiyotoshi Sekiguchi, Taiji Adachi, and Yoshiki Sasai. Self-organizing optic-cup morphogenesis in three-dimensional culture. *Nature*, 472:51–56, 2011.

[73] Manuela Völkner, Marlen Zschätzsch, Mariya Rostovskaya, Rupert W. Overall, Volker Busskamp, Konstantinos Anastassiadis, and Mike O. Karl. Retinal organoids from pluripotent stem cells efficiently recapitulate retinogenesis. *Stem Cell Reports*, 6:525–538, 2016.

[74] Manuela Völkner, Thomas Kurth, Jana Schor, Lynn J. A. Ebner, Lara Bardtke, Cagri Kavak, Joerg Hackermueller, and Mike O. Karl. Mouse retinal organoid growth and maintenance in longer-term culture. *Frontiers in Cell and Developmental Biology*, 9:645704, 2021.

[75] C. J. van Oss, R.J Good, and Manoj K. Chaudhury. Nature of the antigen-antibody interaction. primary and secondary bonds: optimal conditions for association and dissociation. *Journal of Chromatography B: Biomedical Sciences and Applications*, 376:111–9, 1986.

[76] Sung-Yon Kim, Jae Hun Cho, Evan Murray, Naveed A. Bakh, Heejin Choi, Kimberly Ohn, Luzdary Ruelas, Austin Hubbert, Meg McCue, Sara Vassallo, Philipp J. Keller, and Kwanghun Chung. Stochastic electrotransport selectively enhances the transport of highly electromobile molecules. *Proceedings of the National Academy of Sciences of the United States of America*, 112:E6274–83, 2015.

[77] Yan Zhang, Marton Rozsa, Yajie Liang, Daniel Bushey, Ziqiang Wei, Jihong Zheng, Daniel Reep, Gerard Joey Broussard, Arthur Tsang, Getahun Tsegaye, Sujatha Narayan, Christopher J. Obara, Jing-Xuan Lim, Ronak Patel, Rongwei Zhang, Misha B. Ahrens, Glenn C. Turner, Samuel S.H. Wang, Wyatt L. Korff, Eric R. Schreiter, Karel Svoboda, Jeremy P. Hasseman, Ilya Kolb, and Loren L. Looger. Fast and sensitive GCaMP calcium indicators for imaging neural populations. *Biorvix*, doi:10.1101/2021.11.08.467793, 2021.

[78] Guosong Hong and Charles M. Lieber. Novel electrode technologies for neural recordings. *Nature Reviews Neuroscience*, 20:330–345, 2019.

[79] Kazi Tasnim and Jia Liu. Emerging bioelectronics for brain organoid electrophysiology. *Journal of Molecular Biology*, 434:167165, 2021.

[80] Hyogeun Shin, Sohyeon Jeong, Ju Hyun Lee, Woong Sun, Nakwon Choi, and Il-Joo Cho. 3D high-density microelectrode array with optical stimulation and drug delivery for investigating neural circuit dynamics. *Nature Communications*, 12:1–18, 2021.

[81] Qiang Li, Kewang Nan, Paul Le Floch, Zuwan Lin, Hao Sheng, Thomas S. Blum, and Jia Liu. Cyborg organoids: Implantation of nanoelectronics via organogenesis for tissue-wide electrophysiology. *Nano Letters*, 19:5781–5789, 2019.

[82] Jan Mueller, Marco Ballini, Paolo Livi, Yihui Chen, Milos Radivojevic, Amir Shadmani, Vijay Viswam, Ian L. Jones, Michele Fiscella, Roland Diggelmann, Alexander Stettler, Urs Frey, Douglas J. Bakkum, and Andreas Hierlemann. High-resolution CMOS MEA platform to study neurons at subcellular, cellular, and network levels. *Lab on a Chip*, 15:2767–2780, 2015.

[83] Areles Molleman. Patch clamping : an introductory guide to patch clamp electrophysiology. *Wiley*, 2:33–42, 2002.

[84] Anca M. Paşca, Steven A. Sloan, Laura E. Clarke, Yuan Tian, Christopher D. Makinson, Nina Huber, Chul Hoon Kim, Jin-Young Park, Nancy A. O'Rourke, Khoa D. Nguyen, Stephen J. Smith, John R. Huguenard, Daniel H. Geschwind, Ben A. Barres, and Sergiu P. Paşca. Functional cortical neurons and astrocytes from human pluripotent stem cells in 3D culture. *Nature Methods*, 12:671–678, 2015.

[85] Micha E. Spira and Aviad Hai. Multi-electrode array technologies for neuroscience and cardiology. *Nature Nanotechnology*, 8:83–94, 2013.

[86] James J. Jun, Nicholas A. Steinmetz, Joshua H. Siegle, Daniel J. Denman, Marius Bauza, Brian Barbarits, Albert K. Lee, Costas A. Anastassiou, Alexandru Andrei, Çağatay Aydın, Mladen Barbic, Timothy J. Blanche, Vincent Bonin, João Luiz Peçanha Couto, Barundeb Dutta, Sergey L. Gratiy, Diego A. Gutnisky, Michael Häusser, Bill Karsh, Peter Ledochowitsch, Carolina Mora Lopez, Catalin Mitelut, Silke Musa, Michael S. Okun, Marius Pachitariu, Jan Putzeys, P. Dylan Rich, Cyrille Rossant, Wei lung Sun, Karel Svoboda, Matteo Carandini, Kenneth D. Harris, Christof Koch, John O'Keefe, and Timothy D. Harris. Fully integrated silicon probes for high-density recording of neural activity. *Nature*, 551:232–236, 2017.

[87] Paul Le Floch, Qiang Li, Zuwan Lin, Siyuan Zhao, Ren Liu, Kazi Tasnim, Han Jiang, and Jia Liu. Stretchable mesh nanoelectronics for three-dimensional single-cell chronic electrophysiology from developing brain organoids. *Advanced materials*, 34:e2106829, 2022.

[88] Kun Ping Lu and Anthony R. Means. Regulation of the cell cycle by Calcium and Calmodulin. *Endocrine Reviews*, 14:40–58, 1993.

[89] Sten Orrenius, Boris Zhivotovsky, and Pierluigi Nicotera. Regulation of cell death the calcium-apoptosis link. *Nature Reviews Molecular Cell Biology*, 4:552–565, 2003.

[90] Robert S. Zucker. Calcium- and activity-dependent synaptic plasticity. *Current Opinion in Neurobiology*, 9:305–13, 1999.

[91] Claire Ribrault, Ken Sekimoto, and Antoine Triller. From the stochasticity of molecular processes to the variability of synaptic transmission. *Nature Reviews Neuroscience*, 12:375–387, 2011.

[92] Christopher D. Moyes and Patricia M. Schulte. Animal physiology, 3rd edition. *Pearson*, 5:154–179, 2016.

[93] Erwin Neher and Takeshi Sakaba. Multiple roles of calcium ions in the regulation of neurotransmitter release. *Neuron*, 59:861–72, 2008.

[94] Yongkiel Sung and Seong Kim. Recent advances in the development of gene delivery systems. *Biomaterials Research*, 23:1–7, 2019.

[95] Fernando P. Polack, Kenneth Koury, Stephen J. Thomas, Nicholas Kitchin, Judith Absalon, Alejandra Gurtman, Stephen Lockhart, John L. Perez, Gonzalo Pérez Marc, Edson D. Moreira, Cristiano Zerbini, Ruth Bailey, Kena A. Swanson, Satrajit Roychoudhury, Kenneth Koury, Ping Li, Warren Kalina, David K. C. Cooper, Robert W. Frenck, Laura L Hammitt, Özlem Türeci, Haylene Nell, Axel Schaefer, Serhat Ünal, Dina B Tresnan, Susan Mather, Philip R. Dormitzer, Uğur Şahin, Kathrin U. Jansen, and William C. Gruber. Safety and efficacy of the BNT162b2 mRNA Covid-19 vaccine. *The New England Journal of Medicine*, 383:2603–2615, 2020.

[96] Marco Mank and Oliver Griesbeck. Genetically encoded calcium indicators. *Chemical Reviews*, 198:1550–1564, 2008.

[97] Nathan C. Shaner, Michael Z. Lin, Michael R. McKeown, Paul Steinbach, Kristin L. Hazelwood, Michael W. Davidson, and Roger Y. Tsien. Improving the photostability of bright monomeric orange and red fluorescent proteins. *Nature Methods*, 5:545–551, 2008.

[98] Fritjof Helmchen. Handbook of neural activity measurement: Calcium imaging. *Cambridge University Press*, 12:362–403, 2012.

[99] Yongxin Zhao, Satoko Araki, Jiahui Wu, Takayuki Teramoto, Yu Fen Chang, Masahiro Nakano, Ahmed S. Abdelfattah, Manabi Fujiwara, Takeshi Ishihara, Takeharu Nagai, and Robert E. Campbell. An expanded palette of genetically encoded Ca^{2+} indicators. *Science*, 333:1888–1891, 2011.

[100] Weijian Yang and Rafael Yuste. *In vivo* imaging of neural activity. *Nature Methods*, 14:349–359, 2017.

[101] Jerome Mertz. Strategies for volumetric imaging with a fluorescence microscope. *Optica*, 6:1261–1268, 2019.

[102] Rongwen Lu, Wenzhi Sun, Yajie Liang, Aaron M. Kerlin, Jens Bierfeld, Johannes Dominik Seelig, Daniel E. Wilson, Benjamin Scholl, Boaz Mohar, Masashi Tanimoto, Minoru Koyama, David Fitzpatrick, Michael B. Orger, and Na Ji. Video-rate volumetric functional imaging of the brain at synaptic resolution. *Nature Neuroscience*, 20:620–628, 2017.

[103] Rongwen Lu, Masashi Tanimoto, Minoru Koyama, and Na Ji. 50 Hz volumetric functional imaging with continuously adjustable depth of focus. *Biomedical Optics Express*, 9:1964–1976, 2018.

[104] Sheng Xiao, Hua an Tseng, Howard J. Gritton, Xue Han, and Jerome Mertz. Video-rate volumetric neuronal imaging using 3D targeted illumination. *Scientific Reports*, 8:7921, 2018.

[105] Pablo Loza-Alvarez, Gustavo Castro-Olvera, Jorge Madrid-Wolff, Omar E. Olarte, Emilio J. Gualda, Jordi Soriano, Estefanía Estévez-Priego, and Adriaan A. Ludl. Light sheet fluorescence microscopy for 3D imaging of Ca^{2+} dynamics in neuronal cultures. *Proceedings SPIE, Emerging Topics in Artificial Intelligence (ETAI) 2021*, 118040L, 2021.

[106] Bin Yang, Merlin Lange, Alfred Millett-Sikking, Xiang Zhao, Jordão Bragantini, Shruthi VijayKumar, Mason Kamb, Rafael Gomez-Sjoberg, AhmetCan Solak, Wanpeng Wang, Hirofumi Kobayashi, Matthew N McCarroll, Lachlan Whitehead, Reto P Fiolka, Thomas B Kornberg, Andrew G York, and Loic Royer. DaXi-high-resolution, large imaging volume and multi-view single-objective light-sheet microscopy. *Nature Methods*, 19:461–469, 2022.

[107] H. Siedentopf and R. Zsigmondy. Über sichtbarmachung und größenbestimmung ultramikoskopischer teilchen, mit besonderer anwendung auf goldrubingläser. *Annalen der Physik*, 315:1–39, 1902.

[108] A.H. Voie, D. H. Burns, and Francis A. Spelman. Orthogonal-plane fluorescence optical sectioning: Three-dimensional imaging of macroscopic biological specimens. *Journal of Microscopy*, 170:229–236, 1993.

[109] Jan Huisken, Jim Swoger, Filippo Del Bene, Joachim Wittbrodt, and Ernst H. K. Stelzer. Optical sectioning deep inside live embryos by selective plane illumination microscopy. *Science*, 305:1007–1009, 2004.

[110] Joseph T. Verdeyen. Laser electronics, 3rd edition. *Pearson*, 3:63–72, 1995.

[111] Ernst H. K. Stelzer, Frederic Strobl, Bo-Jui Chang, Friedrich Preusser, Stephan Preibisch, Katie McDole, and Reto Fiolka. Light sheet fluorescence microscopy. *Nature Reviews Methods Primers*, 1:73, 2021.

[112] Stephan W. Grill and Ernst H. K. Stelzer. Method to calculate lateral and axial gain factors of optical setups with a large solid angle. *Journal of The Optical Society of America A-optics Image Science and Vision*, 16:2658–2665, 1999.

[113] Ernst H. K. Stelzer and Stephan W. Grill. The uncertainty principle applied to estimate focal spot dimensions. *Optics Communications*, 173:51–56, 2000.

[114] Patrick Kaifosh, Jeffrey D. Zaremba, Nathan B. Danielson, and Attila Losonczy. SIMA: Python software for analysis of dynamic fluorescence imaging data. *Frontiers in Neuroinformatics*, 8:80, 2014.

[115] Pengcheng Zhou, Shanna L. Resendez, Jose Rodriguez-Romaguera, Jessica C. Jimenez, Shay Q. Neufeld, Garret D. Stuber, René Hen, Mazen A. Kheirbek, Bernardo L. Sabatini, Robert E. Kass, and Liam Paninski. Efficient and accurate extraction of *in vivo* calcium signals from microendoscopic video data. *eLife*, 7:e28728, 2016.

[116] Marius Pachitariu, Carsen Stringer, Sylvia Schröder, Mario Dipoppa, L. Federico Rossi, Matteo Carandini, and Kenneth D. Harris. Suite2p: beyond 10,000 neurons with standard two-photon microscopy. *BioRxiv*, doi:10.1101/061507, 2016.

[117] Stephanie Reynolds, Therese Abrahamsson, Renaud Schuck, P. Jesper Sjöström, Simon R. Schultz, and Pier Luigi Dragotti. ABLE: An activity-based level set segmentation algorithm for two-photon calcium imaging data. *eNeuro*, 4:ENEURO.0012–17.2017, 2017.

[118] Ashley Petersen, Noah Simon, and Daniela Witten. SCALPEL: Extracting neurons from calcium imaging data. *The Annals of Applied Statistics*, 12:2430–2456, 2018.

[119] Jinghao Lu, Chunyuan Li, Jonnathan Singh-Alvarado, Zhe Charles Zhou, Flavio Fröhlich, Richard Mooney, and Fan Wang. MIN1PIPE: A miniscope 1-photon-based calcium imaging signal extraction pipeline. *Cell Reports*, 23:3673–3684, 2018.

[120] Martin Rückl, Stephen C. Lenzi, Laura Moreno-Velasquez, Daniel Parthier, Dietmar Schmitz, Sten Rüdiger, and Friedrich W. Johenning. SamuROI, a python-based software tool for visualization and analysis of dynamic time series imaging at multiple spatial scales. *Frontiers in Neuroinformatics*, 11:44, 2017.

[121] Pentti Paatero and Unto Tapper. Analysis of different modes of factor analysis as least squares fit problems. *Chemometrics and Intelligent Laboratory Systems*, 18:183–194, 1993.

[122] Daniel D. Lee and H. Sebastian Seung. Learning the parts of objects by non-negative matrix factorization. *Nature*, 401:788–91, 1999.

[123] Eftychios A. Pnevmatikakis, Daniel Soudry, Yuanjun Gao, Timothy A. Machado, Josh Merel, David Pfau, Thomas Reardon, Yu Mu, Clay O. Lacefield, Weijian Yang, Misha B. Ahrens, Randy M. Bruno, Thomas M. Jessell, Darcy S. Peterka, Rafael Yuste, and Liam Paninski. Simultaneous denoising, deconvolution, and demixing of calcium imaging data. *Neuron*, pages 285–299, 2016.

[124] Maria Göppert-Mayer. Über elementarakte mit zwei quantensprüngen. *Annalen der Physik*, 401:273–294, 1931.

[125] Eftychios A. Pnevmatikakis and Andrea Giovannucci. NoRMCorre: An online algorithm for piecewise rigid motion correction of calcium imaging data. *Journal of Neuroscience Methods*, 291:83–94, 2017.

[126] Rodolfo R. Llinas. The intrinsic electrophysiological properties of mammalian neurons: insights into central nervous system function. *Science*, 242:1654–1664, 1988.

[127] Pietro Ricci, Vladislav Gavryusev, Caroline Muellenbroich, Lapo Turrini, Giuseppe de Vito, Ludovico Silvestri, Giuseppe Sancataldo, and Francesco S. Pavone. Removing striping artifacts in light-sheet fluorescence microscopy: a review. *Progress in Biophysics and Molecular Biology*, 168:52–65, 2021.

[128] Stuart Berg, Dominik Kutra, Thorben Kroeger, Christoph N. Straehle, Bernhard X. Kausler, Carsten Haubold, Martin Schiegg, Janez Ales, Thorsten Beier, Markus Rudy, Kemal Eren, Jaime I Cervantes, Buote Xu, Fynn Beuttenmueller, Adrian Wolny, Chong Zhang, Ullrich Koethe, Fred A. Hamprecht, and Anna Kreshuk. Ilastik: interactive machine learning for (bio)image analysis. *Nature Methods*, 16:1226–1232, 2019.

[129] Ilaria Chiaradia and Madeline A. Lancaster. Brain organoids for the study of human neurobiology at the interface of in vitro and *in vivo*. *Nature Neuroscience*, 23:1496–1508, 2020.

[130] Hans R. Schöler, Siegfried Ruppert, N. Suzuki, Kamal Chowdhury, and Peter Gruss. New type of pou domain in germ line-specific protein Oct-4. *Nature*, 344:435–439, 1990.

[131] Jennifer Nichols, Branko Zevnik, Konstantinos Anastassiadis, Hitoshi Niwa, Daniela Klewe-Nebenius, Ian Chambers, Hans R. Schöler, and Austin Smith. Formation of pluripotent stem cells in the mammalian embryo depends on the pou transcription factor Oct4. *Cell*, 95:379–91, 1998.

[132] Hitoshi Niwa, Jun ichi Miyazaki, and Austin Smith. Quantitative expression of Oct-3/4 defines differentiation, dedifferentiation or self-renewal of ES cells. *Nature Genetics*, 24:372–376, 2000.

[133] Ian Chambers, Douglas Colby, Morag Robertson, Jennifer Nichols, Sonia Lee, Susan Tweedie, and Austin Smith. Functional expression cloning of Nanog, a pluripotency sustaining factor in embryonic stem cells. *Cell*, 113:643–655, 2003.

[134] Kaoru Mitsui, Yoshimi Tokuzawa, Hiroaki Itoh, Kohichi Segawa, Mirei Murakami, Kazutoshi Takahashi, Masayoshi Maruyama, Mitsuyo Maeda, and Shinya Yamanaka. The homeoprotein Nanog is required for maintenance of pluripotency in mouse epiblast and ES cells. *Cell*, 113:631–642, 2003.

[135] Hans G. Drexler and Cord C. Uphoff. *Mycoplasma* contamination of cell cultures: Incidence, sources, effects, detection, elimination, prevention. *Cytotechnology*, 39:75–90, 2002.

[136] Laleh Nikfarjam and Parvaneh Farzaneh. Prevention and detection of Mycoplasma contamination in cell culture. *Cell*, 13:203–12, 2012.

[137] Teresa M. DesRochers, Ivana Y. Kuo, Erica P. Kimmerling, Barbara E. Ehrlich, and David L. Kaplan. The effects of *Mycoplasma* contamination upon the ability to form bioengineered 3D kidney cysts. *PLOS One*, 10:e0120097, 2015.

[138] Hod Dana, Boaz Mohar, Yi Sun, Sujatha Narayan, Andrew Gordus, Jeremy P Hasseman, Getahun Tsegaye, Graham T Holt, Amy Hu, Deepika Walpita, Ronak Patel, John J. Macklin, Cornelia I. Bargmann, Misha B. Ahrens, Eric R. Schreiter, Vivek Jayaraman, Loren L. Looger, Karel Svoboda, and Douglas S. Kim. Sensitive red protein calcium indicators for imaging neural activity. *eLife*, 5:e12727, 2016.

[139] Jonas Dahlstrand, Michael Lardelli, and Urban Lendahl. Nestin mRna expression correlates with the central nervous system progenitor cell state in many, but not all, regions of developing central nervous system. *Developmental Brain Research*, 84:109–129, 1995.

[140] Urban Lendahl, Lyle B. Zimmerman, and Ronald D.G. McKay. CNS stem cells express a new class of intermediate filament protein. *Cell*, 60:585–595, 1990.

[141] Mahmud Bani-Yaghoub, Roger Tremblay, Joy X Lei, Dongling Zhang, Bogdan Zurakowski, Jagdeep K. Sandhu, Brandon Smith, Maria Ribecco-Lutkiewicz, Jessica Kennedy, P. Roy Walker, and Marianna Sikorska. Role of Sox2 in the development of the mouse neocortex. *Developmental Biology*, 295:52–66, 2006.

[142] Stephen N. Sansom, Dean S. Griffiths, Andrea Faedo, Dirk-Jan Kleinjan, Youlin Ruan, James C. Smith, Veronica van Heyningen, John L.R. Rubenstein, and Frederick J. Livesey. The level of the transcription factor pax6 is essential for controlling the balance between neural stem cell self-renewal and neurogenesis. *PLOS Genetics*, 5:e1000511, 2009.

[143] Jasper Akerboom, Nicole Carreras Calderón, Lin Tian, Sebastian Wabnig, Matthias Prigge, Johan Tolö, Andrew Gordus, Michael B. Orger, Kristen E. Severi, John J. Macklin, Ronak Patel, Stefan R. Pulver, Trevor J. Wardill, Elisabeth Fischer, Christina Schueler, Tsai-Wen Chen, Karen S. Sarkisyan, Jonathan S. Marvin, Cornelia I. Bargmann, Douglas S. Kim, Sebastian Kuegler, Leon Lagnado, Peter Hegemann, Alexander Gottschalk, Eric R. Schreiter, and Loren L. Looger. Genetically encoded calcium indicators for multicolor neural activity imaging and combination with optogenetics. *Frontiers in Molecular Neuroscience*, 6:2, 2013.

[144] D. O. Hebb. The organization of behavior: A neuropsychological theory. *John Wiley & Sons. Inc., New York*, 1949.

[145] Guo-Qiang Bi and Mu ming Poo. Synaptic modification by correlated activity: Hebb's postulate revisited. *Annual Review of Neuroscience*, 24:139–166, 2001.

[146] Elad Schneidman, Michael J. Berry, Ronen Segev, and William Bialek. Weak pairwise correlations imply strongly correlated network states in a neural population. *Nature*, 440:1007–12, 2006.

[147] Rachel O. L. Wong, Markus Meister, and Carla J. Shatz. Transient period of correlated bursting activity during development of the mammalian retina. *Neuron*, 11:923–38, 1993.

[148] Catherine S. Cutts and Stephen J. Eglen. Detecting pairwise correlations in spike trains: An objective comparison of methods and application to the study of retinal waves. *The Journal of Neuroscience*, 34:14288–303, 2014.

[149] Kevin L. Briggman and Winfried Denk. Towards neural circuit reconstruction with volume electron microscopy techniques. *Current Opinion in Neurobiology*, 16:562–570, 2006.

[150] Deepak Ropireddy and Giorgio A. Ascoli. Potential synaptic connectivity of different neurons onto pyramidal cells in a 3D reconstruction of the rat hippocampus. *Frontiers in Neuroinformatics*, 5:5, 2011.

[151] Carsen Stringer, Timothy C. Wang, Michalis Michaelos, and Marius Pachitariu. Cellpose: a generalist algorithm for cellular segmentation. *Nature Methods*, 18:100–106, 2020.

[152] Rafael Yuste, Darin A. Nelson, William W. Rubin, and Lawrence C. Katz. Neuronal domains in developing neocortex: Mechanisms of coactivation. *Neuron*, 14:7–17, 1995.

[153] Rachel O.L. Wong. The role of firing patterns in neuronal development of sensory systems. *Current Opinion in Neurobiology*, 3:595–601, 1993.

[154] Michael J. O'Donovan, Stephen M. Ho, Gerald Sholomenko, and Wayne Yee. Real-time imaging of neurons retrogradely and anterogradely labelled with calcium-sensitive dyes. *Journal of Neuroscience Methods*, 46:91–106, 1993.

[155] Corey S. Goodman and Carla J. Shatz. Developmental mechanisms that generate precise patterns of neuronal connectivity. *Cell*, 72:77–98, 1993.

[156] Markus Meister, Rachel O.L. Wong, Denis A. Baylor, and Carla J. Shatz. Synchronous bursts of action potentials in ganglion cells of the developing mammalian retina. *Science*, 252:939–943, 1991.

[157] Lamberto Maffei and L Galli-Resta. Correlation in the discharges of neighboring rat retinal ganglion cells during prenatal life. *Proceedings of the National Academy of Sciences of the United States of America*, 87:2861–2864, 1990.

[158] J. S. Tootle. Early postnatal development of visual function in ganglion cells of the cat retina. *Journal of Neurophysiology*, 69:1645–1660, 1993.

[159] Fabrizio De Vico Fallani, Jonas Richiardi, Mario Chavez, and Sophie Achard. Graph analysis of functional brain networks: practical issues in translational neuroscience. *Philosophical Transactions of the Royal Society B*, 369:20130521, 2014.

[160] Olaf Sporns. Structure and function of complex brain networks. *Dialogues in clinical neuroscience*, 15:247–262, 2013.

[161] Francisco J. Varela, Jean-Philippe Lachaux, Eugenio Rodriguez, and Jacques Martinerie. The brainweb: phase synchronization and large-scale integration. *Nature Reviews Neuroscience*, 2:229–239, 2001.

[162] John G. White, Eileen Southgate, J. N. Thomson, and Sydney Brenner. The structure of the nervous system of the nematode *Caenorhabditis elegans*. *Philosophical Transactions of the Royal Society B*, 314:1–340, 1986.

[163] Duncan J. Watts and Steven H. Strogatz. Collective dynamics of small-world networks. *Nature*, 393:440–442, 1998.

[164] Jianwei Shuai and Dominique M. Durand. Phase synchronization in two coupled chaotic neurons. *Physics Letters A*, 264:289–297, 1999.

[165] Ashok Chauhan, Joseph D. Taylor, and Alain Nogaret. Dual mechanism for the emergence of synchronization in inhibitory neural networks. *Scientific Reports*, 8:11431, 2018.

[166] John J. Hopfield. Neural networks and physical systems with emergent collective computational abilities. *Proceedings of the National Academy of Sciences of the United States of America*, 79:2554–2558, 1982.

[167] Raúl Rojas. Neural networks: A systematic introduction. *Springer-Verlag, Berlin, New-York*, 1996.

[168] Johannes Friedrich, Pengcheng Zhou, and Liam Paninski. Fast online deconvolution of calcium imaging data. *PLOS Computational Biology*, 13:e1005423, 2017.

[169] Joshua T. Vogelstein, Adam M. Packer, Timothy A. Machado, Tanya Sippy, Baktash Babadi, Rafael Yuste, and Liam Paninski. Fast non negative deconvolution for spike train inference from population calcium imaging. *Journal of Neurophysiology*, 104:3691–3704, 2009.

[170] Thomas Deneux, Attila Kaszás, Gergely Szalay, Gergely Katona, Tamás Lakner, Amiram Grinvald, Balázs Rózsa, and Ivo Vanzetta. Accurate spike estimation from noisy calcium signals for ultrafast three-dimensional imaging of large neuronal populations *in vivo*. *Nature Communications*, 7:12190, 2016.

[171] Artur Speiser, Jinyao Yan, Evan W. Archer, Lars Buesing, Srinivas C. Turaga, and Jakob H. Macke. Fast amortized inference of neural activity from calcium imaging data with variational autoencoders. *Advances in Neural Information Processing Systems*, 30, 2017.

[172] I. Tasaki, A Watanabe, R. Sandlin, and L. Carnay. Changes in fluorescence, turbidity, and birefringence associated with nerve excitation. *Proceedings of the National Academy of Sciences of the United States of America*, 61:883–888, 1968.

[173] Lawrence B. Cohen, Brian M. Salzberg, H. V. Davila, William N. Ross, David Landowne, A. S. Waggoner, and C. H. Wang. Changes in axon fluorescence during activity: Molecular probes of membrane potential. *The Journal of Membrane Biology*, 19:1–36, 1974.

[174] Irene Mollinedo-Gajate, Chenchen Song, and Thomas Knöpfel. Genetically encoded voltage indicators. *Advances in experimental medicine and biology*, 1293:209–224, 2021.